University of Crete

Department of Materials Science & Technology

Foundation for Research and Technology – Hellas

Institute of Electronic Structure & Laser

PhD Thesis

By Evangelos Skoulas

Surface structuring of bulk and thin film materials with polarized ultrashort laser pulses

<u>Supervisors</u>

Dr. Emmanuel Stratakis

Prof. Dimitris Papazoglou   Heraklion, Crete 2020

Thesis Summary

Utilizing laser light for materials processing came along with the first laser invention and revolutionized a plethora of technological applications and scientific fields. It did not take long for lasers to be applied on a vast range of diverse fields such as manufacturing, imaging, chemical analysis-synthesis, medicine and biology. However, the fundamentals of lasing and coherent light manipulation, along with the scientific understanding of the physics involved are under continuous investigation given that any advance in laser science and instrumentation follows significant breakthroughs in most research fields. In particular, since the development of laser sources with ultrashort wave-packets so rapid that can yield timescales of a few femtoseconds (10^{-15} sec), the field of laser ablation and micro-structuring was revolutionized as today there are many ways to induced surface morphological changes with the use of laser light exclusively.

Among the various and fascinating phenomena that can take place during the interaction of intense ultrashort laser pulses with solid matter such as ablation, welding, sintering and thermal annealing, it is found that in some conditions, tiny self-arranged and reproducible surface patterns can occur. These surface structures beat the typical laser beam diffraction limit and since their first observation they paved the way for a new laser processing field during the past decades due to their implementation in numerous technological and industrial applications.

This thesis explores the formation of a particular type of self-assembled structures, the laser induced periodic surface structures (LIPSS), their morphological features, and possible ways to control them by introducing vectorial polarization states as a new parameter among the various laser parameters such as the laser wavelength, energy, etc. of the laser pulses is investigated. Moreover, this work explores the effect of complex polarization states on the LIPSS formation mechanism, along with the reversibility of the observed surface morphologies utilizing ideal material case, which can permit under specific irradiation conditions the formation and deletion of high ordered LIPSS. Finally, the yet unexplored utilization of these type of structures on sub-micrometer sized metal films is investigated. A few examples of the use of laser-based patterned surfaces with femtosecond (fs) pulses are discussed as they can be further utilized in applications such as laser marking, the direct realization of planar meta-optics and polarizers and potentially in fs-data storage.

The first Chapter is focused on a review of LIPSS and their classification based on the distinct features of the induced structures. A review of the most prominent physical mechanisms that lead to the formation of LIPSS is presented along with the most important applications that have risen from this field.

In Chapter 2, the experimental protocols and procedures are presented. The intensity distribution of the laser beam is described along with the polarization conversion process. A brief overview of the fundamentals of Gaussian and Cylindrical vector beams, their use for dynamic surface processing as well as the development of the experimental set up are presented. Moreover, the details of all material targets and the characterization methods (along with digital image analysis) that are involved in this thesis are listed.

In chapter 3 the experimental and theoretical results on irradiations of metals well known for their use in industry such as Nickel (Ni) and steel surfaces are presented and discussed. A systematic study was conducted with LIPSS formation with linear, radial and azimuthally polarized laser pulses. The dependence of such exotic polarization states in the formation mechanism is explored along with the experimental conditions that lead to complex structures of multiple orientations exhibiting omnidirectional angle independent diffractive properties.

For chapter 4, the use of controlled irradiation conditions leads to high-regularity, erasable and re-writable periodic surface patterns on silver metaphosphate glass ($AgPO_3$) by means of ultrashort pulsed laser processing. The so-formed periodic patterns can be readily erased upon further exposure to femtosecond laser irradiation under irradiating conditions that can selectively permit or deny the physical process that leads to LIPSS formation. This all-laser inscription and deletion protocol allows the reversible patterning of the phosphate glass surface by employing a single laser beam and could potentially be utilized for data storage.

Finally, in the last chapter, we explore the direct realization of LIPSS, on sub-micrometer thin Ni films which are deposited on a dielectric substrate. The experimental investigation showed that it is possible, under specific conditions to realize high regular LIPSS on the thin film while the substrate remains unaffected. The fabricated surfaces were optically and morphologically characterized and exhibit significant response on the Infrared (IR) and The Mid-IR electromagnetic spectrum exactly as a wire grid polarizer. The effective spectrum of the polarizer can be controlled with the thin film ripple period which can be controlled precisely with the laser wavelength. Furthermore, due to the simplicity of this technique and the versatility, it can be potentially applied in almost all thin metal surfaces

regardless of the substrate characteristics. Whereas, this approach can be with further development revolutionize the current way we produce wire grid polarizing plates with no need for chemicals and time-consuming multi-step processes.

Table of Contents

1 Ultrafast laser induced surface processing – Literature overview

Abstract – The birth of the original idea for the realization of surface structures by means of ultrashort laser pulses is briefly reviewed. The LIPSS formation, is characterized as a universal phenomenon that occurs on almost all classes of solid surfaces upon irradiation with intense polarized pulsed laser beams. Their classification and the proposed fundamental formation mechanisms are discussed. Modern methods for their morphology control and some examples of their technological applications are given as well.

1.1 Introduction

The ability to structure solid surfaces exclusively with laser light has gained significant attention due to the relative simplicity of the process itself and the remarkable functionalities that a material can attain by this drastic change in the surface morphological features. There are currently two major approaches to provoke laser surface modification. The direct laser inscription and the laser induced self-assembly.

In the early sixties, Birnbaum was the first to observe periodically arranged structures, following the irradiation of Germanium surfaces, using one of the first pulsed ruby lasers [1]. These structures are commonly called ''laser induced periodic surface structures''. Since then, an extensive research has been conducted, with the aim to reproduce and to explore the formation mechanism of these structures but also to exploit the exotic properties that LIPSS can induce to a solid surface [2].

This chapter will provide an overview of the LIPSS formation as a universal phenomenon that can be observed in almost every class of materials upon irradiation with short laser pulses. The proposed and most widely accepted theoretical models that can describe LIPSS formation are also discussed, accounting for many issues related to the mechanisms for the generation and evolution of these structures that have been addressed, while still, the complete understanding of this extraordinary phenomenon is missing. The various types of LIPSS and the dominant physical processes that account for their formation are

presented, along with the most important applications that LIPSS have been implemented.

1.2 Classification of LIPSS

Surface structuring with laser pulses can be classified in two major approaches, one which is based on self-organized laser-irradiated structures and another with direct laser-inscribed structures (see Figure 1.1) [3]. The direct laser inscription is the most common approach as it exploits the laser beam as a tool to modify the surface most of the times with ablative conditions. The direct laser inscription, also called micromachining is the most common approach for surface modification with laser pulses, however, there is a limitation on the spatial features of the inscribed structures as the spatial resolution is always limited by the laser beam diffraction limit. On the other hand, self-organized surface irradiation results in features characteristic (quasi-)periodic surface morphologies of a particular orientation which take place within the laser beam spatial limits. The self-organized surface structures may consist of microstructures, nanostructures, or hybrid variants. The emphasis of this thesis will be centered on the formation of periodic nanostructures (Figure. 1.1)
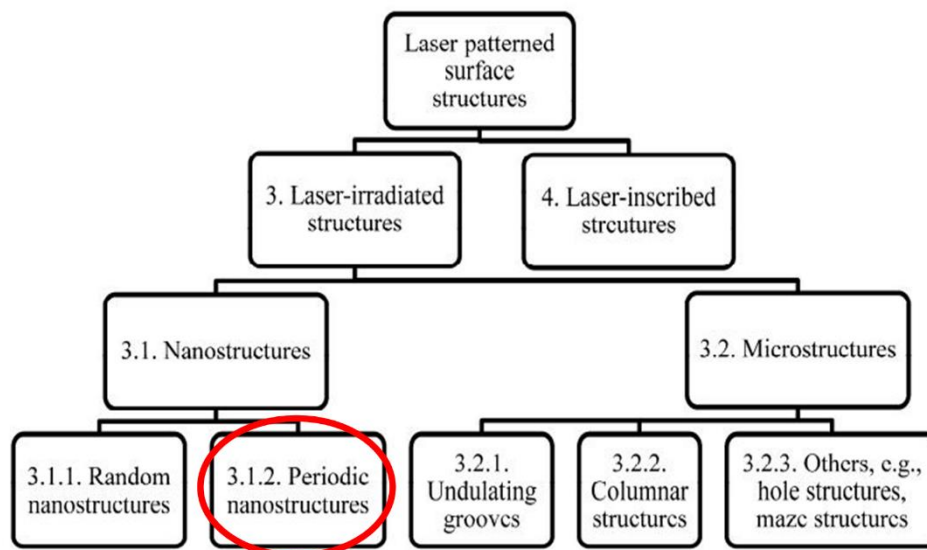

Fig. 1.1: Classification of laser-patterned surface structures. Image reproduced from Ref. [3].

1. Ultrafast laser induced surface processing – Literature overview

The periodic self-organized surface structures are usually classified as nanometric laser-induced periodic surface structures LIPSS, (also termed as 'ripples'). Ripples are observed as high spatial frequency LIPSS (HSFL), Figure 1.2(a) featuring periods significantly smaller than the irradiation wavelength ($\Lambda < \lambda/2$) or as low spatial frequency LIPSS (LSFL), Figure 1.2(b) with periodicity of the order of the laser wavelength [2,4,5]. LSFL and HSFL, both exhibit a well-defined orientation with respect to a linear polarization state of the incident laser light and recently it has been also observed that they follow the electric fields orientation for other more complex polarization states [6–8].
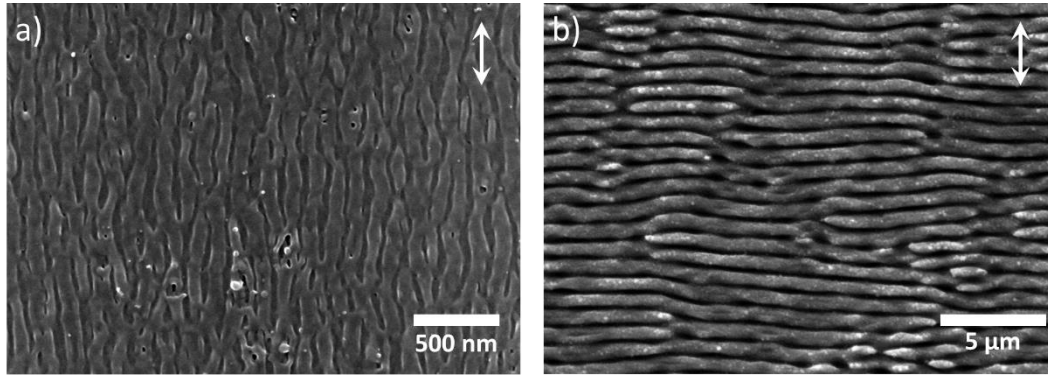
Fig. 1.2: *Top-view scanning electron microscopy images of two characteristic surface morphologies observed upon femtosecond laser scan processing of a Titanium surface (1026 nm, 170 fs, 1 kHz). (a) High spatial frequency LIPSS (HSFL), (b) Low spatial frequency LIPSS (LSFL). The double ended white arrow indicate the polarization state of the exciting laser source.*

The characteristics such as the periodicity and the orientation of ripples strongly depend on the irradiated material [2,9]. For strongly absorbing materials (metals or semiconductors), near-wavelength sized LSFL are usually generated with an orientation perpendicular to the laser beam polarization. The periods are close to the laser wavelength and their specific value has been found to depend on the optical properties of the material [9–12], the pulse number[13], and the surface roughness [11,14–16]. These structures are observed in the ablative regime for fluences up to several times the ablation threshold. For fluences very close to the ablation threshold, HSFL can be formed [2]. Note that semiconductors often behave like metals as they can be transiently made metallic upon high-intensity ultrashort laser pulse irradiation[10,17]. Semiconductors in addition may show the peculiarity of enabling the formation of amorphous-crystalline LSFL in a narrow fluence interval below the ablation threshold [18,19].

For weakly absorbing materials (dielectrics), sub-wavelength-sized LSFL are found mostly with an orientation parallel to the laser polarization. The periods are close to λ/n, with n being the refractive index of the material[20,21]. The corresponding HSFL on dielectrics normally are oriented perpendicular to the polarization[22,23] of the laser beam

but sometimes also parallel [24]. In this thesis we will focus more on LSFL structures and less on HSFL, since those are the structures we experimentally achieved and used for surface functionalization.

1.3 Physical mechanisms – Proposed theoretical models

To provide a detailed description of the physical origin of LIPSS formation as well as the quantitative features of the induced self-assembled structures on the surface of the irradiated material upon excitation with ultrashort pulsed lasers, a thorough investigation of the underlying multiscale phenomena that take place is required. Following Birnbaum's first time observation that the surface morphology can be controlled through formation of LIPSS[1] he tried to explain their formation due to diffraction effects. Emmony et al. in 1973 proposed an interface mechanism in which the irradiated laser light, is scattered on the surface from an existing roughness[25]. They also observed that the periodic structures size is comparable with the laser wavelength and expressed their formation with a general surface scattering model describing the interference of the incident with the surface scattered waves excited due to surface roughness. Based on this model, the ripples period Λ is equal to:

$$\Lambda = \frac{\lambda}{1 \pm sin\theta}$$

Eq. 1

where λ the laser wavelength and θ is the angle of the incidence laser beam. For normal incidence, the equation 1 gives $\Lambda \sim \lambda$ and therefore the term LSFL.

Later on, Sipe et al. reported an until today well-established formation mechanism of surface structures[26,27]. They claimed that the energy deposition on a rough surface (depending on the wavelength) in not homogeneous and introduced an "efficacy factor", η [26]. Moreover, that strong peak of electromagnetic field inducing the periodic surface patterns with specific orientation depends not only on the angle of incidence but also on the polarization of the laser beam. They proposed a new model in which the interference of incident beam with the surface-scattered wave originates the LIPSS formation. It didn't take long for the surface-scattered wave scenario to be replaced with the proposition that the incident laser beam interfere with surface electron density waves commonly called as

surface plasmon polariton waves (SPPs). Since the SPPs are the most prominent LIPSS formation mechanism it will be discussed more extensively on the following paragraph.

In addition, numerous other studies have been reported regarding the formation mechanisms of LIPSS [28,29]. Some authors considered non-resonant models like capillary wave excitation [30] and solid surface defects. In a totally different approach, in 2002, Reif et al.[31] proposed that ripples take place at the bottom of the laser ablated crater due to a self-organized structure formation during the surface relaxation. Instead, the other proposals suggest to involve electromagnetic waves and light localization in order to explain the properties of LIPSSs[32]. Another important contribution was from Huang et. al who reported a multiple pulse feedback mechanism in which they considered that the ripples result from the initial direct SPPs-laser interference and the subsequent grating-assisted SPP-laser coupling[33]. Here, Dufft et. al [34] and Bonse et. al [10] are worth mentioning as they suggested the carrier-dependent LIPSS formation by combining the classical theory of Sipe et al. [26] and the the Drude model (1900) and accounting for the optical and electrical properties of a laser excited material.

However, the origin of LIPSS is still debatable, since there is not yet reported a single theoretical model that can account and predict all classes of LIPSS. Undoubtably, one other process is also required in order to cause dramatic change in the surface morphological profile. Electromagnetic effects themselves are not sufficient to achieve that. Hence, other physical process like a transient phase transition, i.e., melting, that eventually leads to a surface modification [35] is required to change the relief. Other processes might involve ablation (i.e., mass removal)[36], spallation or even thermomechanical effects [37].

Finally, various theoretical approaches or experimental observations were performed in a variety of conditions to describe the evolution of the surface morphology and LIPSS formation. One other approach was based on self-organization processes [38], near field enhancement from random surface inhomogeneities[39]. However, the underlying theoretical approach was not sufficient to correlate the laser conditions with the most types of the laser induced surface morphological features but given that it is an interesting approach and the best theoretical approximation that can account for HSFL will with also provide a brief review in the following paragraphs.

1.3.1 Surface Plasmon Polariton Waves

Since both the LSFL and HSFL orientation always depend on the polarization direction it can be inferred that they originate from an electromagnetic mechanism leading to a spatially modulated deposition (absorption) of the laser pulse energy [2,9,23]. The absorption channels, however, can be different among the material classes. While for metals and semiconductors usually, the excitation and interference of Surface Plasmon Polaritons with the incident laser beam are involved and eventually lead in the formation of LSFL [9,10,17,40,41]. Recent approaches attribute the formation of HSFL to the interference between the incident beam and the radiation scattered at the rough surface while the proposed mechanism is associated to the coupling of the incident light with the far-field scattering of the rough dielectric surface [23]. In most models, excitation of modes and generation of conditions that lead to LIPSS formation is closely related to the carrier density levels upon irradiation with high intensity fields [10,22,23,32,40–44].

Although we can sufficiently explain the LSFL with the simple interference theory, it has been observed on a large number of experiments that ripple periodicity shows much smaller values than the initial laser wavelength ($\Lambda << \lambda$). Hence, their formation could not be explained by the mechanism related to Eq. 1. An improved and widely accepted mechanism that accounts for LSFL formation is further developed and depicted in Eq. 2. The proposed mechanism relates the ripples generation to surface plasmon waves, considering that all solid surfaces shows metallic behavior at high temperatures allowing excitation of surface plasmon waves. Such waves are electron density waves propagating at the interface between a metal and a dielectric and are often called surface plasmon polaritons (SPP)[45]. Figure 1.4 shows an electron density wave propagating across the metal-dielectric interface. SPP, can be defined as the coupling of the surface plasmon and the electric field of the laser beam; it can be generated during the material irradiation due to the accumulation of free carriers.
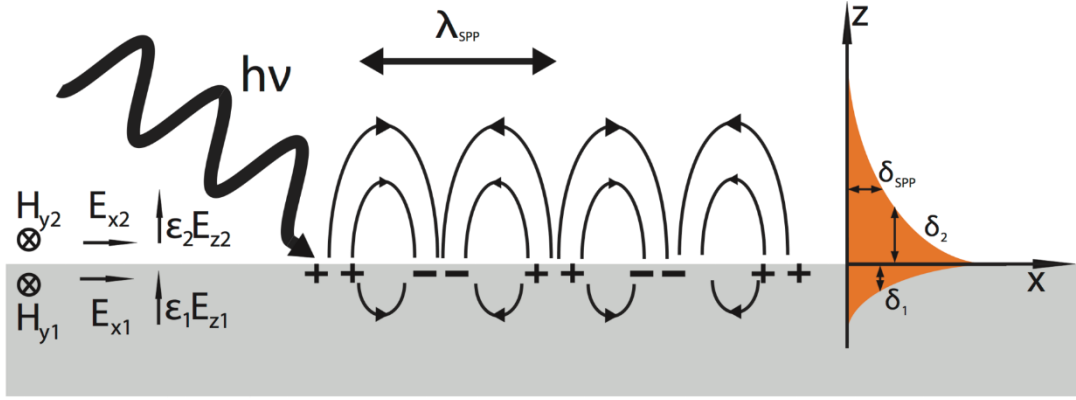
Fig. 1.3: Illustration of the field components of an SPP supported by a metal–dielectric interface. Exhibiting electric field components normal to the interface (z-axis) and along the propagation direction (x-axis). The mode profile (orange) shows the exponential dependence of the electromagnetic field intensity on the distance away from the interface is shown on the right. Reprinted from Wikimedia Commons.

The plasmon's wavelength, λ_{spp}, is related to the wavelength of a single laser pulse on a flat surface through the relations:

$$\Lambda = \frac{\lambda}{\dfrac{\lambda}{\lambda_{spp}} \pm sin\theta}$$

Eq. 2

λ_s can be obtained by the dispersion relation on metal/dielectric interface assuming $\varepsilon'' < |\varepsilon'|$ and a real ε_d,

$$\lambda_{spp} = \left(\frac{\varepsilon' + \varepsilon_d}{\varepsilon' \varepsilon_d}\right)^{1/2}$$

Eq. 3

$$\varepsilon' = Re\left(1 + (\varepsilon_g - 1)\left(1 - \frac{N}{n_0}\right) - \frac{N}{N_{cr}}\frac{1}{\left(1 + i\frac{1}{\omega\tau_e}\right)}\right)$$

Eq. 4

where λ is the laser wavelength, λ_s is the plasmon wavelength, ε' is the real part of ε of a laser-induced high excited surface are the real parts and ε_d is the dielectric constant of the dielectric material (for air, $\varepsilon_d = 1$), ε_g stands for the dielectric constant of the unexcited material, ω is the frequency of the incident beam, n_o is the valence band density.

The SPP propagation on metal or semi-conductive surfaces and all the above relations are pretty capable of predicting the LIPSS formation as well as their spatial characteristics

such as periodicity. Although as we mentioned before there are multiple and competitive physical processes that take place during and after ablation processes. In principle, all the previously mentioned laser beam parameters (wavelength, pulse duration, fluence, number of pulses, angle of incidence, and beam polarization state) determine the onset of the surface modification as energy absorption, electrodynamical effects and relaxation processes are critical to the material heating. Femtosecond laser interaction also involves several complex phenomena, including energy absorption, photo-ionization processes, electron excitation and electron-relaxation processes[46].

The multiscale processes are different with respect to the material nature and can define in some extent the final laser induced surface features. Therefore, besides the SPPs a two-temperature model, emerged from the Boltzmann's transport equation[47] will be described in some extend in the following paragraph which will provide useful information regarding the variations between the electron and lattice subsystems of the materials that sustain irradiation with ultrashort laser pulses. In the following paragraph an energy exchange model is presented capable of probing the electron or carrier energy/temperature in time and how it is delivered to the lattice of the material leading in thermalization.

1.3.2 Two temperature model

One of the most popular theoretical models to predict how heat flows from the exited electrons to the lattice, when it comes to ultrafast laser processing on a solid surface, is the two-temperature model (TTM). TTM has been widely used with a lot of variations depending on the materials and the irradiation conditions to calculate the temperature variations between the electron and lattice subsystems [48,49]. Due to the fact that the beam spot diameter typically varies from 10-100μm, much greater than the optical-electron penetration depth (tens of nanometers) the energy transport into a metal can be described by the following one-dimensional two temperature diffusion model. Hence assuming that the electron thermalization is very fast and that the electron-lattice temperatures can be described by T_e and T_l.

Evolution of electron temperature in time	$$C_e \frac{\partial T_e}{\partial t} = -\frac{\partial Q(z)}{\partial z} - \gamma(T_e - T_l) + S$$	*Eq. 5*

Evolution of lattice temperature in time	$$C_l \frac{\partial T_l}{\partial t} = \gamma(T_e - T_l)$$	*Eq. 6*
Heat flux	$$Q(z) = -k_e \frac{\partial T_e}{\partial z},$$	*Eq. 7*
Laser heating source	$$S = I(t)Aae^{-az}$$	*Eq. 8*

Where *z* axis is always perpendicular to the target surface, *Q(z)* the heat flux, *S* is the laser heating source. *I(t)* is the laser intensity, *A=1-R* and *R* the reflectivity, *a* are the surface transmissivity and the materials absorption coefficient. C_e, C_l are the heat capacities for the electron and lattice subsystems and γ is the electron phonon coupling parameter which can be expressed as $\gamma = C_e/\tau_e$, where τ_e stands for the electron, lattice characteristic heating phases, for every case.

1.3.2.1   TTM and femtosecond laser pulses

In this thesis we conduct all of our experiments with laser pulses of duration of some tens of femtoseconds. The use of laser pulses at the fs-regime is preferred in order to not only to provoke surface morphological changes but also to avoid as much as possible the pronounced thermalization that laser irradiation can cause to the surface[50]. Hence, the total energy deposition to the material surface is way finished before the exited electron system starts to return (relaxation) on ground state and eventually reach thermal equilibrium. Therefore, we have to consider that the pulse duration (τ_p) is less in time that the electron cooling time. Subsequently, following the equations 5-8 which have three characteristic timescales τ_e, τ_l and τ_p where $\tau_e = C_e/\gamma$ the electron cooling time, $\tau_l = C_l/\gamma$ and τ_p the laser pulse duration. In our case the pulse duration is shorter than the electron cooling time $\tau_p << \tau_e$ as we irradiate with ~170 fs pulse duration. So, this means that for $t << \tau_e$, the $C_e/T_e >> \gamma T_e$, the electron-lattice coupling can be neglected. Accordingly, the electron temperature can be calculated as following:

$$C_e' \frac{\partial T_e^2}{\partial t} = 2(1-R)I(t)ae^{-az} \qquad \qquad \textit{Eq. 9}$$

Assuming that the laser intensity *I* and the material reflectivity *R*, are constant in time

$$T_e(t) = \sqrt{\left(T_0{}^2 + \frac{2I_a a}{C_e{}'} t e^{-az}\right)} \qquad \qquad \textit{Eq. 10}$$

Were $I_a = I_o A$ with I_0 constant, and $T_0 = T_e(0)$ as the initial temperature. Finally, at the end of the laser pulse (as $T_0 \ll T_e$)

$$T_e(\tau_p) \cong \sqrt{\left(\frac{2I_a \tau_p a}{C_e{}'}\right)(e^{-az})} \qquad \qquad \textit{Eq. 11}$$

1.3.2.2   Combined TTM and Hydrodynamic effects

Given that the phase change of an irradiated surface in inevitable and that before resolidification the melted material volume dynamics has to be taken into account for the formation of LIPSS, in 2012 Tsibidis and colleagues has introduced a unifying theoretical framework by considering that hydrodynamic, and not mass removal, effects constitute the main agent that govern the initial morphological changes[49].

The combined theory can provide an extension based on the spatial dependence of the laser intensity distribution that induces bending of the isothermal lines. The proposed model comprises, a heat transfer component that accounts for the particle dynamics and heat conduction phenomena and a hydrodynamics component, which describes the molten material dynamics and the resolidification process.

In this context considering a Newtonian incompressive fluid for the mass conservation $\vec{\nabla} \cdot \vec{u} = 0$, where $\vec{u}$ is the velocity of the fluid while for the energy conservation:

$$C_l\left(\frac{\partial T_l}{\partial t} + \vec{\nabla} \cdot (\vec{u} T_l)\right) = \vec{\nabla}\left(K_l \vec{\nabla} T_l\right) \qquad \qquad \textit{Eq. 12}$$

And for the momentum conservation:

$$p_l\left(\frac{\partial \vec{u}}{\partial t} + \vec{\nabla}\vec{u} \cdot \vec{u}\right) = \vec{\nabla} \cdot \left(-P + \mu(\vec{\nabla}\vec{u}) + \mu(\vec{\nabla}\vec{u})^T\right) \qquad \qquad \textit{Eq. 13}$$

Where K_L is the thermal conductivity of the lattice, μ is the liquid viscosity, P pressure. and K_L stand for the thermal conductivity of the liquid phase, respectively. It is evident that

the transition between a purely solid to a completely liquid phase requires the presence of an intermediate zone that contains material in both phases.

1.3.3 Near-field enhancement from random inhomogeneities

Another proposed mechanism that aims to describe self-assembly is based on the electromagnetic effects originating by irradiating materials in the presence of initial inhomogeneities, scattering centers or defects. In order to account for the periodic self-organization of matter beyond the diffraction limit, compares the mechanisms of periodic nanostructure formation on the surface and in the bulk of fused silica. Rudenko and colleagues show that volume nanogratings and surface nanoripples having subwavelength periodicity and oriented perpendicular to the laser polarization share the same electromagnetic origin[39,51]. They claim that the nanostructure orientation is defined by the near-field local enhancement in the vicinity of the inhomogeneous scattering centers while the periodicity of the nanostructures is attributed to the coherent superposition of the waves scattered at inhomogeneities. Consequently, the latter structures also share the electromagnetic origin, but are related to the incident field interference with the scattered far-field of rough non-metallic or transiently metallic surfaces. Given that in this thesis we did not performed any experiment in the bulk of any material it is more important to discuss the proposed effect of the near-field local enhancement in the vicinity of the inhomogeneous scattering centers on the surface.

So, an example of surface nanostructuring, for a rough surface between air (= 1) and a dielectric surface with half-sphere inhomogeneities of radius r = 10 nm is considered in Figure 1.4(a). Below the surface, random perpendicular oriented patterns are generated by the interference of the incident field with near-field scattered waves by single inhomogeneities, so-called roughness-dependent radiation remnants also referred previously at paragraph 1.3. These patterns are considered as the seeds for the periodic HSFL formation which eventually leads to LSFL. Whereas, for a low number of applied pulses, subwavelength HSFL oriented perpendicular to the laser polarization are almost randomly-distributed as reported in the experimental literature [40,52,53].

Furthermore, the presence of the interface air-fused silica is not necessary for the HSFL structures or volume nanograting formation. However, the growth of the nanoplasmas can be significantly accelerated by the ionization processes in dielectrics if the predistributed inhomogeneous seeds for the nanostructure formation acquire the

metallic properties[54]. Apart from the enhanced near-field interaction with the incident light, the rough surface is at the origin of the far-field periodic modulation, enhanced in parallel direction to the laser polarization for non-metallic surface $Re(\varepsilon) > 0$ and in perpendicular direction for metallic surface $Re(\varepsilon) < 0$. The typical intensity distributions from one single dielectric hemisphere on the non-excited and the metallic fused silica surfaces are shown in Figure 1.4(b,c). The intensity patterns dominant enhancement in the directions perpendicular (Figure 1.4(b)) and parallel (Figure 1.4(c)) to the laser polarization as we it was previously predicted by Sipe theory [26] and used afterword to explain the orientation and the laser wavelength in media periodicity of the classical laser-induced ripples[32]. In this case the presence of the interface (surface) is essential for generation of the far-field periodic intensity patterns and the condition $Re(\varepsilon) < 0$ is sufficient to generate the perpendicular oriented patterns, even if the condition for the surface plasmon wave excitation $Re(\varepsilon) < -1$ is not satisfied.
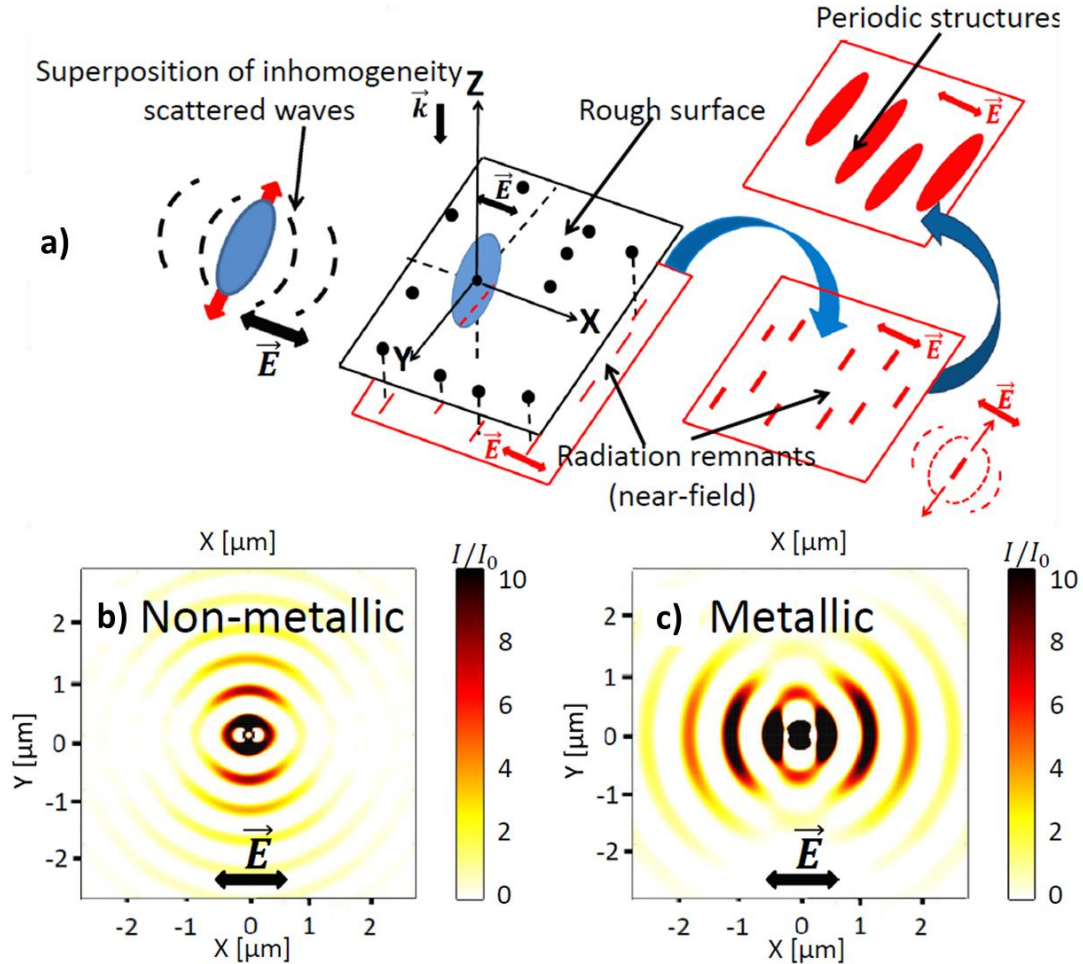

Fig. 1.4: (a) Schematic representation of the electromagnetic formation mechanisms of periodic nanostructures in surface ultrashort laser pulses. Intensity pattern from a single inhomogeneity (hemisphere with R = 50 nm) (b) on the non-excited fused silica surface ($n^2 = 2.105$), (c) on the excited metallic fused silica surface ($\varepsilon = -1 + i0.5$) image reproduced from ref [51].

Therefore, the electromagnetic origin of LIPSS with periodicities between $\lambda/2–\lambda$ is a process of multipulse selection of hybrid standing waves produced by the interference of the incident light with surface wave scattered by nanoholes with comparable contributions of SPP and continues wave (CW). An important conclusion is that there are two main factors that can lead to periodicity reduction. The enhanced dipole–dipole coupling between nanoholes, and the surface curvature at the edges of the ablation crater, dictating the saturation value of well-organized LIPSS. This claim was supported with multipulse numerical simulations based on Maxwell equations, coupled with the TTM and ablation removal criterion, to reveal the transition from a rough surface to a pronounced sinusoidal periodic grating.

Conclusively the local field enhancement contributes to their growth into nanoplanes in the direction perpendicular to the laser polarization on a shot-to-shot basis, were in addition to the near-field enhancement, each nanoplasma or inhomogeneity center scatters spherical waves into the far-field, which are enhanced parallel to the nanoplane.

1.4 LIPSS applications and functionalities

Since the LIPSS typical period of the structures matches the wavelength range of visible/near-infrared light, pronounced changes appear in the reflection or transmission spectra of a material, and in some cases diffraction of white light occurs into its different spectral components. In this context, the work of Vorobyev and Guo [55] demonstrated for several metals a considerable control over the color appearance through generation of self-organized surface structures with femtosecond laser pulses. Furthermore, extremely broad Hue color range of angle-insensitive colors on silver, gold, copper and aluminum surfaces [56]. Inspired by the glass-wing butterfly *Greta oto* [57] and the *Cicada Cretensis* [58] species, laser structuring has been employed to generate structural anti-reflective properties in glasses [59]. Moreover, it has also been demonstrated that fs laser nanostructuring of a SiC surface leads to an increase in visible light transmission by a factor of more than 60 [60]. The LIPSS are also used for luminescence enhancement in light-emitting diode (LED) [61,62] and ZnO nanowires [63].

LIPSS formation is not limited to the surface of a material but can also be formed underneath its surface. One example are sub-wavelength periodic gratings inside transparent materials that share their electromagnetic formation mechanism with HSFL found at surfaces as described above [23]. Such sub-surface self-organized gratings in form

of voxels can be produced by focusing fs laser pulses inside fused silica glass [64], paving the way for high-density 5D data storage. The information encoded in an individual voxel is not limited to binary information but can be multiplexed via the rotation of the nanograting, giving rise to optical anisotropy (form birefringence) and effectively adding a fourth dimension [65]. A fifth dimension can be added in form of the strength of the retardance, further increasing storage density [65]. The same self-organized grating structure in fused silica has also found applications in generating laser beams with exotic properties [66] and one of these element was used in this thesis as a polarization converter in Chapter 3.

Another self-organization process that can be triggered inside glasses is the self-organized re-distribution of different elements of the glass composition [67,68]. This laser processing strategy has been further developed in order to fabricate optical waveguides by writing tracks inside a glass, whose self-organized cross sections feature a region enriched by heavy elements, locally increasing the refractive index and thus strongly confining light [68,69]. Using this technique, efficient optical waveguides, as well as optical amplifiers and integrated lasers with high net gain have been fabricated [70,71]. The pronounced hierarchy of many types of LIPSS in metals leads to strong electromagnetic field enhancement. Microfluidic surface enhanced Raman scattering (SERS) chips have already been fabricated by all-femtosecond-laser processing [72]. Some important examples of LIPSS applications are depicted in Figure 1.4 where images with outstanding examples are illustrated for surface functionalization in Figure 1.4(a) photonics, biologically active surfaces (Figure 1.4(b)), remarkable wetting properties (Figure 1.4(c)), effects in tribology (Figure 1.4(d)), structural coloration (Figure 1.4(e)) and data storage (Figure 1.4(f)).
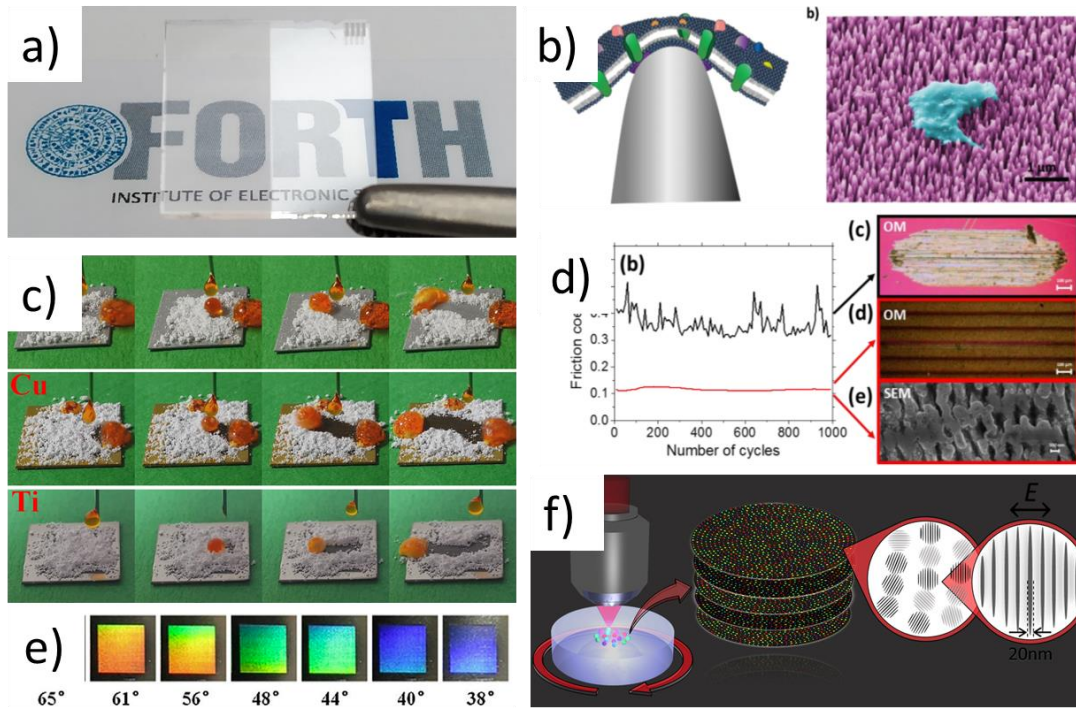
Fig. 1.5: Summarized the most important LIPSS applications categories up to date with an example for each one for (a)anti-reflection, (b) bactericidal activity, (c) wettability, (d) friction reduction, (e)iridescence and (f) data storage. The image (a) was reproduced from ref [73], (b) from ref [74], (c) from ref[75], image(d) from ref[2], (e) from ref[76] and (f) from ref[77].

In other properties LIPSS are a popular as previously mentioned as a direct way to control the surface wetting properties for metal [55,78–84], semiconductors [85–87], dielectrics [88,89], even natural stone, such as marble [90]. Furthermore in metals, the very same self-organized structures that feature hydrophobic behavior present oleophilic properties [80,91,92] leading to friction control [93,94] and underwater superoleophobicity [85]. These remarkable wettability features are also exploited for fluidic transport [79,95–97], surfaces that can transport water with gradient surface tension. The self-organized laser structuring offers also great potential for enhancing and directing cell growth on suitably structured substrates [98–105], implantable vaccines [106]. Moreover, Laser micro- and nanostructuring provides a promising method to reduce the growth of biofilms by altering topographical and chemical surface properties [107–110].

2 Experimental methods

Abstract - This chapter discusses the procedures illustrating the experimental setups (i.e. laser source, optical components, target materials and instrumentation) used in the target irradiation experiments and the characterization techniques exploited for optical and chemical analysis as well as for the determination of the various spatial features of the laser induced periodic surface structures.

2.1 Introduction

The direct fabrication of LIPSS structures is based on laser matter interactions with specific parameters. The effects that lead to the desired laser structuring are performed under certain conditions of the laser beam parameters such as wavelength, pulse duration, pulse energy, beam size, polarization and repetition rate. These parameters can be optimized according to the substrate material and irradiation conditions [79,80]. The laser beam characteristics can significantly affect the formation and features of the surface structures. In our experiments we generally used fs laser beams with a Gaussian intensity spatial profile only with the exception of chapter 3. However, the interesting capabilities of fs surface treatment for realizing mask free surface and volume structuring are highlighted in the present work by means of experiments with cylindrically polarized laser beams[111].

In this chapter, the experimental methods including the definition of the laser beam parameters, instrumentation such as laser type, optics, material targets, electronics and mechanical devices are presented, along with the illustration of the experimental techniques for the surface morphological and chemical and optical characterizations, which are discussed in detail.

2.2 Laser beam spatial profile

2.2.1   Gaussian beams

The Gaussian intensity profile is the most common laser beam mode and it can be described as a fundamental transverse electromagnetic mode (TEM$_{00}$). This Gaussian mode describes the intended output of most commercial lasers, given that such a beam can be focused into the most concentrated spot. For a Gaussian beam, the spatial profile of the normalized pulse fluence $\varphi(r)$ along the diameter of the beam, r, is given by:

$$\varphi(r) \; = \; \frac{2E_p}{\pi w_0^2} e^{\left(\frac{-2r^2}{w_0^2}\right)} \qquad\qquad Eq.\ 14$$

where E_p is the pulse energy and w_0 the waist of the fundamental Gaussian beam [111]. The maximum fluence value occurring within the Gaussian profile when the radius $r = 0$, is commonly named as peak fluence φ_p

$$\varphi(p) \; = \; \frac{2E_p}{\pi w_0^2} \qquad\qquad Eq.\ 15$$

The spot size or beam waist of a Gaussian beam is the location along the beam axis where the intensity is $1/e^2$ its own maximum value. A simple method to measure the spot size of the Gaussian beam is to use the fabricated circular craters produced by amorphization or ablation was provided at 1982 by Liu [112]. Considering the actual laser damaged craters radius profiles r_a (vertical radius) and r_b,(horizontal radius) and plotting out the following relations:

$$E_a = E_p \, e^{\left(\frac{-2r_a^2}{w_0^2}\right)} \qquad\qquad Eq.\ 16$$

$$E_b = E_p \, e^{\left(\frac{-2r_b^2}{w_0^2}\right)} \qquad\qquad Eq.\ 17$$

We end up with the extracted dependence of r_a and r_b as:

$$r_a^2 = \frac{w_0^2}{2} \ln\frac{E_p}{E_a} \qquad\qquad Eq.\ 18$$

2. Experimental methods

$$r_b^2 = \frac{w_0^2}{2} \ln \frac{E_p}{E_b}$$

From Equations (18-19), the beam spot size can be derived by plotting average r^2 versus energy E_p and estimating the slope of the plot, which is equal to $w_0^2/2$, through a fitting procedure. The parameters, E_a and E_b can be considered as the minimum pulse energies required for observing surface modification or ablation (threshold energies), which correspond to the above beam energies of Eq. (16-17) when r(a,b) is firstly observed on the material surface, introducing the threshold fluence value of φ_{th} which is expressed as:

$$\varphi(th) = \frac{2E_{a,b}}{\pi w_0^2}$$

Additionally, the beam w_0 can be calculated theoretically. The theoretical beam radius of a collimated laser beam after passing through the focusing (converging) lens is calculated by the following equation [113,114]:

$$w_o = \frac{2f\lambda M^2}{\pi D}$$

where f is the focal length of the focusing lens, λ is the wavelength of the laser, D is the input/collimated laser beam diameter onto the focusing lens, and M^2 is the beam propagation factor, which describes the difference between a real laser beam and an ideal diffraction-limited Gaussian beam.

The laser fluence see (equation 20) can be also altered not only by varying the laser pulse energy but it can be change by shifting the distance (z) between the sample and the lens, which alters the beam diameter. The beam radius (w_z) at any z position from the focus is given by[115]:

$$w_z = w_0 \sqrt{1 + (\frac{z}{z_R})^2}$$

where z_R is the Rayleigh length and for a beam propagation in air is given by:

$$z_R \;=\; \frac{\pi w_0^2}{\lambda}$$

Eq. 23

2.2.2 Cylindrical vector beams

Laser beams with cylindrical symmetry in polarization, the so-called cylindrical vector (CV) beams, have attracted significant recent attention, largely due to their unique properties [111,116,117]. Radial and azimuthal polarization also can be used as an ideal source for surface plasmon excitation with axially symmetric metal/dielectric structures, because plasmon excitation has a strong dependence on excitation polarization [8,118–120].
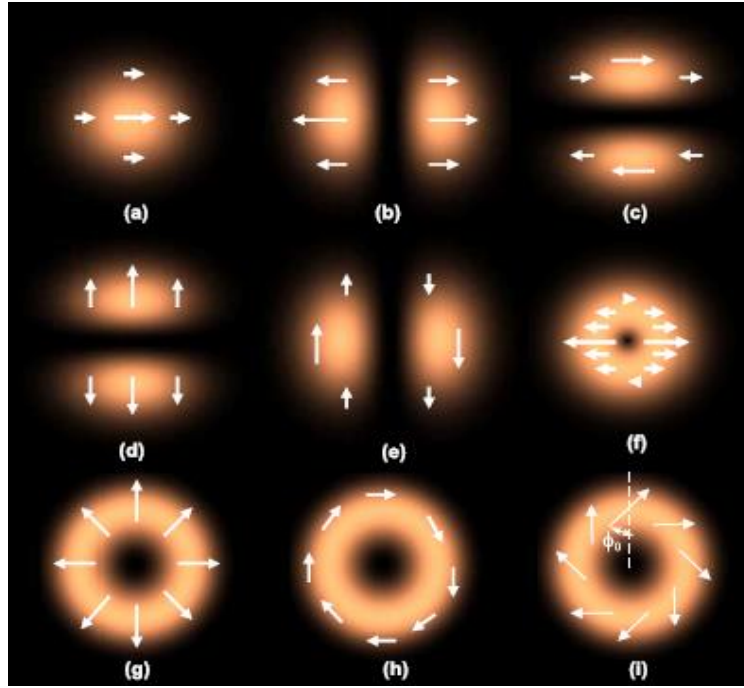

Fig. 2.1: Spatial distribution of instantaneous electric vector field for several conventional modes and CV modes: (a) x-polarized fundamental Gaussian mode, (b) x-polarized HG10 mode, (c) x-polarized HG01 mode, (d) y-polarized HG01 mode, (e) y-polarized HG01 mode, (f) x-polarized LG01 mode; (g) radially polarized mode, (h) azimuthally polarized mode, (i) generalized CV beams as a linear superposition of (g) and (h). Image reprinted from ref [111].

CV beams also can be used for three-dimensional focus engineering[121]. By controlling polarization azimuthal angle φ_0 from the radial direction (Fig. 2.1), it is possible to create focal field with a transverse flat-top profile. Introducing pupil plane phase or amplitude mask provides additional degrees of freedom and enables extra focal field profile control and highly homogeneous field distribution in three dimensions can be generated. Even

more exotic focal field distributions, such as an optical "bubble" or optical "needle" can be generated[122].

The cylindrical vector (CV) beams are vector-beam solutions of Maxwell's equations that obey axial symmetry in both amplitude and phase. Comparison of spatially homogenous state of polarization beams (SOP) beams and CV beams are illustrated in Figure 2.1. Spatially homogenous SOPs modes have instantaneous electric field, which may have an opposite direction due to inhomogeneous phase distribution across the beam. Typical CV beams cases are shown in Figure 2.1(g)-(i). When polarization of a beam is aligned in radially direction, it is called radial polarization. Similarly, azimuthal polarization is shown in Figure 2.1(h). A linear superposition of these two modes can produce beam with even more complex polarization distribution as shown in Figure 2.1.

The solutions for the spatially homogeneous SOP beams are obtained by solving the scalar Helmholtz equation:

$$(\nabla^2 + k^2)E = 0$$

where $k=2\pi/\lambda$ is the wave number. In Cartesian coordinates, the general solution for the electric field has a form

$$E(x,y,z,t) = u(x,y,z)e^{i(kz-\omega t)}$$

For slowly varying envelope approximation, the Hermite-Gauss modes (HG) solution can be obtained:

$$u(x,y,z) = E_0 H_m\sqrt{2}\frac{x}{w(z)}H_n\sqrt{2}\frac{x}{w(z)}\frac{w_0}{w(z)}e^{-i\varphi_{n,m}(z)}e^{i\frac{k}{2q(z)}r^2}$$

where $H_m(x)$ denotes Hermite polynomials, E_0 is a constant electric field amplitude, $w(z)$ is the beam size, w_0 is the beam size at the beam waist, z_0 is the Rayleigh range, $q(z)$ is complex beam parameter and $\varphi_{m,n}(z)$ is the Gouy phase shift[123].

The general solution in cylindrical coordinates, paraxial is:

$$E(r,\varphi,z,t) = u(r,\varphi,z)\,e^{i(kz-\omega t)}$$

2. Experimental methods

Substituting Equation (27) to (24) and applying the slowly varying envelope approximation we get differential equation:

$$\frac{1}{r}\frac{\partial}{\partial r}\left(r\frac{\partial}{\partial r}\right) + \frac{1}{r^2}\frac{\partial^2}{\partial\varphi^2} + 2ik\frac{\partial u}{\partial z} = 0$$

Eq. 28

From this equation two solutions can be found. The first solution describes Laguerre-Gauss modes (LG$_{pl}$)[124].

$$u(r,\varphi,z) = E_0\left(\sqrt{2}\frac{r}{w(z)}\right)^l L_p^l\left(\sqrt{2}\frac{r^2}{w(z)^2}\right)e^{-i\varphi_{pl}(z)}e^{i\frac{k}{2q(z)}r^2}e^{il\varphi}$$

Eq. 29

where L_L^l is the Laguerre polynomials (l – azimuthal index, p – radial index) and $\varphi_{pl}(z)$ is the Gouy phase shift. The second solution is independent of the azimuthal angle ϕ and describes Bessel-Gauss beams:

$$u(r,z) = E_0\frac{w_0}{w(z)}e^{-i\varphi(z)}e^{i\,k/(2q(z))\,r^2}J_0\left(\frac{\beta r}{1+iz/z_0}\right)e^{-\frac{\beta^2 z}{2k(1+\frac{iz}{z_0})}}$$

Eq. 30

Those three solutions (Hermite-Gauss, Laguerre-Gauss and Bessel-Gauss) correspond to beams with spatially homogeneous polarization.

In many practical applications, instead of the vector Bessel-Gauss solutions, the following simplified distribution can be used:

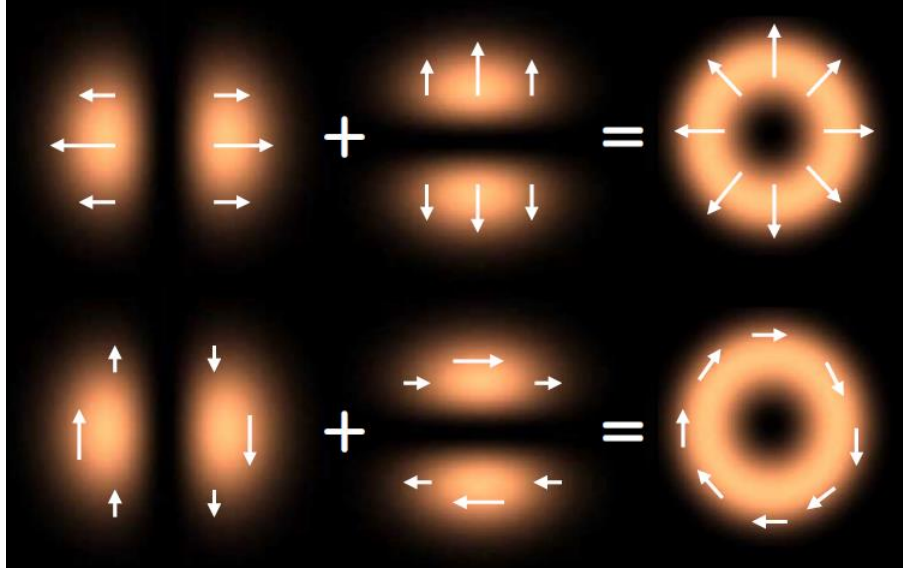$$\vec{E}(r,z) = Are^{\left(-\frac{r^2}{w^2}\right)}\vec{e}(r,\varphi)$$

Eq. 31

Fig. 2.2: Formation of radial and azimuthal polarizations using linear superposition of orthogonally polarized HG modes. Image reprinted from ref [111].

The profile of amplitude is the same like in LG$_{01}$ mode and without the vortex phase term $e^{(i\phi)}$. Alternatively, CV beams can be described as a superposition of orthogonally polarized Hermite-Gauss *HG$_{01}$* and *HG$_{10}$* modes as shown in Figure 2.2. For instance, radially and azimuthally polarized beams in such a way can be expressed as:

$$\vec{E}(Radial) = HG_{10}\vec{e}(x) + HG_{01}\vec{e}(y)$$

$$\vec{E}(Azimuthal) = HG_{01}\vec{e}(x) + HG_{10}\vec{e}(y)$$

2.3 S-Waveplate polarization converter

A converter from linear to more complex polarization states can be made by gluing several segments of λ/2 phase wave-plates with different discrete crystal layers. Such a converter was utilized to convert our laser typical Gaussian and linearly polarizer beam to a doughnut shaped cylindrically polarizer beam[125]. This polarization converter is an s-waveplate and the most fascinating aspect of it is that is works using nanograting HSFL structures which were formed in the volume of fused silica glass with fs laser pulses as previously mentioned on Chapter 1.4. Continuous phase profiles of nearly any optical

component can be fabricated in silica, which allows unparalleled control over the local phase of a laser beam that is transmitted by the element.

For the incident circular-polarized beam, the radial or azimuthal polarization can be formed with a space variant quarter-wave plate possessing a radial symmetry Figure 2.3, which can be described using Jones calculus with the following matrix:

$$\begin{pmatrix} \cos^2\theta + i\sin^2\theta & (1-i)\cos\theta\,\sin\theta \\ (1-i)\cos\theta\,\sin\theta & i\cos^2\theta + \sin^2\theta \end{pmatrix} \qquad \text{Eq. 34}$$

where angle $\theta=\psi+\pi/4$ and ψ is a polar angle. Multiplying a vector describing the left-handed circular polarization by this matrix the following expression is derived:

$$\begin{pmatrix} \cos^2\theta + i\sin^2\theta & (1-i)\cos\theta\,\sin\theta \\ (1-i)\cos\theta\,\sin\theta & i\cos^2\theta + \sin^2\theta \end{pmatrix} \frac{1}{\sqrt{2}}\begin{pmatrix} 1 \\ i \end{pmatrix} = \begin{pmatrix} -\sin\psi \\ \cos\psi \end{pmatrix} e^{i\psi} e^{i\pi/4} \qquad \text{Eq. 35}$$

This enables fabrication of advanced optical components (similar to q-plates) that are capable of generating beams with radial and azimuthal polarization. The s-waveplte can operate as a polarizing retarder without the capability for any degree of freedom regarding the polarization conversion, but with much higher laser damager thresholds.
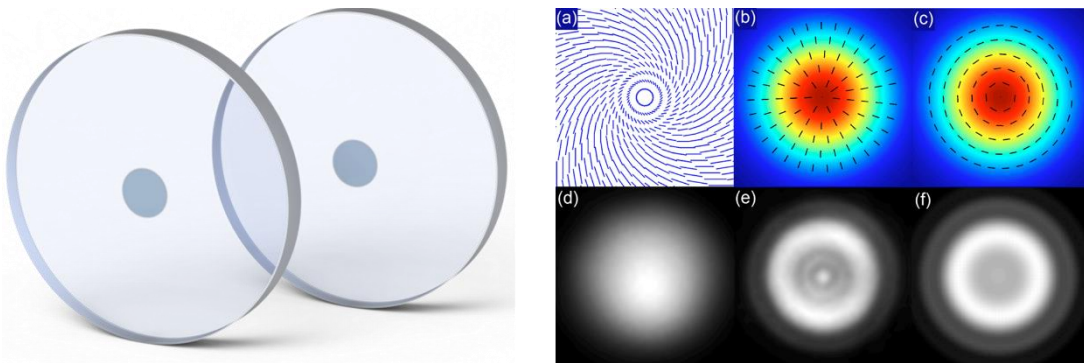
Fig. 2.3: Actual image of the commercial optical element (on the left), image reprinted from www.altechna.com. On the right, color online (a) Schematic drawing of nanograting distribution in polarization converter. (b) and (c) Distribution of the electric field for left-hand and right-hand circularly (see white circles) polarized beam after passing through the polarization converter. (d) and (e) Measured beam profiles before and after beam converter. (f) Modeled beam profile after beam converter. Image reprinted from ref [125].

2. Experimental methods

We have previously demonstrated that the availability of such beam shaping elements for laser processing has already led to the fabrication of highly complex self-organized structures[126]. So, in principle we exploit the functionalities of LIPSS in the bulk of glass to be able to extend our control LIPSS in the surface.

2.4 Dynamic surface processing with Gaussian and CV beams

Dynamic surface processing is defined as repetitive irradiations in a single or multiple direction with laser pulses. In this case, the sample is in constant motion with controlled velocity on the x and y axis and fixed position on the z-axis. For line scanning with focused laser pulses an effective number of pulses N_{eff} must be introduced in order to define and correlate the attained surface morphology of the line scans with the static irradiations (multiple pulses on a single spot).

In the case of a laser beam with Gaussian spatial intensity distribution the line or area scanning, effective number of laser pulses can be defined per length unit or per area unit. The actual Gaussian beam diameter ($2w_0$) (at the $1/e^2$) or the corresponding beam waist area (πw_0^2) can be the measuring factor. Expressing the number of laser pulses which fall, upon one-dimensional (linear) scanning, into a length interval equal to the Gaussian beam diameter $2w_0$.

For "line scanning" at a constant velocity v *(mm/s)* and at a pulse repetition rate f *(Hz)*, the effective pulse number $Neff_{line}$ can be defined as:

$$Neff_{line} = \frac{2w_0 f}{v} \qquad\qquad Eq.\ 36$$

Subsequently for area scanning by repetitive line scan overlap at a line distance (δ), the number of laser pulses which fall, upon two-dimensional (area) scanning ($Neff_{area}$), into an area equal to $\pi(w_0)^2$ can be expressed as*:*

$$Neff_{area} = \frac{\pi w_0^2 f}{v\delta} \qquad\qquad Eq.\ 37$$

In case of line or area scanning with CV beams the N_{eff} should be defined per unit length or unit area respectively. In case of a CV beam and for line scanning at constant velocity v, using a repetition rate f, the effective pulse number $Neff_{line}$ can be defined with Equations (36) and (37) by replacing the w_0 with (R-r). Where R is the radius (μm) of the CV beam

and *r (μm)* corresponds to the central null disk radius exhibiting nearly zero intensity.

2.5 Experimental set up

The experimental apparatus developed and used for the direct laser processing of the all samples in this thesis is schematically and, in a photograph, presented in Figure 2.4. A Pharos-SP laser source from Light Conversion with an Yb:KGW active media was utilized to produced linearly polarized pulses of 170 fs, with tunable repetition rate ranging from single shot to 200.000 kHz and 1026 nm central wavelength with the possibility of 513nm second harmonic output.
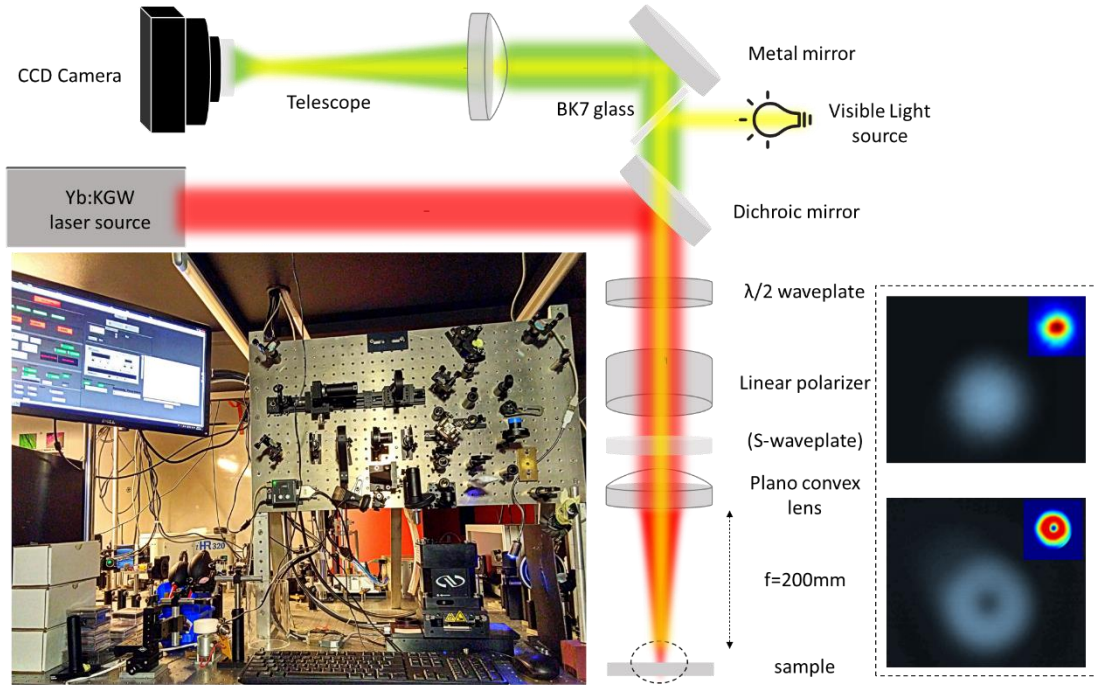
Fig. 2.4: Photograph and schematic representation of the experimental set up developed and used to conduct all of the experimental procedures on this thesis. The beam profiles for both Gaussian and CV beam are presented on the left.

The laser pulses were focused in all of the thesis experiments on each sample via a plano-convex lens of 200 mm focal length while the Gaussian (and CV) spot diameter, measured by a CMOS camera within the Rayleigh length of the focal plane at *1/e²*, was ∼49μm diameter for the IR and ∼27μm for the second harmonic. Typical beam profile images are presented at Figure 2.4 on the black dashed box on the left, along with intensity insets on every beam profile image taken at 1026nm and 1kHz. All the samples were mounted onto a 3-axis motorized servo stage from Newport and positioned perpendicular to the

incident beam. A CCD camera mounted above the sample were used to visualize in situ all experimental process on the sample surfaces. While all the irradiations were performed in ambient environment at normal incidence (~90 degrees). At the same time, power modulation was achieved by means of an automatically rotating zero-order half wave plate behind a high extinction ratio (10000:1), glan-taylor linear polarizer. The polarization conversion from linear to radial and azimuthal was realized with the use of an s-waveplate as discussed at chapter paragraph 2.3 above.

2.6 Characterization methods

2.6.1 Period measurements & Fourier analysis

To characterize the laser fabricated LIPSS structures, besides monitoring its geometry and shape, the LIPSS periodicity and topography and its respective dispersion should be accurately estimated. For this purpose, the scanning electron microscopy (SEM) and (AFM) images of the irradiated surfaces were examined thought image analysis software such as imageJ and Gwyddion and in most cases statistical measurements were performed for the best possible approximation of the surface morphological features. The exact procedure of the transformation and subsequent analysis is presented in the following paragraphs.

2.6.1.1 Two-dimensional fast Fourier transform surface image analysis

In order to be able to extract spatial frequency information a 2D fast Fourier transform (2D-FFT) transform was employed. High-resolution (1280x1024) SEM pictures had been transformed in reverse space images via a 2D-FFT algorithm. The new dimensions of the generated Fourier images are inversely proportional to x and y dimensions of the original image. Figure 2.5(a, b) presents a typical SEM image of an irradiated laser spot using azimuthal polarization. While Figure 2.5(c) shows the corresponding Fourier space image. The orange line represents the direction vertical to the ripple nanostructure.
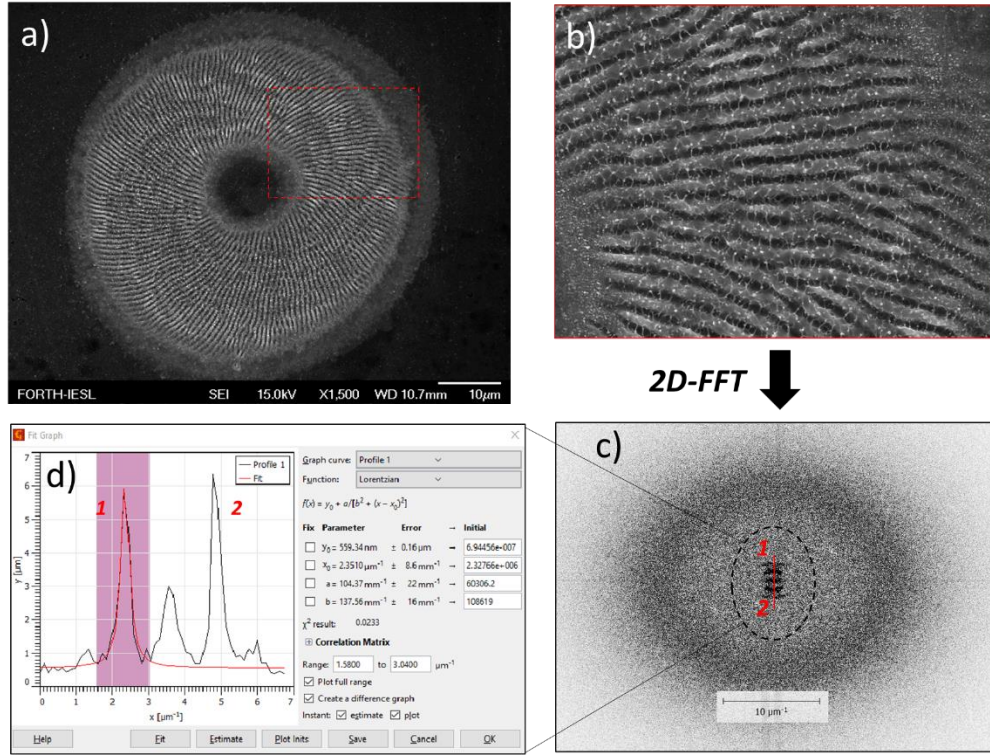
2. Experimental methods

Fig. 2.5: SEM images of ripple formation on nickel surface, (a) Laser spot, (b) higher magnification of the red box on (a). Image (c) represents the 2D-FFT of the image (b) without the labels on the bottom. The cross section of the black dashed ellipse of the Fourier space image (c) in presented on image (d) with peaks 1, 2 to correspond on the intensity of the attained characteristic frequencies in the Fourier space.

Along this direction the Fourier transformation detects a periodical fluctuation of the frequency intensity. This fluctuation exhibits an average frequency which is inversely proportional to the average ripple period. In particular, the distance between the centre of Figure 2.5(d) and the first peak represents the characteristic frequency f of the periodic structure. In order to calculate the periodicity, Λ, of the structures first we calculate the average frequency of *1* and *2* peaks for a vertical as well as a horizontal image cross section (Figure 2.5(d)), and then the average period is, given by the relation $< \Lambda > = 1/f$.

For the estimation of range of frequencies involved into the respective 2D-FFT images, we applied a Lorentzian fit on both peaks of the cross section and the error of each measurement is calculated using the following relation:

$$\Delta\Lambda = \left| -\frac{1}{f^2} \right| \Delta f \qquad\qquad Eq.\ 38$$

were Δf is the mean of the linewidths for the two Lorentzian fit curves of the 2D-FFT image profile peaks.

2.6.2 Material targets

In the following Table, the materials used as targets for irradiation and surface modification with ultrashort laser pulses in every thesis chapter. Both bulk and thin film materials are included with its natural properties and physical dimensions. Also, the irradiating parameters and LIPSS type is given for every material and the possible functionality of each material and process respectively.

Table 1: summarized the materials used as targets for irradiation and surface modification with ultrashort laser pulses.

Material	Crystal structure	Physical dimensions	Irradiation parameters	Chapter	Functionality
Bulk Nickel (Ni)	Poly-crystalline Face-centered cubic (fcc)	Square plates of 1.0 cm diameter and 0.5mm thickness	1kHz, 1026nm, 170fs	3	Multi-directional LIPSS
Austenitic Stainless-Steel Alloy (1.4307) (X2CrNi18-9)	Poly-crystalline Face-centered cubic (fcc)	Square plates of 2.5cm diameter and 1.0mm thickness	1kHz, 1026nm, 170fs	3	Omnidirectional Iridescence
Silver Phosphate glass ($AgPO_3$)	Amorphous	Round plates of 1.5cm diameter and 0.5mm thickness	1kHz, 1026nm, 170fs	4	High order erasable and re-writable gratings
100nm Nickel (Ni) film	Poly-crystalline Face-centered cubic (fcc)	100nm thick Ni films on Square ($4cm^2$) SiO_2 plates (1mm thick) and Round Al_2O_3 plates (1mm thick)	1 – 60kHz, 170fs, 1026nm & 513nm	5	Polarizing plate (wire grid polarizer)

2.6.3 Instrumentation

2. Experimental methods

All of the characterization methods and instruments used for optical, morphological, topographical and chemical analysis in this thesis are summarized below in Table 2. The characterization of the morphological features of the irradiated samples was carried out by different techniques including optical microscopy (OM), scanning electron microscopy (SEM), atomic force microscopy (AFM), depending on any specific experiment. The analysis of the images was carried out using open source software as ImageJ and Gwyddion. In addition, further techniques such as UV-Vis spectroscopy, Fourier-transform infrared spectroscopy (FTIR), Ultraviolet–visible spectroscopy (UV-VIS) were used for optical characterization and Energy-dispersive X-ray spectroscopy (EDX) were available and used to collect more information on phase study and elemental analysis when appropriate (see Table 2).

Table 2: Summarized the characterization techniques along with instrumentation specifications.

Scope	Instrument	Observation	Specifications
Surface analysis	Field Emission Scanning Electron Microscope (FESEM)	Surface Morphology	JEOL 7000F, equipped with a Shottky field-emission electron gun and a secondary electron detector. The resolution is 1.2 nm at 30KV and 3.0 nm at 1.0KV. The magnification range is x10 to x650000
	Atomic Force Microscopy (AFM)	Surface Morphology and Topography	Digital Instruments - Multimode microscope was employed with piezo scanner J (scan size: 125μm×125μm, vertical range: 5μm) working in the tapping mode by using sharp tips (radius of curvature 5-10 nm) from Veeco.
	Optical Microscopy	Surface imaging (up to 100x resolution)	Leica DM2700 M
	Energy Dispersive X-Ray (EDX)	Qualitative and Quantitative Surface Chemical Analysis	Oxford Instruments (INCA). The X-ray Detector is Si (Li) with a resolution of 137eV at 5.9KeV.
Spectroscopy	Ultraviolet–visible spectroscopy (UV-VIS)	Optical characterization	PerkinElmer Lambda 950 UV-VIS lamda 950 spectrometer with an integration sphere
	Fourier-transform infrared spectroscopy (FT-IR)	Polarization Response in the IR – Mid-IR	Bruker Vertex 70v FT-IR vacuum spectrometer, in a spectral range of 1.33-28.6μm (7500 - 350cm^{-1}).

3 Surface processing with cylindrically polarized fs laser pulses

Abstract

This chapter's aim is to provide useful tools for surface processing and explore the physical mechanisms that govern LIPSS formation with locally variant polarizing laser beams such as cylindrical vector beams (CV) beams. In this chapter, a combined experimental and theoretical investigation will be followed to explore ways to control the spatial orientation of LIPSS structures via azimuthally and radially polarized laser pulses. Furthermore, the material response to irradiation with such beams will be discussed along with promising surface functionalities.

Introduction

As discussed previously in chapter 1, one of the most important parameters related to the LIPSS formation is the beam polarization state[127]. It is generally known that irradiation of metals with linear polarized laser light gives rise to LIPSS oriented perpendicular to the incident electric field vector. In this context, the symmetry of the direction of the E-field vector of the radial and azimuthal polarization states, introduces a new approach for surface processing[118,119,128–130] providing further ability to tailor the optical, mechanical and chemical surface properties. The diversity of fabricated structures and the broad spectrum of available materials could therefore facilitate realization of various surface properties, including broadband, hierarchical, multi-directional, surface plasmon effects[8,126]. Despite these versatile and promising applications, few studies have investigated the utilization of optical vortex beams for LIPSS surface structuring.

In this chapter, experimental and theoretical results will be discussed with static and dynamic irradiations on Nickel surfaces. The choice of pure Ni surfaces is attributed to the fact the we needed a pure material for the theoretical investigation, and Ni resistance in oxidation and rust will affect at least our study on the surfaces without extensive

corrosion. Furthermore, the relative abundance of the element in nature and broad range of industrial applications it is used made our choice much easier. The complex polarization states like radial and azimuthal, which were discussed in chapter 2 will now be exploited to investigate the morphological characteristics that induce to metal surfaces as well as their effect on the fundamental physical phenomena that lead to surface modification, always in comparison with a typical linearly polarized gaussian laser beam.

Furthermore, large Stainless-steel surfaces are fabricated with the CV and gaussian fs beams that could potentially be an important tool for structural coloration[131,132], and information marking elements[133] on metal surfaces.

3.1 Static Irradiations with gaussian and CV beams on Ni surfaces

In a first step, the characteristics of laser-induced structures formed upon variation of the NP (*1–1000* at a constant fluence of *0.24 J/cm²*), as well as the incident *φ= 0.17 J/cm²–0.74 J/cm²*, at a constant NP = 100) of the CV beams, was investigated. The central laser wavelength was *λ= 1026nm* with *f=1kHz* repetition rate and 170fs pulse width. All the static irradiations were performed in ambient conditions at normal laser beam incidence (~89.9⁰) and the sample was fixed in a specific z-position within the focusing Rayleigh range. SEM imaging of the respective spots indicated that for *NP<5* no periodic structures were formed in the whole range of fluences used. While, from *2 ≤ NP ≤ 5*, surface roughness was significantly increased and resembles a nanostructured grating with a tendency to orientate parallel to the incident polarization similar to the HSFL structures previously discussed on chapter 1.2. For higher *NP*, the resulting surface comprises a central microstructure formed in the inner region of the CV beam, exhibiting almost null intensity, while the donut area was always decorated with a characteristic texture of LIPSS, always aligned perpendicular to the laser polarization. Accordingly, LIPSS produced with azimuthally polarized light showed radial spatial distribution, while LIPSS obtained with radial polarization exhibited a concentric ring spatial distribution. Figure 3.1 presents typical examples of SEM images of such structures for Gausian linear, CV radial and azimuthal polarization respectively at *NP=50* and *φ=0.24J/cm²* irradiation conditions. The morphological features of the statically irradiated Ni surfaces show a linear and parallel ripple formation for the linear polarization (Figure 3.1(a,b)) with periodicity close to the laser irradiation wavelength (1026nm). Remarkably spot profiles

attained with the azimuthal polarization as depicted in Figure 3.1(c, d) resemble a doughnut shape with radial ripple distribution and a null in the center of the spot caused by the electric field cancellation leading to almost zero intensity. This zero intensity null is also observed in vortex beams, beam that carry an orbital angular momentum regardless the polarization state and it is referred as a phase singularity[134]. Similarly, for radial polarization the spot profile has the same characteristic doughnut shape only this time the ripple formation in exhibiting a vortex-like pattern aligned vertically to the radially distributed electric field charges (Figure 3.1(e, f)).
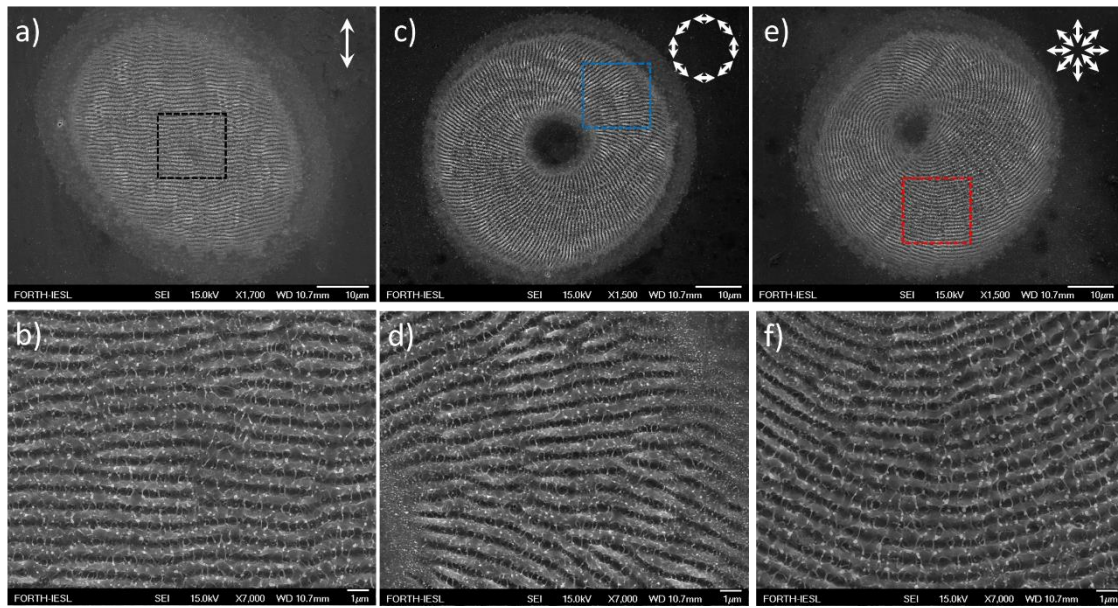

Fig. 3.1: Top view SEM images of fs laser-induced structures formed on Ni surfaces upon irradiation with linear (a,b), azimuthal (c,d) and radial (e,f) polarization states respectively, using φ= 0.24 J/cm2 and NP= 50. Images (b), (d) and (f) are higher magnifications of the white-blue-red dashed-square areas for every polarization state respectively. The white double ended arrows denote the electric field state.

In order to study the effects of the polarization on the laser spot we performed periodicity measurements according to the chapter 2.6.1.1. The periodicity measurements were carried out on every SEM top view laser spot, accounting the whole laser spot for linear and four measurements of every quarter for the doughnut spots.

The results from the parametric analysis, described above, showed that, regardless the polarization condition and LIPSS orientation, the LIPSS periodicity decreases with NPs, (Figure 3.2(a)) while it is weakly influenced by the incident fluence (Figure 3.2(b)). At the same time, the crater depth and thus the height of the microstructure formed at the spot

center of the CV beam can be changed, upon increasing *NP*, the laser fluence and focusing conditions, in the range from hundreds of nanometers to several microns.

As shown in Figure 3.2, the LIPSS period progressively decreases for *5 < NP < 600*, with a trend to saturate at higher NPs, an effect which is valid for both Gaussian (linear polarization in Figure 3.2 and CV beams. On the contrary, LIPSS period is weakly dependent on the incident fluence, despite the spatial profile and polarization of the beam. This behavior has been attributed to the ripple depth increasement with repetitive pulses and the coupling of the SPP with the already formed grating-like roughness. The ripple Λ decrement has been recently addressed by one of our previous communications[8] , via a combined theoretical and experimental study, which showed that it can be attributed to a synergy of electrodynamic and hydrodynamical effects[49]. Figure 3.2(c–e) also presents the 2D-FFT analysis used to determine the ripples periodicity, performed on typical SEM images of spots created by linearly, azimuthally and radially polarized beams respectively.

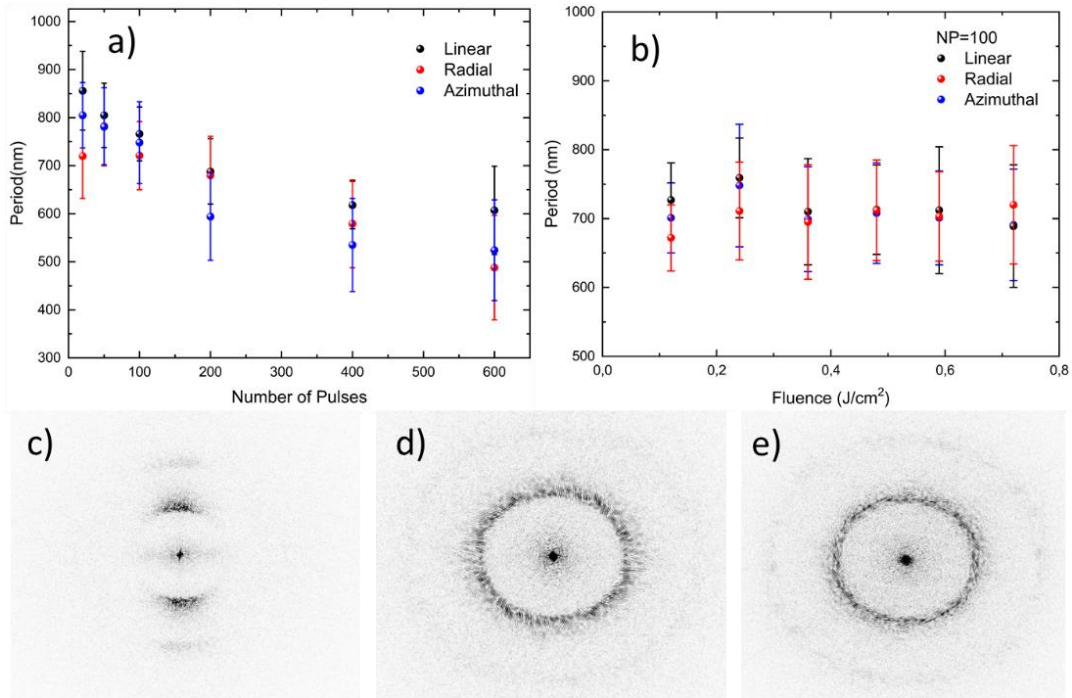*Fig. 3.2: LIPSS dependence on (a) the number of pulses and (b) the fluence for the linear (black), radial (red) and azimuthal (blue) beams respectively. The 2D-FFT analysis corresponding to the SEM images (d), (d) and (f) of Fig. 3.1 is demonstrated.*

It can be observed that the 2D-FFT image characteristics reveal the polarization type and confirm our observation for the ripple distribution as it exhibits a preferential

directionality for linear, a radial distribution for azimuthal and a vortex-like pattern for radial polarization respectively. While the detailed analysis that was performed on the SEM images in order to extract the average periodicities along the standart diviations for every laser spot was dicussed in detail at chapter 2.6.1.1. Furthermore, it is observed that the periodicity values attained with radial or azimuthal polarization have a slightly decreased periodicity when compared with the typical linear polarization, although we can observe this trend the periodicity values are in most cases overlaping within the standart deviation of each measurement as we can see on Figure 3.2. In order to validate these periodic trend we have to examine the amount of the energy absorbtion that is induced for the linearly and radially polarized laser pulses and wheather it is in accordance to our experimental findings.

3.2   Effect of radial polarization on the formation of LIPSS

To explain the surface patterning results, it is important to underline the physical effects that account for the surface modification upon irradiation of Ni with vectorial and linear polarized laser pulses; to this end, a multiscale modelling of the processes that describe laser beam energy absorption and response of the material has to be implemented. The thermophysical and thermomechanical properties of Ni were taken from [46,135–137]. In the simulations (performed by Dr. George Tsibidis), a detailed theoretical model was used that comprised the following components:

(i)   A term for the energy absorption

(ii)   A term that describes electron excitation,

(iii)   A heat transfer component that accounts for electron-lattice thermalization through particle dynamics and heat conduction and carrier-phonon coupling.

(iv)   A term that described a phase transition, molten material movement and resolification that eventually led to surface modification.

In principle, the absorbtion processes starts immediately, from the moment the pulse irradiates the surface. It is followed by the electron exitation and relaxation mechanisms that complete after some picoseconds (ps), while phase transtion, resolidification are the last stage which require more time as they last up to several nanoseconds (ns). It is also important to note that with higher energy deposition other physical phenomena (i.e. ablation, spallation, etc.) that can have significant effects of the surface morphology, however, the laser beam conditions used in this work are not sufficient to produce such

effects. In the rest of this section, the components that constitute the theoretical framework are described [138].

Irradiation of Ni with a radially polarised CV beam, is assumed, in which the electric field of the beam is typically expressed as the superposition of orthogonally Hermite-Gauss HG_{01} and HG_{10} previously described at chapter 2.2.2 (equation 32). To compute the energy absorption, heat transfer and relaxation process the temperature dependence of the thermophysical parameters is considered [136]. A minimal mass removal (i.e. we call it 'sub-ablation conditions' to distinguish effects resulting from the normal 'ablation conditions' that assume plume formation, presence of ejected fragments, etc) [49].
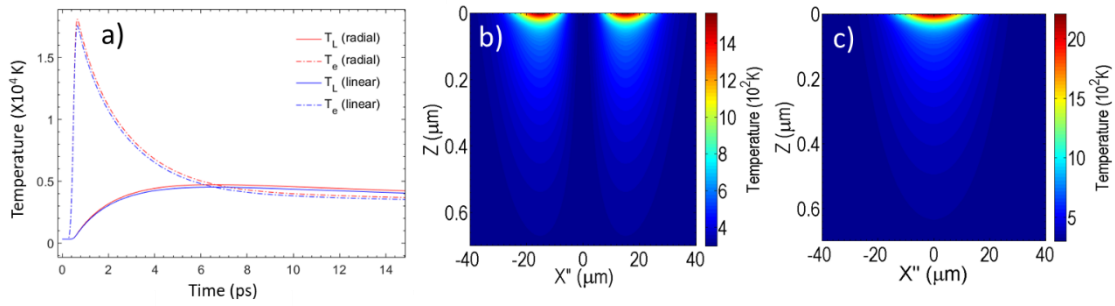

Fig. 3.3: (a) Comparison of electron and lattice temperatures for RP and LP beams for J=0.24J/cm2(NP=1, τp=170fs). Lattice temperature profile at t=20ps (NP=1) for (b) radially polarized CV beam and (c) linearly polarized Gaussian beam.

Simulation results for the electron and lattice temperatures show the evolution of temperatures for various fluences (for melting conditions). The electric field spatio-temporal distribution and the associated intensity is incorporated into the source term of the revised TTM [139] as it was briefly desctied at paragraph 1.3.2, which is solved to derive the heat transfer, electron-phonon relaxation, heat lattice temperature and fluid dynamics in the formed surface tension gradient. In the model, interband transition contributions are also assumed [33].

It is evident radial polarization produces slightly higher temperatures and delay of the electron-phonon relaxation (Figure3.3(a)) with respect to linear. The spatial distribution of the lattice temperature is illustrated in Figure 3.3(b,c) which illustrates the temperature spatial lattice temperature variation at t=20ps that results from consideration of SPP excitation for *NP=1*, for *φ=0.24J/cm²*. Lattice temperature values determine the region where lattice displacements will be dictated by hydrodynamics and surface-tension related forces (where $T_L>T_{melt}$) or mechanical effects (where $T_L<T_{melt}$). In case of phase transformation, the movement of the molten material is expected to induce

two craters around the region of highest temperatures due to the CV beams, ring shaped intensity profile.

Phase change and resolidification process is incorporated into the model by solving the Navier-Stokes equation. A finite-difference method in a staggered grid is employed to solve numerically the heat transfer equations (i.e. by solving the differential equations that describe the two temperature model previously described at chapter 1.3.2) [49], phase change and dynamic elasticity equations [139]. Plastic effects are considered when the total stress exceeds the yield stress of the material [139]. Simulation results for the electron and lattice temperatures show the evolution of temperatures for various fluences (for melting conditions). It is evident that radial polarization produces slightly higher temperatures and delay of the electron-phonon relaxation (Figure 3.3).

A comparison of the theoretical predictions with the experimental results regarding the LSFL periodicity is illustrated in Figure 3.4 for both the radial polarization and the linear polarization cases, under identical irradiation conditions. It is observed that irradiation with radial polarization results in a reduced ripple periodicity, compared to that derived using a linearly polarized beam. The respective simulations indicate that this deviation can be attributed to both electrodynamic and hydrodynamical effects. In particular, as the local energy deposition on the material is higher and is diffused to larger depths for the radial polarization case, it produces an increased maximum of the energy displacement at smaller Λ/λ (for subsequent irradiation), which means that the grating wavelength will decrease. Besides this, the results obtained with radial porarization exhibit higher lattice temperature which, in turn, leads to enhanced fluid vortex development that further decreases the ripple periodicity [49].
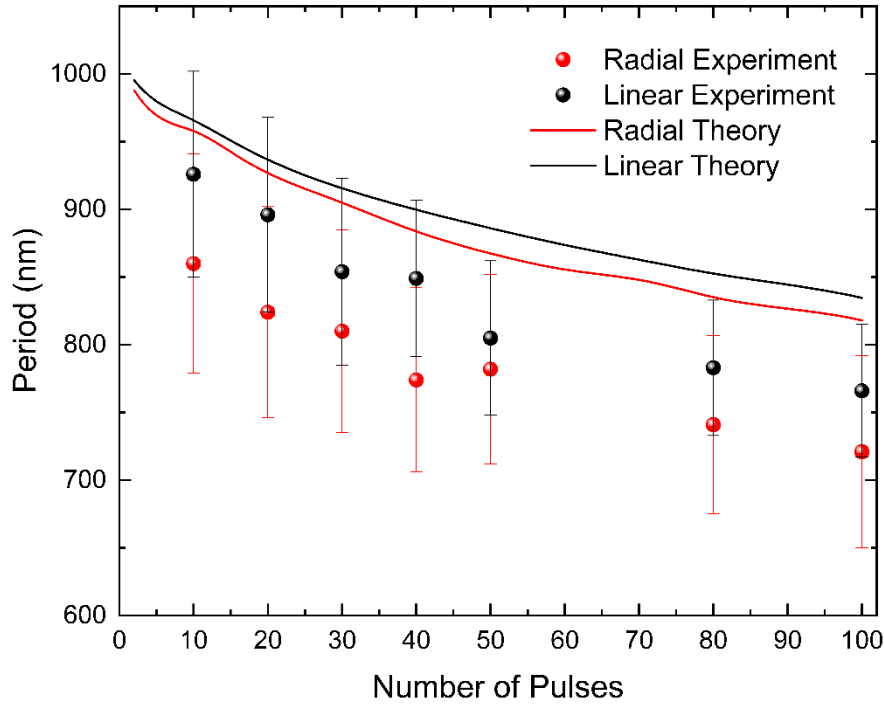
Fig. 3.4: Comparison of ripple periodicity vs. NP at 0.24 J/cm² for radially and linearly polarized beams. Both the experimental observations and theoretical predictions are presented in each case.

Results on the pulse number dependence of ripple periodicity demonstrate a good agreement between the tendency of the experimental observations and theoretical predictions (Figure 3.4). Furthermore, for both types of polarization, the irradiation fluence does not appear to influence substantially the ripple periodicity as previously observed at Figure 3.2(b). In the case of Ni which is a transition metal without completed d bands, the electron heat capacity of Ni strongly deviates from linear electron temperature dependency, while the electron-phonon coupling γ rapidly decreases with increasing electron temperature for low temperatures, followed by a slower decrease as temperature further rises [46]. These properties emphasise the significant role of electron-lattice coupling and electron diffusion in energy confinement and thermalisation that eventually influence size of the laser induced morphological features.

Moreover, LIPSS formation is attributed to the repetitive irradiation of Ni with fs pulses give rise to excitation of SPP (as the real part of the dielectric constant of Ni is (ε_r<-1), although the photon energy and the density of states of Ni indicate that interband transitions dominate its optical properties in the infrared range [140]. Accordingly the already laser induced corrugated surface profile (from the first few pulses) allow SPP excitation [27,49] and correlation of morphological characteristics of the irradiated zone

(depth, and LSFL periodicity, Λ) with the magnitude of the longitudinal wavevector of the SPP requires a systematic analysis of the propagation of the respective electromagnetic field [19,21].

In conclusion, the numerical simulations provided a specific indight into the underlying mechanisms that lead to surface modification upon irradiation of our Ni surfaces for both cases of irradiating polarization. The investigation shows the considerable influence of the incident beam polarization on both the morphological profile as well as the size of the produced periodic structures. The ability to control the size of the morphological changes via modulating the beam polarization is expected to provide novel types of surface structures with significant functionalities.

3.3 Line scanning with radially and azimuthally polarized CV beams

Following spot analysis, line processing experiments were performed in scanning mode, using different scan velocities and spot overlap at a constant ϕ value. Scanning mode as well as the static irradiations were performed in ambient conditions and room temperature. While in the scanning mode the sample is moving along the x-axis or y-axis with constant velocity (v) in the exact same z-position as is was in the static mode. Figure 3.5 exemplifies the characteristic surface morphologies attained, in top-view SEM micrographs of scanned lines, obtained at *v= 0.5 mm/s* (*Neff$_{line}$ = 62*) and *ϕ = 0.24 J/cm²*, for azimuthal (Figure 3.5(a)) and radial (Figure 3.5(b)) CV beams respectively. The *Neff$_{line}$* was calculated with the equation (36) as described at chapter 2.4 accounting the null radius on the center of the CV beam.

Contrary to the, mostly applied to date, linear polarization state, dynamic surface processing with CV beams produces multi-directional rhombus-like structures exhibiting a radial or azimuthal directionality respectively. The LIPSS formed with the used of radial and azimuthal polarization show an unpresented omnidirectionality in their orientation which is directed in almost any possible direction but also exhibit significant differences in their geometrical features. The multiple directionalities are attributed to the spatially variance of the local electric field oscillations of the vectorially polarized CV beams, taking into account that the beams' polarization is oscillating in every possible direction with a profound symmetry as described in chapter 2.2.2.
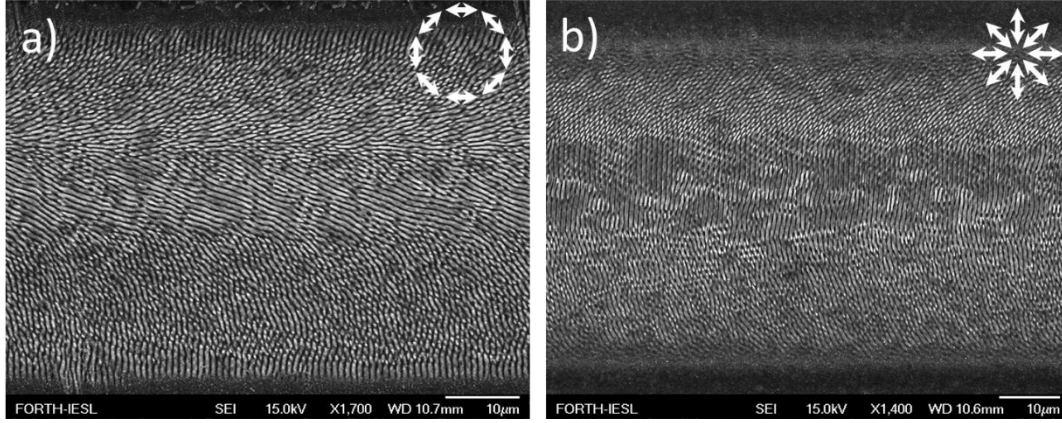
Fig. 3.5: Top view SEM images of line scans with (a) azimuthal and (b) radial polarization state at Neff$_{line}$ =62, φ=0,24J/cm².

As presented in Figure 3.5, it was revealed that the central part of the scan lines is patterned with LIPSS exhibiting relative linearly, which is totally depending on the CV beam focusing conditions used for scanning and the zero-intensity null is the center of the doughnut spot as discussed above. While, the line scan peripheral areas are textured with rhomboid structures. The differences in the geometrical features, observed especially on the edges of the line scans can be attributed to the pulse to pulse overlap caused by the beam advances on the surface during scan, the pulse overlapping effect leads to crossed vector peripheral areas, leading eventually rise to the rhombic-shaped structures. Such structures form as the natural outcome of the overlap between successive CV beam spots, specifically as the beam advances on the surface during scan, the pulse overlapping effect leads to crossed vector peripheral areas, giving rise to the rhombic-shaped structures. According to the above, the scanning speed that determines the degree of overlap should play significant role on the patterns' morphology attained.

The attained morphological changes of the structures presented at Figure 3.5 exhibit notable differences with respect of many previous studies[6,84,141] in which linearly polarized fs pulses were used on metal surfaces; the overall periodicity of the LIPSS is slightly affected within the standard deviation of the period measurement. These are wavelength LSFL structures and exhibit and average periodicity of ~890nm ±62nm measured in the SEM images for eight times with a 45-degree difference.

3.4 Omnidirectional iridescence on steel surfaces

As previously discussed, the fabrication of LSFL in the form of parallel fringes with great spatial accuracy and homogeneity are possible upon irradiation with ultrashort laser pulses, due to the limited collateral damage and thermal effects. LSFL are thoroughly characterized by their depth, periodicity and orientation. Both periodicity and depth are dependent on the fundamental characteristics of the laser irradiation such as wavelength, intensity and scanning speed[3]. However, their orientation as we saw above, is absolutely dependent on the polarization state of the laser beam. Specifically, for metallic surfaces, LSFL there are numerous reports of their tendency to align perpendicularly to the incident net force of the E-field components for a typical linearly polarized pulse[48,126,142,143]. At this context Vorobyev and Guo have demonstrated the possibility of realizing well-defined structural color via a precise control of periodicity and orientation of LSFL, upon changing various irradiation parameters[144,145]. Following this work, there are numerous reports on the fabrication of structural colors via laser based fabrication approaches [131,132,146], [141,147–149], [150].

Nevertheless, none of the methods reported to date, including the laser-based ones, is capable to produce multidirectional spatial frequency patterns, in a single step. As a consequence, the produced iridescence strongly depends on the viewing angle, thus it exists only for specific angles of incidence and is absent upon tilting the diffraction element [151,152] .Besides this, it has been both experimentally and theoretically reported, that diffraction cannot occur when the plane of light incidence is parallel to grating orientation[76,142]. Efforts have been made in order to overcome the above restrictions with the generation of LSFL in variable orthogonal directions by utilizing the polarization dependence of the ripple orientation. In particular, a grid can be fabricated where each laser scanning direction employs different polarization state such as *p* and *s* polarization respectively[76,153]. Therefore, the surface can produce diffraction in two different planes of incidence. Also, it has recently been reported that irradiation with circular polarization pulses can form triangular periodic surface structures that could potentially significantly increase the range of incident light-illumination angles[154]. Despite these efforts, omnidirectional iridescence has not yet been realized via a single-step irradiation process.

Following the previous results of this chapter we present, an effective, simple and single-step technique for the fabrication of diffractive surfaces, exhibiting iridescence with great

efficiency for any angle of incidence. This is realized via large-area processing of austenitic stainless steel (1.4307) with radially polarized cylindrical vector (CV) fs laser beams[126], leading to the formation of LSFL, which are spatially oriented in multiple directions as we presented in the previous paragraph. The choice of stainless steel instead of Ni in this section was due to the availability of lager samples which was more convenient for the surface characterization methods we will use below. The only notable difference in stainless steel samples was that the fluence we used to be slightly increased with respect to the value we used for Ni line scanning as presented at Figure 3.5 above.

Large areas of 25 mm² were also fabricated via scanning the fs beam onto the sample surface using the optimized conditions found during the line scanning experiments. Figure 3.6(a-c) illustrates the characteristic morphologies attained for the S_1 samples, using $\varphi=0.45$ J/cm², $N_{eff\text{-}area}=36$, $\delta=32$ μm and $v=2$ mm/s. The corresponding 2D-FFT, frequency spectrum, acquired by the SEM images indicates that the LSFL structures exhibit a single and well-defined directionality, which is perpendicular to the laser beam polarization.
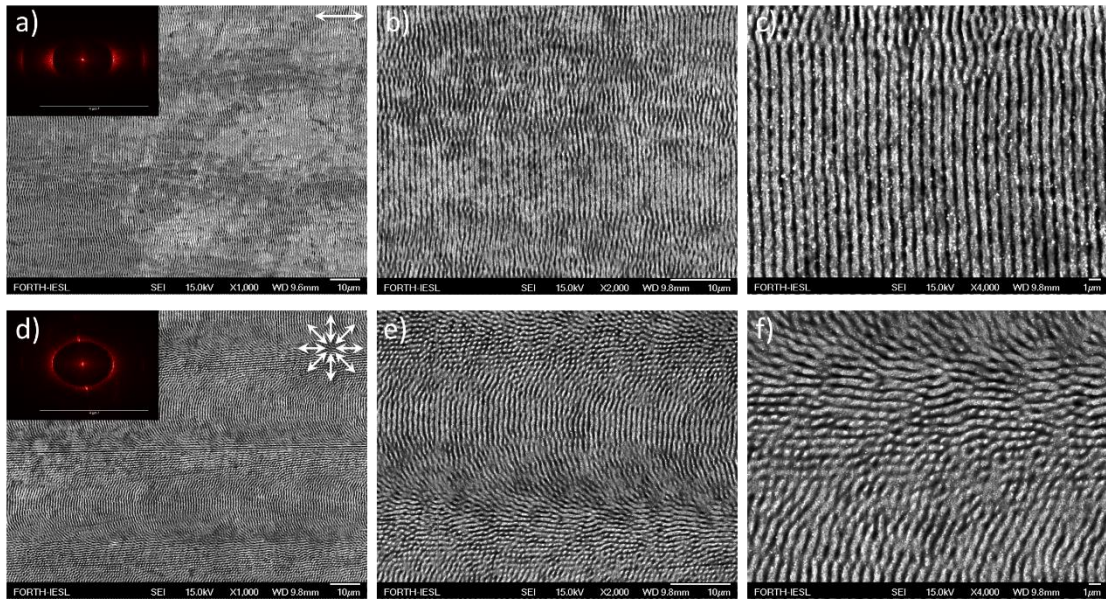
Fig. 3.6: Top-view SEM images of areas produced upon irradiation using linearly, (a,b,c) and radially, (d,e,f), polarized fs beams. The images shown in b,c and e,f are higher magnifications of the images a,d respectively. The areas in a,b,c were fabricated at φ=0.45 J/cm2 and Neff-area=36, δ=32 μm and v=2 mm/s, while those in d,e,f were obtained at φ =0.49 J/cm2, Neff-area=30, δ=34 μm and v=2 mm/s. The white arrows depict the electric field polarization state. The 2D-FFT patterns corresponding to each area are shown in the insets.

The average period calculated by the FFT pattern for the linear-polarized case equals to 870±80 nm. On the other hand, areal scanning with CV beams gives rise to more complex

3. Surface processing with cylindrically polarized fs laser pulses

LSFL structures exhibiting multi-directional orientation (Figure 3.6(d-f)). As previously reported[126], such structures is the outcome of the dynamic evolution of the overlap between successive CV beam spots. Indeed, there are two different kinds of overlap taking place in this case. The first is the pulse overlap between successive CV beam spots as the beam advances on the surface during line scan and the second is the overlap between two successive scan lines. In both cases, the crossing of the electric field vectors between successive CV beam pulses determines the LSFL direction per irradiation area. The corresponding 2D-FFT pattern, presented in the inset of Figure 3.6c, shows no dominant spatial frequency, which confirms the multidirectional nature of the formed structures. The average LSFL periodicity calculated in this case to equals to 850±97 nm.

Following irradiation, all the processed surfaces exhibited vivid coloration, which is expected, considering that the calculated LSFL periodicities are close to the visible wavelengths [155,156].
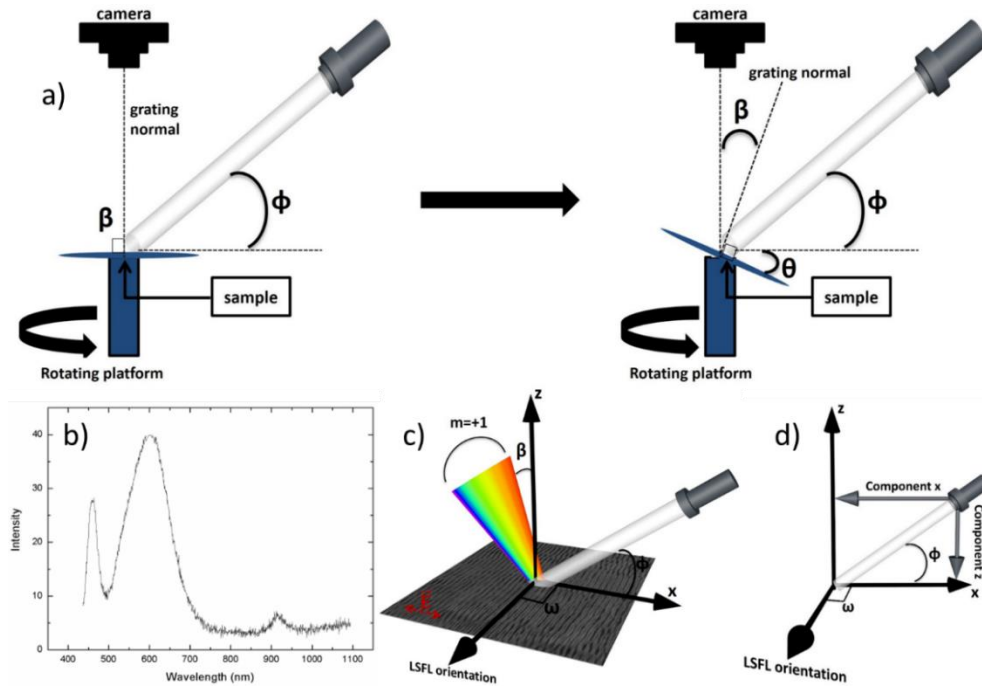
Fig. 3.7: (a) Experimental setup and geometry used for the evaluation of surface diffraction properties; (b) Typical intensity plot of the white light spectrum; (c) Schematic illustration of the structural color monitoring system; (d) the respective coordination parameters.

It is also striking that the S_2 samples are iridescent at practically any viewing angle, contrary to the S_1 ones. Figure 3.7(a) shows the geometry of the used to study the white light diffraction properties of such surfaces, while Figure 3.7(b) depicts a typical light

emitting diode (LED) white light spectrum detected for a specific angle of incidence. Based on the color measuring system, the diffracted light wavelengths can be calculated by the simple diffraction grating equation [156]

$$m\lambda \ = \ \Lambda \left(cos\varphi \cdot sin\omega \ + \ sin\beta\right) \qquad \text{Eq. 39}$$

, where λ is the diffracted wavelength, Λ corresponds to the LSFL period and m is the order of diffraction, in our case $m=\pm 1$ (Figure 3.7(c)). The angle φ denotes the white light incidence, while ω corresponds to the sample rotation within the sample plane. Assuming that θ is the sample tilt angle, the grazing angle equals to $\varphi+\theta$ as presented at Figure 3.7(a,d).

The ability of the surface to act as diffraction grating was tested for 8 different angles ω in order to prove experimentally the hypothesized angle free iridescent when the surface exhibits LIPSS aligned in every direction. We tested for eight different angles ω, starting from 0º to 360º with a step of 45º. The grazing angle can be considered as φ+θ. In each angle ω, the grazing angle was changing and the color change was observed for the visible spectrum while the angle β was recorded in every case. Consequently, the experiment is based on the coordinate system (ω, φ+θ, β). Each color was captured by a SONY DSC-RX100M4 camera that was placed perpendicular to the sample along the z axis.

It is observed that for practically every possible incident angle of illumination, the plane direction of light is always perpendicular to locally formed LSFL, hence reflective diffraction can take place. The ability of the obtained structures to act as diffraction gratings (S_2) (Figure 3.8(a)) was systematically studied and compared against the diffraction originating on the conventional ones (S_1) fabricated using linearly polarized laser pulses Figure 3.8(b). The polar coloration attained images of Figure 3.8 presents in the form of a polar plot of the angle ω the structural coloration in the case of the, single spatial frequency, S_1, surfaces, which is in good agreement with the theoretical predictions [155]. Indeed, no diffraction is observed when the ripples orientation becomes parallel to the *x*-axis (i.e. $\omega=0º$ and 180º). On the contrary, when *x*-axis is perpendicular to the ripple's orientation, i.e. the angle ω was 90º and 270º, diffraction with maximum intensity takes place and vivid structural colors were observed. Diffraction also occurred for the rest of angles ω tested, i.e. 45º, 135º, 225º and 315º, but with a lower intensity and yield. As a result, the structural colors appeared as blurred.

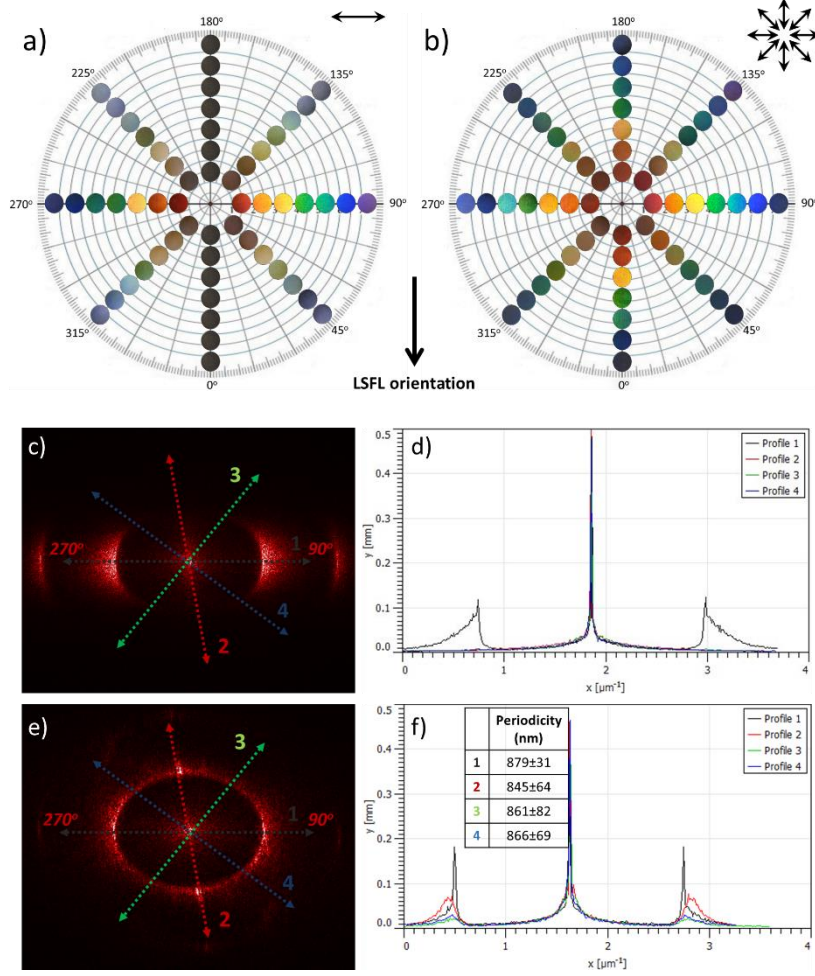## 3. Surface processing with cylindrically polarized fs laser pulses

Fig. 3.8: Schematic illustration of the resulting observed colors (a,b). The (a) corresponds to the colors obtained after the white light is applied to the area irradiated with a linearly polarized beam. Similarly, the (b) refers to the processed surface with radially polarized beam. The angles of the circle correspond to the angles ω of the (a-b). 2D-FFT images for the fabricated areas with linearly and radially polarized beams are depicted at (c) and (e) respectively. Images (d) and (f) are profiles of the dashed lines shown at images (c) and (e).

As mentioned above, the diffraction properties and respective structural colors are quite different for the S_2 series of surfaces fabricated by a radially polarized CV beam. This is due to the formation of multi-directional LSFL structures, giving rise to reflective diffraction, regardless of the rotational angle ω. As a result, the surface is iridescent for practically any viewing angle, although the vividness and sharpness of the diffracted colors are slightly different depending on the angle ω. Specifically, for the angles ω = 0º, 90º, 180º, 270º, the diffracted colors appeared to be most vivid and exhibit maximum rendering capacity, compared to the angles ω = 45 º, 135 º, 225 º, 315 º. This effect is also indicated by the respective FFT pattern (Figure 3.8(c, e)), which shows characteristic hot spots only for the angles where the diffraction is dominant.

The limitation of angles ω where the diffraction occurs was surpassed by the use of a radially polarized CV beam for the fabricated S_1 showed at Figure 3.8 (e-f). As discussed

above, the pulse overlap during the dynamic irradiation with radial polarization causes the formation of complex multi-directional surface structures. As a result, the reflective diffraction is irrespective of the rotational angle ω due to the existence of structures perpendicular to each individual direction. Thus, the white light can be analyzed in all directions, although the vividness and sharpness of the diffracted colors are slightly different for each angle ω. In particular, at the angles $\omega = 0^0, 90^0, 180^0, 270^0$, the diffracted colors appeared to be the most vivid and have maximum rendering capacity, compared to angles $\omega = 45^0, 135^0, 225^0, 315^0$.

At this point it is important to note that the radial intensity of the diffraction colors depends directly on the quantitative sum of the periodic structures that are present in the each observed direction, which we set always perpendicular to the x-axis. In our case a way to quantify this is presented at Figure 3.8(c-f) where the 2D-FFT images for S1 and S2 surfaces are showed along with the relative cross section intensities for four different radial directions Figure 3.8(d,f). More specifically the distribution of the frequencies of the structures in each direction arising from the combination of theory and observations of the results can be confirmed by the Fourier transformation method. The 2D-FFT method provides information about the direction of the dominant structures, that is, the direction that has a higher sum of LIPSS formation. Specifically, four axes were taken. In each case, the axis gives information about the frequency of the structures in the direction perpendicular to that particular cross section axis. In Figure 3.8(e), axis 1 used for the investigation of the frequency of the structures in the direction parallel to ripples orientation axis. Respectively, axis 2 informs about the frequency of the structures that exist perpendicular to ripples orientation axis and cross sections 3 and 4 for the diagonal structures. These four axes are transformed into a common plot of intensity of frequency as a function of length in Figure 3.8(f). This plot shows that the higher intensities belong to the axes 1 and 2, while the lower ones on the axes 3 and 4.

Consequently, it is noticed that the greatest frequencies are in the directions that are perpendicular and parallel to the predefined ripples orientation axis. In more detail, the axis 1 has a greater intensity than axis 2 in the diagram, so the direction that is parallel to ripples orientation axis appears the highest frequency. Moreover, using the 2D-FFT image, the average LIPSS periodicity was calculated in four directions showing ineligible period variations. Indicating that the frequency of the structures remains almost the same, within the standard deviation regardless their orientation for S_2. Figure 3.9 displays analytically all the diffracted colors presented at Figure 3.8(a and b) with the exact values of polar *(ω),* grazing *($\varphi+\theta$)* and diffracted *(β)* angles.

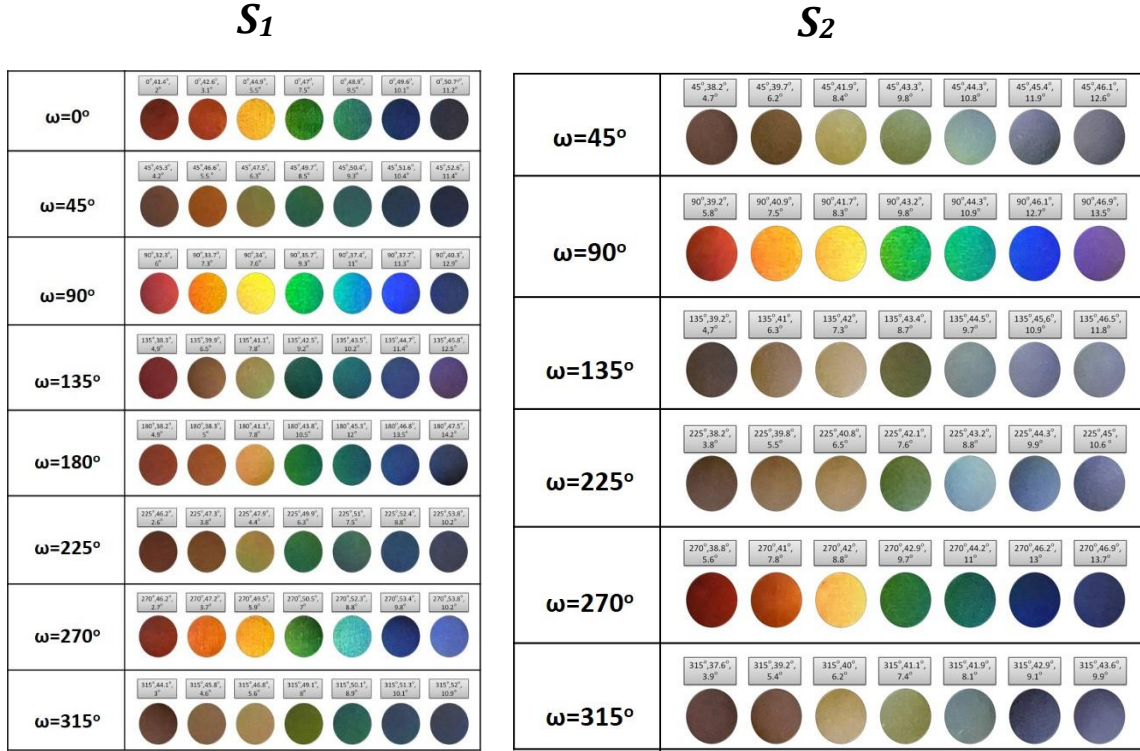## 3. Surface processing with cylindrically polarized fs laser pulses

Fig. 3.9: The resulting diffracted colors obtained by irradiation with white light on the area fabricated with linearly polarized beam for S1. Each color shows up based on the coordinate system (ω, φ+θ, β). The colors obtained by diffraction of white light on the surface fabricated with radially polarized beam. Each color is based on the coordinate system (ω, φ+θ, β) for S2.

The combination of the above leads to the conclusion that the intensity characteristic frequencies of the surface structures in the directions that are vertical or parallel to axis ripples orientation are dominant in diffractive efficiency than the frequencies of the structures in the diagonal directions. Furthermore, it is observed that when the white light impinges in such a way that the angles 90° and 270° are formed, that is, when the light is incident with the x axis being perpendicular to the ripples orientation axis, the colors have the maximum intensity compared to the colors of the remaining angles. Therefore, the direction of structures that dominates is the one that is located parallel to the ripple orientation axis. Thus, when the white light impinges in a way where the x-axis is perpendicular to the ripple orientation axis, the reflective diffraction effect occurs with the maximum intensity of the diffracted wavelengths. However, it is possible following alternative surface processing strategies [126] to control and tune the surface morphology for each observing angle and define the diffraction efficiency for each ω.

This is a novel and rapid technique for the fabrication of large areas of multi-directional laser induced periodic surface structures exhibiting omnidirectional diffraction properties. The diffraction and structural coloration properties are by far different than those exhibited by LSFL areas fabricated via linearly polarized Gaussian beams. Our

results show that it is possible to efficiently tune the diffraction and structural coloration properties via surface processing strategies employing femtosecond CV beams.

4 Erasable & rewritable highly regular LIPSS on AgPO$_3$ glass surfaces

Abstract – In this chapter results on the fabrication of high-regularity, erasable and re-writable periodic surface patterns on silver metaphosphate glass (AgPO$_3$) by means of ultrashort pulsed laser processing are discussed. We show that laser induced periodic surface structures (LIPSS) are formed perpendicular to the laser beam polarization, exhibiting a periodicity similar to the laser wavelength. Notably, the so-formed periodic patterns can be readily erased upon further exposure to femtosecond laser irradiation under controlled conditions. This all-laser inscription and deletion protocol allows the reversible patterning of the phosphate glass surface by employing a single laser beam. This could practically enable infinite cycles of the write/erase/re-write process on the same area of the glassy material, posing the AgPO$_3$ glass as an important candidate for waveguides and optical responsive memory components of advanced photonic applications.

4.1 Introduction

Direct laser processing of transparent materials in the visible spectrum, via femtosecond pulses has been extensively explored over the last decades as it poses tremendous advantages in terms of the patterning of periodic structures that can be exploited in a wide range of photonic devices with remarkable functionalities [141,157–160]. Moreover, the rapid development of femtosecond laser sources over the years allows not only the exploitation of ultrashort pulses, but also, the advantage of creating well shaped light field in both space and time regimes [159,161]. Fabricating periodic structures on the surface and/or within the bulk provides the potential of enhancing advanced optical materials with a wide range of additional applications, including super-hydrophobicity [162,163], fluid transport[164], friction reduction [165], tissue engineering [166], data storage [167], and light manipulation [168].

The formation of (LIPSS) on transparent, dielectric materials as briefly described at chapter 1 can, in general, be interpreted as the photo-excited electron density induced modification of the dielectric properties of the material. To date, the vast majority of glassy materials that are used for laser writing and patterning are based on pure silica[169], while this trend is mainly prompted by the excellent transparency of silica based glassy compounds. On the other hand, pure silica exhibits the highest glass transition and melting temperatures among all glasses[170], i.e. glass transition temperature (T_g) of well above 1000 °C. In this chapter, we demonstrate the inscription of erasable periodic structures on the surface of silver metaphosphate ($AgPO_3$) glass by the means of direct femtosecond laser writing.

The selection of the much softer $AgPO_3$ glass was based on its optical properties (transparent in most of the visible) as well as the electric conductivity which is attributed on the silver nanoparticles may promote SPP excitation and result to similar LSFL structures as presented in the previous chapter. Moreover its elastic mechanical properties and low T_g temperature (with respect to common glasses i.e. silica or soda lime glasses) could be the ideal case for the control of the so-formed surface pattern deletion upon either controlled femtosecond laser irradiation or conventional thermal annealing, and thus, potentially giving rise to infinite writing/erase/re-write cycles. This remarkable reversibility feature is considered extremely important in terms of optical memory storage and thermo-responsive photonic applications, especially due to the fact that it can be an entirely all-laser process. Recently, Lei et al. demonstrated nicely a similar process of writing and eliminating LIPSS on metal glasses by utilizing two temporarily separated femtosecond laser beams[171]. However, to the best of our knowledge, our present study is the first demonstration of such process on transparent inorganic oxide glasses, while being possible to erase the so-formed patterned with a sole laser beam. Furthermore, the selection of the transparent $AgPO_3$ soft glass permits the deletion of patterns by means of both all-laser and/or thermal annealing routes, i.e. depending on the desires of the application.

4.2 Silver metaphosphate glass preparation

The silver metaphosphate glass, AgPO$_3$, was prepared by Dr. Ioannis Konidakis in a platinum crucible by melting equimolar amounts of high purity AgNO$_3$ (99.995%) and NH$_4$H$_2$PO$_4$ (99.999%) dry powders, following a well-established synthesis procedure[172,173]. Namely, all weighing and mixing manipulations of the two powder precursors were performed within a glove bag purged with dry nitrogen gas. Following this, the melting batch was transferred to an electrical furnace initially held at 170 °C, while slowly heated up to 290 °C in order to allow the smooth removal of the volatile gas products. The furnace temperature was then raised to 700 °C, and kept steady for 90 minutes, while the glass melt was stirred regularly. AgPO$_3$ glasses were obtained in the form of ca. 1 mm-thick disc specimens with a diameter of ca. 10 mm, by splat-quenching the melt within two silicon wafers. The latter allows the formation of remarkably smooth glass surfaces that render the samples suitable for laser inscription. It is noted that the aforementioned fabrication protocol results to AgPO$_3$ glasses with minimum water traces of less than 0.3 mol.%, which are proven unable to cause any noticeable changes to optical and/or structural properties [172], while the samples remain unaffected of room humidity (25-30%) for several months.

4.3 Static irradiations and thermal incubation effect

Initially laser parametric study was conducted with single and multiple pulse irradiations varying the laser fluence and the number of pulses[174]. In the static mode the sample is always mounted to a fix z-position on our 3-axis motorized servo stage and in moves only after the irradiation process takes place. Subsequently arrays with laser spots were created with the number of pulses ranging from *NP= 1 - 1000* and the laser fluence used were *φ= (1.20J/cm², 1.74J/cm², 2.20J/cm²)*. The fluence values were selected after performing ablation threshold experiments for *NP= 10*. The single shot damage threshold laser fluence was estimated to be around *φ$_{th}$= 1.12 – 1.22 J/cm²*. The single shot damage threshold is the minimum pulse energy or fluence that is required to induce considerable morphological change with a single laser pulse. For damage threshold unlikely to the ablation threshold there is no material removal and the material surface is just reshaped. In most cases for the fs regime, the damage threshold is lower than the ablation threshold and for materials with dielectric properties in with respect to the amount of the energy, it is distributed in some the three major absorption channels (multi-photon absorption, tunnel effect, and impact ionization)[175]. Moreover, the ablation and damage thresholds

can vary with respect to the *NP*, and the LIPSS formation can occur for multiple repetitive NPs when irradiating a surface of low roughness.

In this context multiple shots of variable pulse number at *φ=2.20J/cm²* are presented in SEM images at Figure 4.1(a) along with high magnifications of the brinks of the beam spots for *NP= 2* (Figure 4.1(b)) which indicate silver nanoparticle clustering spheres and 1000pulses and Figure 4.1(d) with LIPSS formation on the laser spot edges due to the inhomogeneous intensity of the beam. Moreover, a characteristic laser spot of 50 pulses with LSFL-LIPSS formation is depicted at Figure 4.1(c).
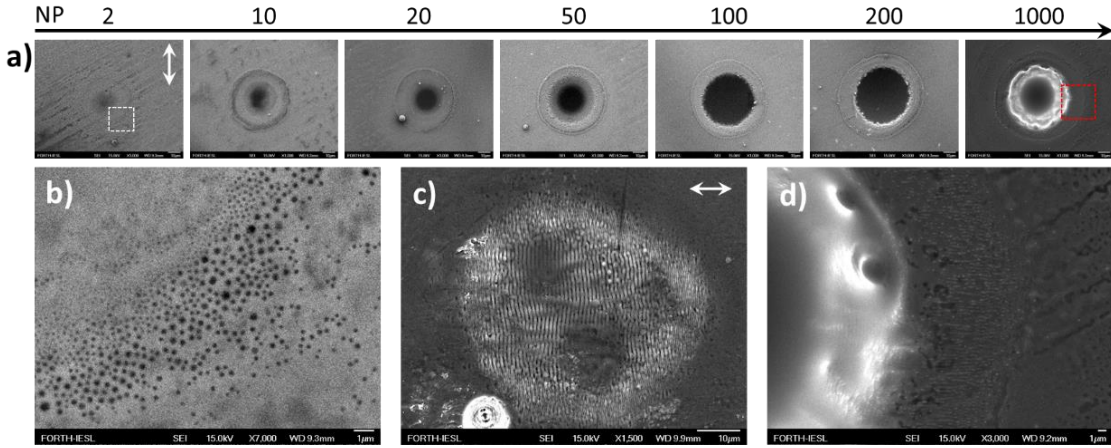

Fig. 4.1:Top view SEM images depicting (a) multiples irradiations at 2.2 J/cm². The highlighted white and red dashed squares are the corresponding (b) and (d) images at higher magnification. And (c) LIPSS formation for 50 pulses and 1.74 J/cm².

Through all static irradiations, it was observed pronounced thermalization and melting of the irradiated surface areas along with significant LIPSS inhomogeneity as presented in Figure 4.1(c). The characteristic SEM image of Figure 4.1(c) presents the laser spot with the most homogenous LIPSS that was currently achieved. It is also important to stress that indications of the LSFL-LIPSS formation were only observed in *φ=1.74 J/cm²* and for the range of *15≤ NP ≤50*. It is also very important to note that for all the *NP* and *φ*, parameters examined there was not a single observation of sub-wavelength structures parallel to the polarization state. On the contrary HSFL structures were observed on the lateral regions of several laser spots that were always perpendicular to the laser polarization and they exhibited almost half the laser wavelength size with a periodicity (Figure 4.1(d)) roughly estimated at *~418nm±70nm*. The period was roughly estimated without the 2D-FFT method presented in chapter 2.6.1 due to sample sufficiency as well as the low order of regularity of these structures, which produce significant noise on the FFT measurement.

Hence their average period was evaluated with manual measurements with ten repetitions on 5 different areas.

The attained non-uniformity of LIPSS, observed in the laser spots can be attributed to heat accumulation[176], and thermal incubating effects[177] due to repetitive number of pulses in the confined (laser spot) area. On the other hand, the material thermal properties intensify this claim, taking into account that the silver phosphates glasses exhibit extremely low glass transition temperature T_g ~190 °C and lower thermal conductivity from the metal surfaces examined in the previous chapter, indicating pronounced thermalization effects in the material surface.

Regardless of the structural homogeneity the LSFL formation on the surface of soft glasses such as the silver phosphate glass can be attributed to an electromagnetic origin. The silver phosphate glass has a band gap of 0.49-0.53eV[172] with the laser wavelength (¬1.2eV) more than sufficient to provoke the excitation of surface plasmon polaritons (SPPs) on the $AgPO_3$ glass surface[141,178] since the carrier density of the material during irradiation exceed the critical carrier density threshold. Hence, the materials real part of the dielectric constant results in negative values, therefore for a finite time the excited material can be considerate as metal as previously discussed at chapter 1 for the case of LIPSS on semiconductors[49,179].

4.4 Fabrication of high order LIPSS on $AgPO_3$ surfaces

In an attempt to reduce thermal incubation and heat accumulation effects we preformed line scans in order to examine the material response when the laser pulses were progressively delivered to the material surface in different location every time (via raster scanning). The results showed significant improvement on the LIPSS homogeneity as Figure 4.2 presents SEM images of the periodic rippled structures formed on the surface of $AgPO_3$ glass. The pristine glass surface is also shown as Figure 4.2(a). The areal scanning was performed with a rate of *2 mm/s*, whereas the employed fluence was *φ=1.74 J/cm²* and the effective number of pulses for the fabricated areas, *Neff_area, was ~330* and the line separation *δ=10*μm. As shown in Figure 4.2(b-d) the obtained structures are always orientated perpendicular to the incident electric field polarization state, exhibiting an average periodicity ranging from 850 to 950 nm.
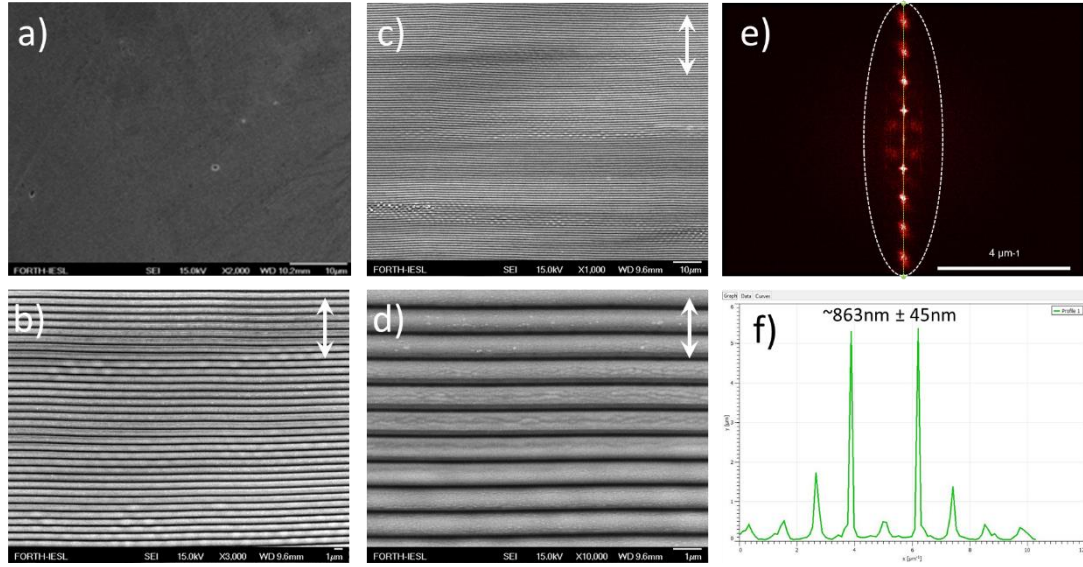
Fig. 4.2: (a) Top view SEM image of pristine AgPO₃ glass surface. (b-d) Top view SEM images of periodic patterns on the surface of AgPO₃ glass following laser irradiation process (LIPSS) in different magnifications. The orientation of the incident electric field state is indicated by the white double ended arrows. (e) Corresponding two-dimensional fast Fourier transform (2D-FFT) of (b) revealing the spatial distribution and the orders of regularity for the fabricated LIPSS. (f) Cross section of the inversed space 2D-FFT image (e), depicting the characteristic high order periodicity of the LIPSS.

The LIPSS analysis regarding their spatial features are presented at Figure 4.2(e), which shows the corresponding two dimensional fast Fourier transform (2D-FFT) of the Figure 4.2(b) SEM image, revealing the spatial distribution and the high order of regularity for the fabricated LIPSS, while the characteristic periodicity of the patterns is extracted by the illustrated cross section of the inversed space 2D-FFT image depicted in Figure 4.2(f). The origin of the high regularity of the LIPSS formed on the AgPO₃ glass surface can be compared with reported LIPSS on pure metal surfaces[141,180]. The spatial features of the created LSFL-LIPSS and its extremely high order and excellent regularity as presented at Figure 4.2 could be potentially used as transmissive gratings[181] for the visible and the near infrared spectrum.

Apart from the soft nature of the AgPO₃ glass, the presence of silver ions provides a system with attractive plasmon and non-linear optical properties that could be further exploited towards functional applications. As for instance, it has been shown that the formation of silver clusters induced by direct laser writing or conventional thermal annealing treatment induces second harmonic generation (SHG) effects [182,183]. In a similar manner, LIPSS can be employed for the formation of metallic silver nanoparticle domains and nanogratings[184,185]. In addition, the plasmonic features of the AgPO₃ glass have made it attractive material also in the field of composite optical fibers[186,187].

4.5 Erasing LIPSS with Laser pulses

Notably, the so-formed surface patterns can be completely erased upon further scanning with the same laser beam fluence and scanning velocity conditions, however, through reducing the overall number of pulses receptive to the surface. This was achieved by slightly increasing the line separation $\delta=18\mu m$, leading to $Neff_{area} \approx 180$. Figure 4.3(a) presents a SEM image that shows a square region where the previously written pattern has been erased. Figure 4.3(b) depicts higher magnification of the erased square of Figure 4.3(a). While higher magnifications are also presented at SEM images at Figure 4.2(c,d)
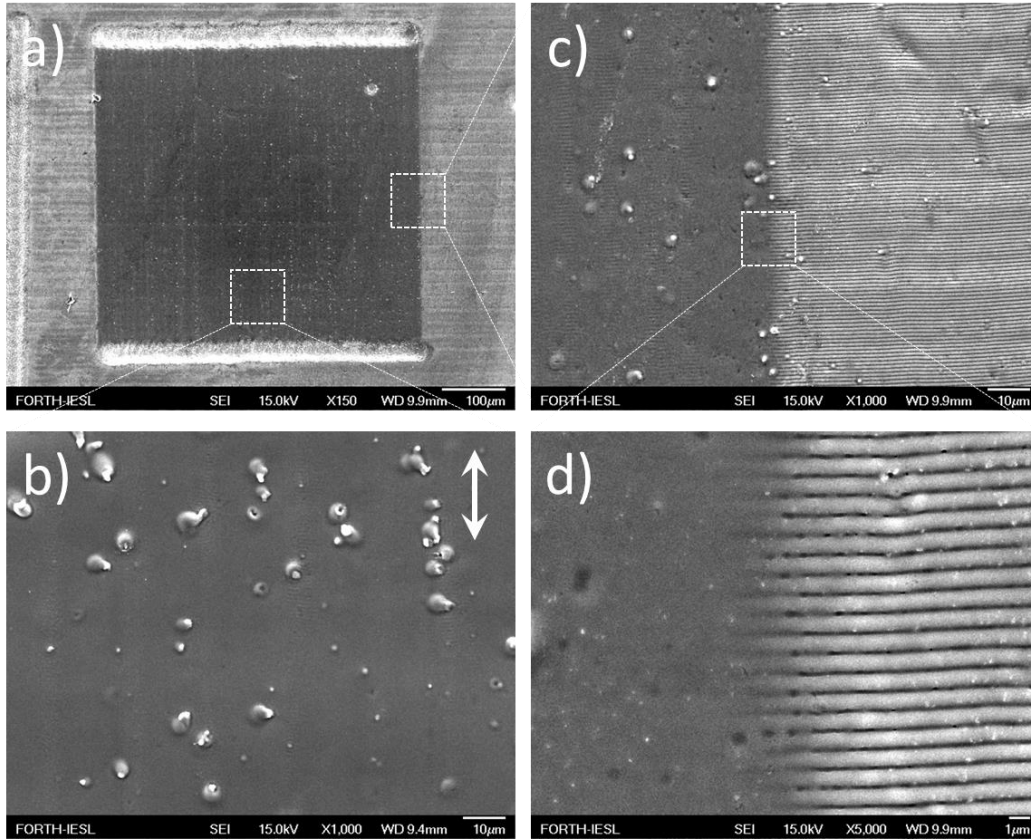
Fig. 4.3: (a) Top view SEM image showing an erased pattern region on the surface of AgPO3 patterned glass. (b) Magnified area of (a) where the threshold between the erased region and the patterned region is shown (for images of higher magnification see SI). (c) Magnified area of (a) within the erased patterned. (d) SEM image of a periodic structure edge of the laser beam reach in the erased region. The double ended white arrow indicates the polarization of the erasing beam.

An indication that the erasing process can be significantly smooth in the whole erasing area even at the edges, is that the ripple structures seems to be fading at the lateral regions

that the erasing beam were deposited. The erasing process can be attributed to heating effects caused by the accumulated laser pulses in higher accumulated fluence with respect to the one used for the initial writing process[188].

This means that while the erasing fluence value was identical with the fluence used for the initial LIPSS formation the energy deposition on the re-irradiated surface was higher due to the fact that the surface roughness is much higher than the pristine. This significant increment of the active surface results in higher energy deposition than it was in the flat polished sample. More specifically, once the initially flat profile becomes corrugated due to ablation or mass displacement, the geometrical effects will significantly influence interaction of the laser with the solid's surface[49]. As in the vicinity of sharp features of the surface topography, a significant enhancement of the electromagnetic fields can occur, the spatial carrier density distribution may become inhomogeneous and increases locally at a rough or corrugated surface. Along with the increased optical absorption, the sample reflectivity decreases due to the geometrical corrugation and the absorbed energy increases sharply that leads to material melting.

Therefore, the number of pulses in this fluence value was not enough to induced LIPSS formation also on static irradiations as described above in Figure 4.1. The low T_g of the AgPO$_3$ glass seems to be of much significance on the quality of the erasing process assuming that the elastic mechanical properties of these glasses when heated around and above T_g is responsible at these conditions to attain low roughness (polished-like) erased areas. While as reported on previous studies the erasing LIPSS quality on non-visibly transparent metallic glasses[171] performed on fs scanned lines with double pulses (two beams) the erasing quality seems to be much lower to the results presented above.

It becomes apparent that the previously written pattern is readily erased while the glass surface at the erased region (Figure 4.3(b)) rejuvenates to a smooth profile equivalent to that of the pristine glass presented at Figure 4.2(a). Another interesting characteristic of the images of Figure 4.3(b) is the presence of metallic silver particles upon laser processing of the glass in the erased area. Indeed, some silver nano-particles are also noted in the surface of the pristine AgPO3 glass (Figure 4.2(a)), as well as, upon the first laser patterning (Figure 4.2(b,c)). Nevertheless, the processes of erase and re-patterning appear to cause further augmentation of the silver clusters Figure 4.3(b).

4.6   Re-writing LIPSS on the erased areas

Following the successful demonstration of the erasing LIPSS process we attempted to re-structure the exact point that we previously have removed as described in the previous section. Our result confirmed that the erased surface can be re-structured with slightly reduced laser fluence $\varphi=1.39$ J/cm^2, $v=2$ mm/s scanning velocity and $\delta=10\mu m$ line separation. Which are the exact parameters used for the initial LIPSS formation with the only exception of the fluence value. Figure 4.4(a) presents a SEM image that shows a square region where the previously erased pattern has been re-written. Figure 4.4(b) depicts higher magnification of the remained erased square (highlighted with blue dashed square) of Figure 4.4(a). While at Figure 4.4(c) higher magnification of the red dashed square at Figure 4.4(a) is presented along with the laser polarization state denoted with the white double ended arrow.
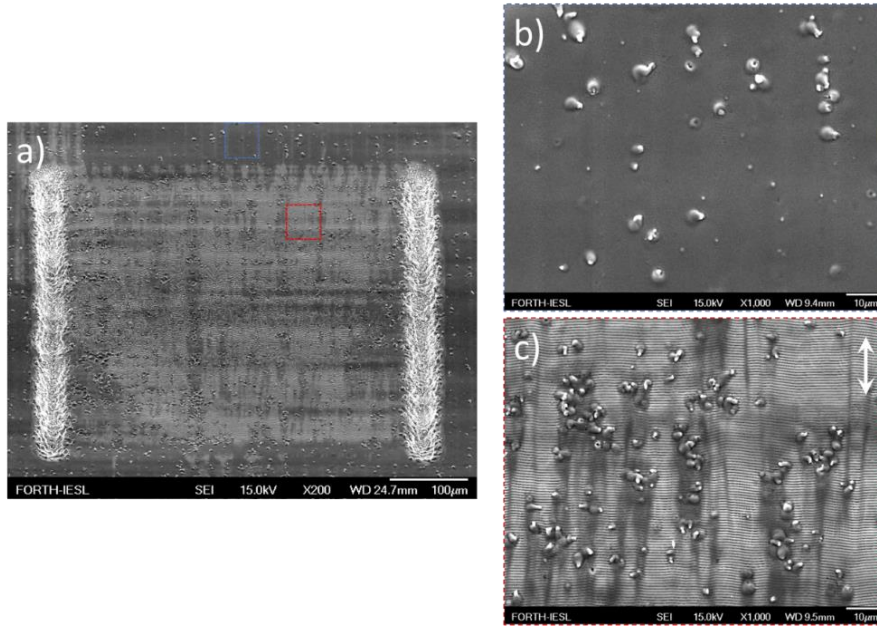
Fig. 4.4: (a)Tilted at 45⁰ SEM image of a periodic structure re-written on the previously erased region. The blue and red dashed highlighted square areas correspond to the higher magnification, top view SEM images of the previously erased (b) and the re-written (c) regions. The double ended white arrow indicates the polarization of the re-writing beam.

Such particle formation explains plausibly the lower laser fluence required for the optimum re-structuring conditions, as the rougher (in this case) glass surface due to the presence of silver particles favors LIPPS formation since they act like light scattering centers. Moreover, the formation of silver nanoparticle clusters observed in the already erased surface at Figure 4.3(b) and Figure 4.4(b) seems to be more pronounced in the re-structured surface of Figure 4.4(c). These can be easily spotted on the top view SEM

images at Figure 4.4(b,c) with the same magnification where the silver nanoparticle formation is much more pronounced and dispersed across the re-written area.

4.7 Optical characterization of AgPO₃ Processed Surfaces

It is of great interest to examine whether the LSFL-LIPSS formation, as well as, the all-laser re-patterning cycle on the surface of AgPO3 glass induces significant glass network structural modifications and most importantly to investigate how the silver clustering is affecting the overall absorbance of the material. Figure 4.5 depicts the normalized optical absorbance spectra of the glasses in question. The presence of silver clusters gives rise to the distinct but relatively broad silver plasmon profile in the 380-500 nm region of the absorbance spectra[189,190].
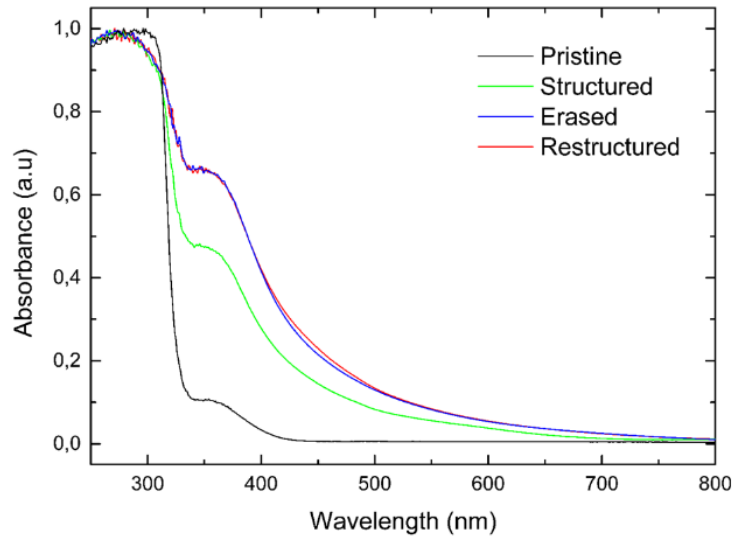
Fig. 4.5: Normalized optical absorbance room temperature of pristine, patterned, erased, and re-patterned AgPO3 glasses.

In accordance to SEM data, the absorption profiles of Figure 4.5 confirm the presence of silver particles within the pristine glass, while the silver plasmon feature gains intensity upon patterning the glass. However, it is highlighted that there is no significant difference between the absorption profile of the erased and the re-patterned glass. The latter finding

suggests that the formation of silver clusters is maximized upon employing the elevated laser power to erase the pattern ($\varphi=1.74 \ J/ \ cm^2$), whereas the lower laser fluence ($\varphi=1.39 \ J/cm^2$) re-pattern process does not seem to cause any further worth noting silver clustering.

The output of all the above experimental results, induced by means of a single-beam femtosecond laser irradiation can pave the way for a complete patterning/erase/re-patterning technique performed by employing a single laser source, i.e. an all-laser process. The ability to erase the so-formed patterns while being able to re-write the structure with the same laser source can be further developed for the surface and the bulk of soft glass. Furthermore it will have enormous potential towards the utilization of phosphate glasses for advanced optical memory[160,167], waveguides[157] and photonic grating sensors[191]. Further work is in progress aiming at the formation of erasable periodic structures within the bulk of soft phosphate glasses of various compositions and types.

5 Realizing polarizing plates via laser processing of sub-micron thin metal films

Abstract – In this chapter a single-step and versatile method to create polarizing plates like wire grid polarizers with high order laser induced periodic surface structures (LIPSS) on metal Ni films. Wire grid polarizers (WGPs) are grating type planar metasurfaces that consist of periodically aligned infinite ridges commonly placed on a uniform transparent substrate. For some electromagnetic frequencies, like the far or mid infrared WGPs is the only available polarizing optic. Herein, we experimentally and theoretically demonstrate a single-step and versatile method for the realization of polarizing plates. We find that highly ordered, femtosecond laser induced, periodic surface structures (LIPSS) formed on nanometre-thick metallic films which are deposited on dielectric substrates demonstrate transmissive WGP operation. Moreover, we show that the LIPSS technique can produce metal-substrate-metal patterns in the form of nanowire arrays with a periodicity that can be tuned by the exciting laser wavelength. Using this method, we pattern polarizing plates on a 100nm Ni film with two different dielectric substrates; the samples exhibit high transmittance and consistent polarization response at IR and Mid-IR. The experiment results for the polarizing efficiency stand in very good agreement with the numerical investigation. Our study indicates that exploiting the LIPSS formation on sub-micron metal films may lead to new types of meta-optics and applications.

Introduction

The ability to control polarization is crucial for most optical systems. WGP, unlike birefringent crystals or Brewster angle polarizers, are subwavelength parallel metal lines attached on a substrate transparent to the desired polarizing spectra. A WGP can reflect polarizing light when the incident electric field is parallel to their orientation and transmit it when its vertical. In principle a polarizer of this type can be effective in any spectral range depending on its spatial characteristics. Wire-like structures were first used as a polarizing element from Heinrich Hertz used a WGP in 1893 to test the properties of radio waves[192]. Limited by the current fabrication technology, the first report as "wire-grid polarizer" for the infrared region was at 1960[193]. Since then many studies were conducted for the realization of modern polarizing optical elements based on conductive wire patterns, with nanofabrication technology[194,195]. Different geometric structures have been

developed and fabricated from the ultraviolet to the Terahertz electromagnetic spectra[196–198]. However, the current methods that lead to the creation of such a polarizer are based on multiple processes and involve toxic chemicals[199].

On the other hand, as we previously presented at chapter 3 & 4 the material removal utilizing laser light can consist a significant tool for the realization of such optical elements.

So far the direct laser ablation on metal films has been a single step method to induce parallel metal arrays on the surface and selectively remove the material[200–202]. However, this approach will always be constrained from the laser beam focusing diffraction limit and laser beam pointing stability[203] which can be a huge problem on ablation quality with tight focused laser light. On the other hand, LIPSS formation can be employed on such spatially confined tin metal films in order to realize self-assembled morphological changes which will appear within the laser beam boundaries. Their periodicity is completely dependent on the laser wavelength and their orientation from the pulse polarization state[126]. Latest studies have shown that it is possible to induce LIPSS formation on sub-micrometer thin metal films[204–207].

In this section investigate LIPSS formation on 100nm Ni films via exclusively ultrashort laser pulses. Moreover, we will seek the exact condition in order to generate of high order LIPSS, selectively induced on the thin metal films. The Ni films were deposited before the irradiation on Fused silica and Sapphire substrate materials and the substrate material type had no effect on the optimum irradiating conditions required. The deposited Ni thin films were irradiated with two laser wavelengths under static irradiation conditions and line scanning. Moreover, rectangular areas were produced with identical conditions on both substrates, which showed polarization response for TE and TM electromagnetic modes. The polarizing plates fabricated are efficient for the IR & Mid-IR spectral regions. Remarkably the Energy Dispersive X-Ray Spectroscopy (EDS) measurements showed significant decrease on Ni concentration among the LIPSS, which is a strong indication that there is complete material removal and only substrate presence. The initial thin film thickness is preserved after the laser processing as showed the analysis on the metal wires height. We believe that this method can potentially revolutionize the way we currently create WGPs.

5.1   Ni thin film deposition

The 100nm Ni thin films were deposited on amorphous silica glass (SiO_2) and crystalline sapphire glass (Al_2O_3) by e-beam evaporation. Various metallic thin films are deposited by e-beam evporation. Substrate is placed in the evaporation chamber which is pumped down to high vacuum (10-7 Torr) by cryo-pumping. Then an electron beam is generated, accelerated and deflected towards metal target (crucible), where the transfer of kinetic energy from the electron heats the metal up.   Evaporation rate and deposited metal thickness is monitored by a quartz crystal sensor.

5.2   Effect of static irradiations on Ni films

Initially the experimental investigation started with a parametric study on the effects of the laser fluence and the pulse number on the surface morphological features. Hence, static irradiations with multiple pulses on the Ni thin films for both substrates were performed. The expression for the energy density (peak fluence) φ_p was calculated as described at chapter 2.2.1.

The number of pulses range was from *NP= 1* up to *NP= 100* receptive to the sample and the fluence range used was *φ_p= 0.17J/cm² - 0.32J/cm²* for the 513nm and *φ_p= 0.28J/cm² - 0.90J/cm²* for the 1026nm wavelength both performed at 1kHz. For *NP < 5* no LSFL structures were formed in the whole range of fluences used. While, from *2 ≤ NP ≤ 5*, surface roughness was significantly increased and resembles a nanostructured grating with a tendency to orientate parallel to the incident polarization similar to the HSFL structures discussed in chapter 1. For the more detailed understanding of the experimental procedure which was described at chapter 2.5 and due to the fact, that in this section the samples are consisted of more than one element with significant physical properties; the experimental procedure is illustrated schematically at Figure 5.1.   In Figure 5.1(a) shows the pulses focused on the thin film in ambient conditions while Figure 5.1(b) presents the morphological effects of the focused laser beam on the thin film material, revealing a pattern of Ni-substrate-Ni within the laser beam limits. Given that the ablation threshold of the dielectric substrates we used is significantly higher than that of Ni there was no differences observed on the morphological features of any of the substrates which were totally unaffected by the laser beam. Hence, the irradiating conditions were identical for both substrate cases, inducing the same periodical

structures. Due to the low value of the laser fluence and the gaussian spatial energy distribution of the beam; LIPSS were formed in a much smaller area than the actual spot size.
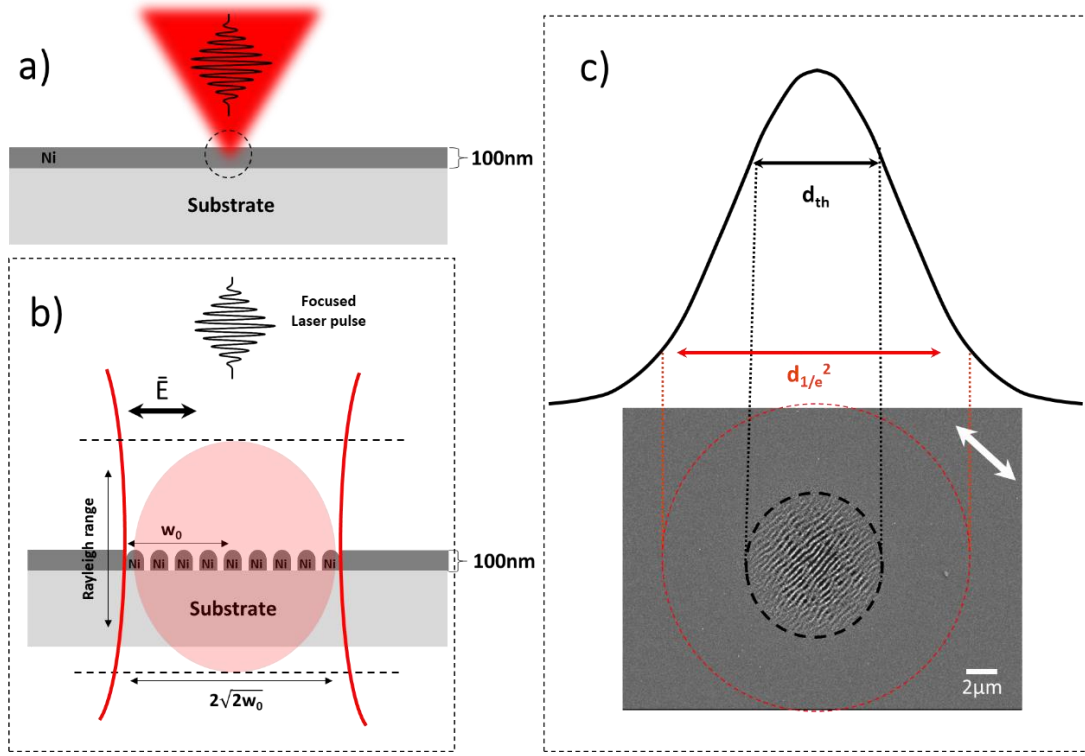

Fig. 5.1: Schematic illustration of LIPSS formation on 100nm thick Ni films on a dielectric substrate, were (a) a focusing laser pulse on the surface of the sample. (b) higher magnification of the black dashed highlighted are at (a). And (c) an SEM image of laser spot with pulse energy E_p=0.38μJ, NP=30, φ=0.17J/cm² at 513nm the black dashed circle surrounding the affected area and the red the real spot size at the 1/e². The double ended black and whited arrows at (b) and (c) denote the laser polarization orientation.

The affected area of a laser spot as an example is presented at Figure 5.1(c) on a top view SEM image highlighted with black dashed circle, produced with E_p = 0.38μJ, NP= 30 and φ= 0.17J/cm² at 513nm. The characteristic threshold diameter of the affected laser induced crater exceeding diameter was measured $d_{th} \approx 7μm$ more than twice smaller than the actual spot size d_{1/e^2} (red dashed circle) for this wavelength. The same effects were observed for the static irradiations of 1026nm with the affected area for *NP= 30* at E_p= 2μJ and φ= 0.25J/cm² was $d_{th} \approx 19μm.$ Further analysis and more systematic on the laser spot affected area will be provided in the following figures after we examine the types of LIPSS we could produce with this method.

Under static irradiations with variable laser fluence and number of pulses showed LSFL formation on the Ni film can occur, selectively removing the metallic layer, giving rise to

parallel metal arrays with periodicity strongly dependent on the laser wavelength and orientation always vertical to the incident polarization state. This metal-substrate-metal interface could be the beginning for the realization of wire-like ripple patterns. In Figure 4.2 top view SEM images are presented as examples, created with λ_{513nm} and λ_{1026nm} at $f=1kHz$ for $\varphi=0,17J/cm^2$ & $0,25J/cm^2$ respectively. The periodicity of the LSFL structures realized with λ_{513nm} was half of the periodicity measured for those created with the λ_{1026nm} wavelength. The 2D-FFT image in Figure 4.2 is the intensity profile of the characteristic frequencies in the 2D Fourier space for the top view images of *NP=30* in the Figure 5.2. The spatial morphological features of the LSFL structures will be more analytically characterized and discussed in the following paragraphs with AFM. Moreover, the static irradiations showed that the linear polarization direction can dictate the orientation of the ripples, for both wavelengths used, totally in agreement with the previously discussed results on chapter 3&4.
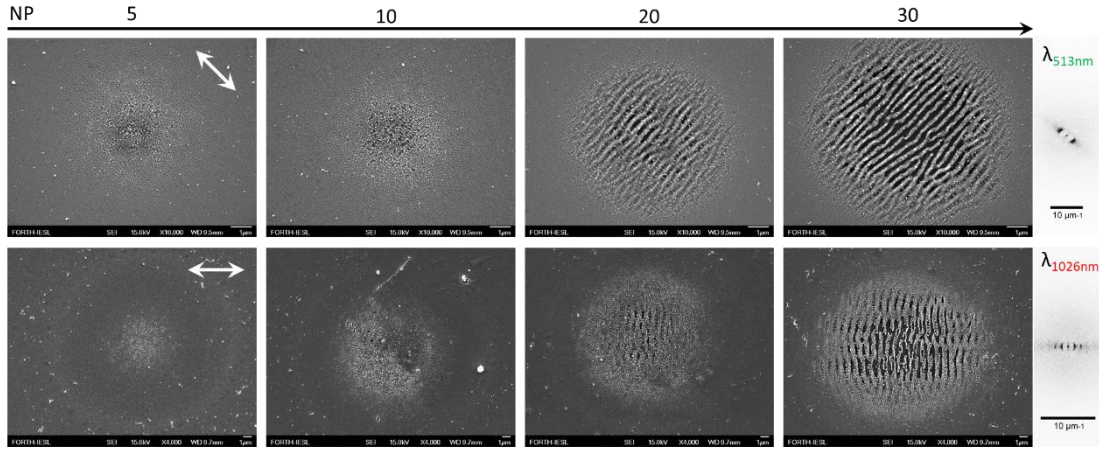
Fig. 5.2: Top view SEM images at different magnifications of NP=(5,10,20,30) for 513nm at 0.17J/cm² top line and 1026nm at 0.25J/cm² bottom line. The 2D-FFT images reveal the intensity profile of the characteristic attained frequencies for NP=30 at both wavelengths. The white double ended arrow indicates the polarization state for both cases.

Notably, the laser induced crater of the affected metal layer is not constant in size for the same laser fluence and variable *NP* (Figure 5.2). Furthermore, SEM analysis on the surface morphological profiles showed that LIPSS formation can occur for a wide range of *NP* at λ_{513nm}. Due to this structural variety and the we have summarized the surface morphological profiles and their dependence on the irradiating conditions (φ, *NP*) on a morphological map (Figure 5.3) which contains the formation of all the different structures in the central region of the laser spot crater, symbolizing the type of surface structures observed for any couple of values of the parameters. The map was created at *f=1kHz* and for λ_{513nm}

In particular it was observed for all the range of fluences used that for *NP*= (2-5), deep subwavelength HSFL structures appear with orientation parallel to the laser polarization. There average periodicity was approximately *148 ±40nm*, while their spatial alignment can be characterized as pseudo-periodical since their spatial arrangement is not regular and uniform. For *5≤ NP ≤10* it the formation of LSFL was observed with irregular arrays formed within the HSFL structures. The mixture of HSFL and LSFL structures was observed for ever higher *10≤ NP ≤30* at the lower φ values where the LSFL formation was faintly notable in the central area of the laser spot crater and decorated with HSFL structures. It is also important to stress that for the highest fluence used at *φ= 0,26J/cm²* and for *5≤ NP ≤10* there no LSFL formation at any *NP* while it was observed this hybrid LSFL and HSFL structures.

In most cases and for *φ>0,17J/cm²* intense ablation was pronounced in the center of the laser spot for a wide range of pulses with LSFL formation taking place only in the periphery of the spots. In the central region only parts of metal remnants remained. The total material removal is even more pronounced for the highest *0.21J/cm² ≤ φ ≤ 0.26J/cm²* used, given that LSFL structures were observed only in one *NP* value for each case and material removal occurred for *NP≥15.* Another important observation is that we observed surface modification for a single pulse only for the φ_{peak} *≥0,24J/cm²* which indicates that the single shot ablation threshold $\varphi_{th}(1)$ of the 100nm Ni film at λ_{513nm} should range *0.19J/cm² <$\varphi_{th}(1)$ ≤ 0.24J/cm²*.

Furthermore, it is of worth to mention that we did not notice any superficial morphological change in the substrate holding the Ni film, which was sapphire in this case. The substrates surface evaluation was performed on the metal ablated regions in which the substrate was exposed and could be further examined with SEM. The substrate type seems to has to effect on the LIPSS formation and that was also verified with structures produced on the top of silica glass with the exact same conditions. The much higher ablation and damage threshold of the dielectric substrate (Al_2O_3 or SiO_2) makes it completely unharmed at the whole range of fluences we used for both irradiation wavelengths.

As previously discussed for metals and semiconductors, the excitation and interference of Surface Plasmon Polaritons (SPP) with the incident laser beam, is the most prominent mechanism accounting for the formation of this wavelength structures commonly called as low spatial frequency LIPSS (LSFL)[9,10,17,40,41]. While there are also reports of high order LIPSS on bulk metal surfaces[141].

Fig. 5.3: Structures observed for any couple of values of the parameters (φ_p, NP) in 100nm Ni films deposited on sapphire at 1kHz and λ_{513nm}. The data refer to irradiation sequences with NP = 1-100 for six fluence values. The SEM images on the right are a typical morphological criterion for the classification of every mark structure case.

The same morphological map was created with λ_{1026nm} at f=1kHz for the evaluation and classification of the LIPSS formation, this time the metal film was irradiated twice lower radiation frequencies and half the photon energy. Subsequently, Figure 5.4 contains the experimental morphological observations and the summarized surface morphological profiles coupled with their classification mark regarding their dependence on the irradiating conditions (φ, NP) exactly as presented at Figure 5.3 earlier. The fluence range we used was *0.13J/cm² <φ_{th} ≤ 0.8J/cm²* and the number of pulses sequence was identical with the previous conditions.
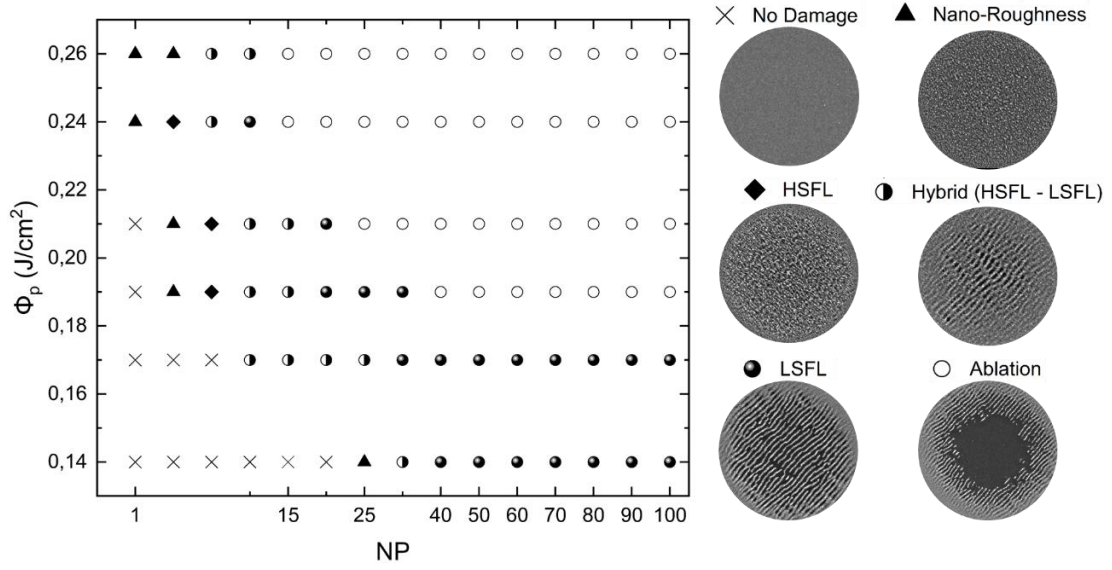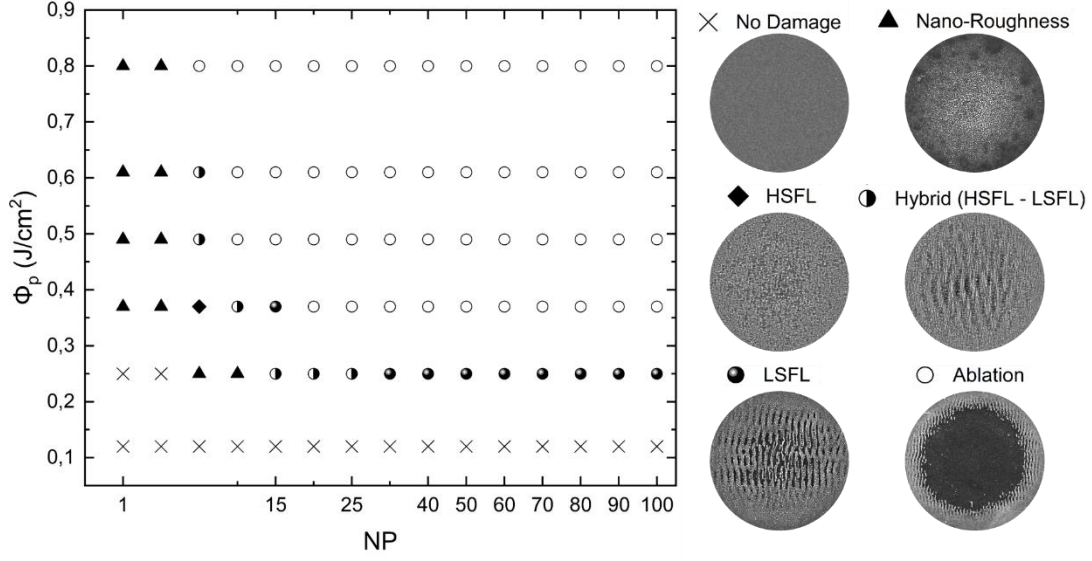
Fig. 5.4: Structures observed for any couple of values of the parameters (φ_p , NP) in 100nm Ni films deposited on sapphire at 1kHz and λ_{1026nm}. The data refer to irradiation sequences with NP = 1-100 for six fluence values. The SEM images on the right are a typical morphological criterion for the classification of every mark structure case.

The results of the spot profiles showed an increased single shot ablation threshold, which was observed much higher at the previous study at λ_{531nm}, indicating that the range of the single shot ablation threshold for the λ_{1026nm} should be around 0.25 J/cm^2 <φ_{th}≤0.38 J/cm^2. LSFL formation is confined in a smaller range of parameters if one compares the Figure 5.4 with Figure 5.3. On the other hand, the this is not a safe conclusion due to the fact that the fluence variation for λ_{1026nm} was performed with higher step than the λ_{513nm}. Making it possible to miss some LSFL observations that could occur in-between the φ values we performed. Nevertheless, the LSFL formation that was observed on the laser spots with λ_{513nm} was well defined (straight lines), with narrow ripple width distribution (182 ± 66nm) and an average period (432± 58nm) for all the sets of parameters of (*NP*,φ), while the LSFL produced with λ_{1026nm} was not regular they exhibited much width discrepancies and the ripples were observed to form oblique lines with two characteristic average periods at (868± 121nm) and (434± 48nm) with a very broad ripple width distribution (433 ± 199nm).

As discussed before on the Figure 5.2, the number of pulses is significantly affecting the later laser affected area. Therefore, the we performed measurements on experimental the spot size areas examined with the SEM images versus the *NP* in variable fluence values and for both wavelengths. Figure 5.5(a) illustrate the average spot size diameter (d) measurements for *NP=1-100* and *φ =0.17J/cm²* and *0.19 J/cm²* fabricated at λ_{513nm} and Figure 5.5(b) shows the same measurements for *φ =0.25J/cm²* and *0.37 J/cm²* for λ_{1026nm} respectively.
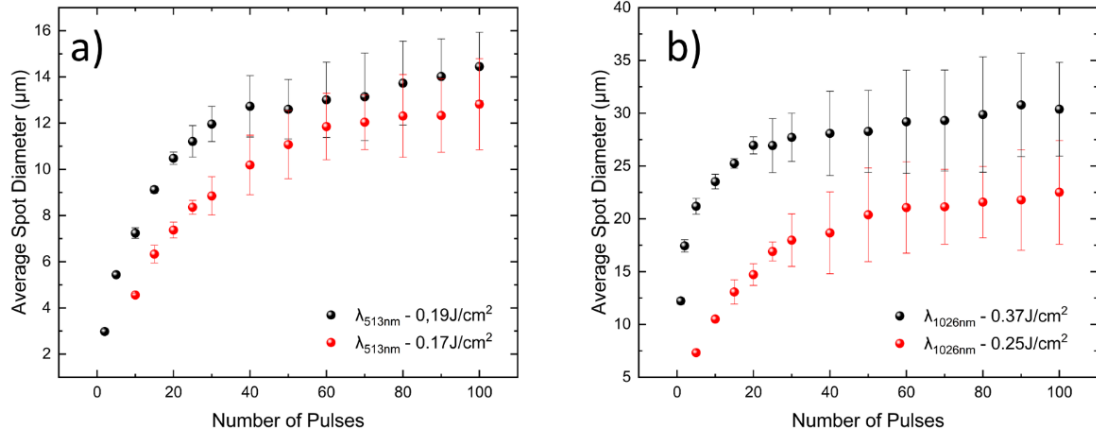
Fig. 5.5: Average spot size dependence on the number of pulses at $\varphi=0,17J/cm^2$ & $0,19J/cm^2$ for λ_{513nm} (a) and λ_{1026nm} (b) at $\varphi=0,25J/cm^2$ & $0,37J/cm^2$ respectively.

There is a strong dependence of the affected area with respect to the number of pulses especially for the lower *NP* values. The spot diameter measurements showed an almost linear increase in the average diameter for *NP= 1-30* for both laser wavelengths. While there is a tendency to saturate for *$50\leq$ NP ≤100.* The reason we decided to perform the spot size measurements in this φ values was that as we noticed from the morphological map at Figure 5.3 these are the exact φ values that can produce LSFL structures in a much wider range of NPs in comparison with all the other. Moreover, the exact dimensions of the laser affected area will be of further use our efforts towards the realization of large areas with LSFL structures on the 100nm Ni films.

5.3 Ablation threshold and ripple formation at λ_{513nm} and λ_{1026nm} wavelengths

Since the number of pulses is crucial to the overall size of the material removal area and considering the Gaussian beam spatial profile, we estimated the NP dependent fluence threshold for the successful LSFL (ripple) formation. Figure. 5.6(a,b) reports the variation of the threshold fluence φ_{th} for ripple structures as a function of the pulse number *NP*, for both λ_{513nm} and λ_{1026nm} respectively. The variation of the area of the spot covered by these specific LIPSS for various values of the number of pulses and the laser pulse energy [208,209]. For the sake of precision, also the fluence values which produced LSFL which did not cover the hole spot were analyzed and displayed in Figure. 5.6. As ripples typically also decorate the very peripheral annular region of the spot, the crater fluence threshold is not

assigned as ripples formation and these threshold fluences were neglected, exactly as the classification on these specific parameters on the morphological maps at Figures (5.3 & 5.4).
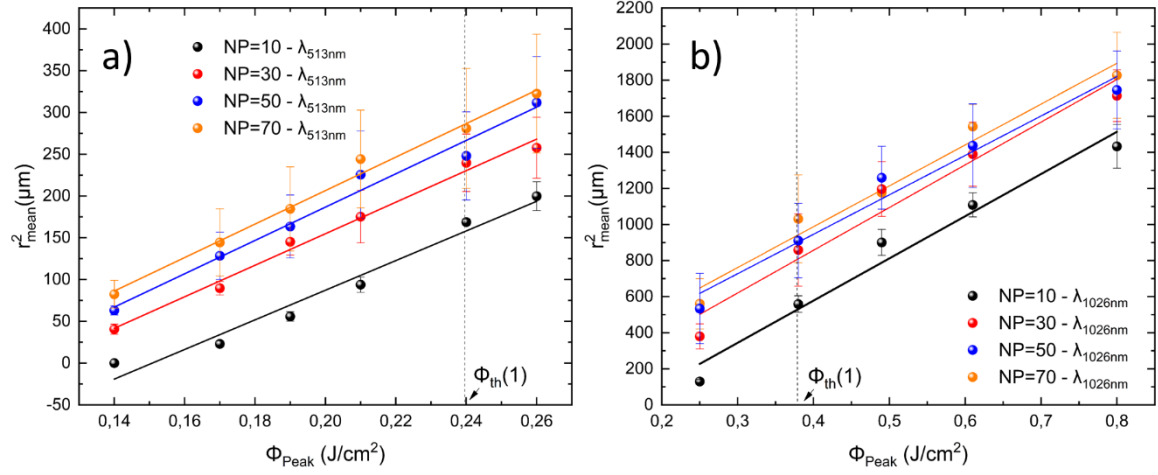
Fig. 5.6: Squared spot diameter (r^2) dependence on fluence for NP=10,30,50,70 for (a) λ_{513nm} and (b) λ_{1026nm}. The colored lines are a linear fit to the individual scattered points.

It is obvious that some of the values in Figure 5.6 are significantly lower than the single-pulse thresholds $\varphi_{th}(1)$ evaluated from Figure 5.4 and Figure 5.5, because the thresholds of modification and ablation depend on the number of applied laser pulses. This incubation effect rests on a non-ablating modification of the sample material by the laser pulses in such a manner that the threshold for damage decreases. Hence, another modification threshold fluence $\varphi_{th}(NP)$ denotes the modification threshold fluence for multiple laser pulses, and ξ is a material-dependent coefficient[210]. Incubation coefficient ξ is related `to the accumulation of energy (i.e. non-complete dissipation of the deposited energy) into plastic stress–strain of the metal. In both cases, we observe a progressive reduction of φ_{th} with multiple NP according to the expected trend described by the dependence [208]:

$$\Phi_{th}(NP) = \Phi_{th}(1)\, NP^{\xi-1}$$

<div align="right">Eq. 40</div>

where ξ is a material dependent incubation factor and $\varphi_{th}(1)$ is the fluence threshold for $NP=1$. For the surface modification we observe that the fluence threshold $\varphi_{th}(1)$ at λ_{513nm} is a factor of ≈ 1.5 times lower than at $\lambda_{1026\ nm}$, confirming the larger effectiveness of ablation and LIPSS formation at shorter wavelengths, which is likely due to diverse energy

coupling efficiency to the thin film Nickel target of laser pulses with different wavelengths and to the consequent different level of excitation reached by the material [211]. For accurate purpose we estimated to separate ξ values the incubation factor for the LSFL formation (ξ_{LSFL}) and the incubation for any other possible surface modification($\xi_{modification}$). Moreover, the threshold fluence values for the ≈170 fs infrared pulses at $\lambda_{1026\,nm}$ are pretty consistent with those observed earlier (namely (0.12 ±0.04) *J/cm²* and (0.20 ±0.04) *J/cm²*) for ablation threshold on bulk Nickel surfaces with NIR 100fs pulses[212,213]. The following table 3 summarizes all the parameters regarding the LSFL threshold fluences for both wavelengths along with the calculated incubation factor *ξ* for Nickel.

Table 3: Peak fluence threshold φth(1), for N=1 pulse and incubation factor ξ for the two wavelengths used in the experiments, namely 513 nm and 1026 nm. The peak fluence threshold for ripples corresponds to that needed to produce exclusively LSFL formation across the hole irradiated laser spot.

λ (nm)	*φth(1) (J/cm²)*	*ξLSFL*	*ξmodification*
513	0.23 ± 0.01	0.89± 0.02	0.83± 0.06
1026	0.32 ± 0.06	0.90± 0.04	0.85± 0.03

Hence, while the fluence threshold for LIPSS formation shows a clear reduction at λ_{513nm} the incubation factor displays a negligible effect of the laser wavelength.

These morphological maps as well as the morphological threshold fluences are a key for advancing on further development of LIPSS on the sub-micron thin Ni film areas due to the prospect of correlating the desired LIPSS class from the map with the effective number of pulses, typical strategy as presented at both previous chapters 3&4. Furthermore the fluence threshold for each surface modification type could provide us the most efficient in energy and speed, (the lower) φ_{peak}, and *NP* values for the successful fabrication of areas with the desired LIPSS.

5.4 Line scanning on Ni thin films

Following spot analysis, line processing experiments were performed in scanning mode, using different scan velocities (*v*) and spot overlap at a constant *φ* value. For line scanning at a constant velocity and stable pulse repetition rate the effective pulse number (N_{eff}) was calculated with the Equation 36. The scanning speeds were calculated to match an overall

effective number of pulses within the *NP* = (30 – 100) and the φ_{peak} values were explicitly selected as from the parametric study at section 5.2. Also, some extreme cases with NP ›› 100 were studied via line scans in order to examine the LSFL formation in much higher number of pulses in the dynamic mode.
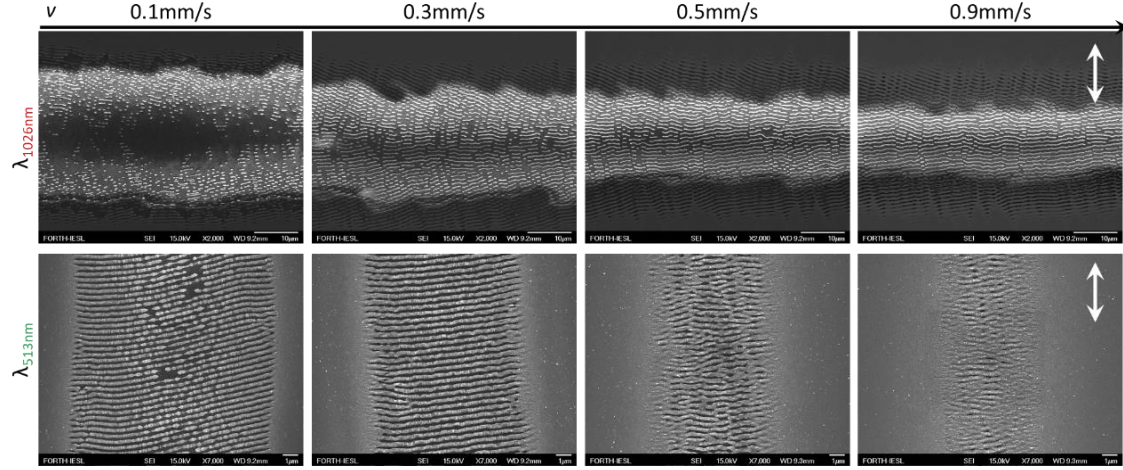

Fig. 5.7: Line scans with variable scanning velocities for λ_{1026nm} (top line) and λ_{513nm} (bottom line) irradiated with φ_{peak} = 0.25 J/cm^2 and φ_{peak} = 0.17 J/cm respectively. The white double ended arrow indicate the polarization state.

Subsequently the top view SEM images of Figure 5.7 exemplifies the characteristic surface morphologies on the Ni films for both λ_{513nm} and λ_{1026nm} respectively. The scanned lines, were all obtained at repetition rate *f=1kHz*, at variable scanning speeds ranging from *v= 0.1 mm/s* to *v= 0.9 mm/s* with a 0.2mm/s increment. As expected, the fluence as well as the effective number of pulses values were φ_{peak} = 0.17 J/cm^2, $Neff_{line}$ ≈ (270, 90, 54, 39, 30) for λ_{513nm} and φ_{peak} = 0.25J/cm^2, $Neff_{line}$ ≈ (490, 163, 98, 70, 55) at λ_{1026nm} respectively. All LSFL ripples as presented at Figure 5.7 were formed vertically to the laser beam polarization. The ripples attained with λ_{1026nm} showed well-defined metallic arrays and formed a characteristic Ni-substrate-Ni interface but with a characteristic non continuity as the ripples showed several gaps with only the substrates presence across the scanned line area. On the contrary the LSFL-ripples formed with λ_{513nm} exhibited a remarkable regularity and continuity with a characteristic example the SEM image of figure 5.7 at *v=0.3mm/s.* The origin of high regular LIPSS was previously discussed on chapter 4 and it seems that this effect is more likely to occur on lower wavelengths for metallic surfaces as theoretical predictions suggest that reducing the laser wavelength can provide the possibility of High regular LIPSS production on principally any metallic surface[141,180,214,215]. Nonetheless, this is the first time these kinds of structures are observed at a sub-micron thin metal film.

As depicted at Figure 5.7 the scanning speed increment lead to a reduced line width. These effects are similar to the spot size variations were presented at Figure 5.5 with the only difference that this time the number of pulses is changing dynamically. Consequently, the higher v leads to lower $Neff_{line}$ values almost in the same manner that the lower NP showed significant decrease in the previously measured laser spot diameter. Furthermore, there were observed LSFL in high Neff values for both wavelengths which was previously unexplored in the parametric study.

Note that all the top line SEM images on Figure 5.7 for the λ_{1026nm} exhibit some inhomogeneous brightness on the grayscale, which is due to charging effects induced from the dielectric substrate during acquiring the SEM picture. This charging effect is a result caused by the dielectric substrate and also the fact that the sample were not sputtered with any additional metal layer before SEM. This was intentional given that it would made impossible the EDS analysis that was performed in the LSFL metal-dielectric-metal interface and will be discussed in the following section. The observed charging effect on the SEM images were not appeared in any SEM image of the λ_{513nm} line scans and one possible explanation would be that the LSFL created with λ_{1026nm} are of almost twice the periodicity from those created with $\lambda_{513nm.}$ The longer the periodicity the more substrate is exposed that can eventually lead to charging effects[216].

The results on the line scanning and the ability to induce partial metal exfoliation leading to the metal-substrate-metal interface can pave the way for a new laser-based tool for polarization control. Moreover, the ability to control the LSFL period with the exiting laser wavelength is of huge importance for the versatility of this method. Given that, we performed the periodicity measurements for the "finest" or, the most regular line scans v with LSFL which we attained at both wavelengths. The periodicity for λ_{1026nm} was 848±66nm for the SEM image with $v=0.9mm/s$ and for λ_{513nm} was measured 422±30nm for the image with $v=0.3mm/s$ of Figure5.7 respectively.

5.5   Realization of a polarizing plate

A multi-scale structuring approach is especially important for comprising optical elements with the desired polarization response at multiple length scales. In this respect, the fabrication of precisely controlled large surfaces consisting of structures with specific spatial frequency, is desirable. Such surface morphology occurs due to the overlap between adjacent lines during the scanning process. Accordingly, the scanning speed

together with the overlap between adjacent spots, are the most important parameters affecting the morphology of the surfaces attained. In our case the distance (δ) between two overlapping laser scanning lines can define along the overlap on the y-scanning-axis while the always assumed constant (v) expresses the pulse to pulse overlap along x-scanning axis.

In order to be able to produce large surfaces that could function as polarizing plates we were in need of a short of up-scaling procedure for the significant reduction of the laser processing time. An example of the importance of the laser processing time would be the following, assuming we are to produce a surface with *f=1kHz* and *v=0.3mms/s* with the λ_{513nm} and with *δ=6μm,* for a surface area of 1cm² we would need approximately ≈15.5 hours for a single surface of 1x1cm. Due to the fact that the *v* and *δ* are very low with respect to the actual area we would need in order to perform a proper characterization. Subsequently the need to reduce the processing speed time was eminent. That is the reason we decided to increase to laser repetition rate but retain the pulse energy exactly the same since the laser pulse energy is given by *Ep=* (*Laser measured average power/f*). With this approach for a *f=10kHz* the much higher pulse repetition enables that we could use *v=3mm/s* and for *f=100kHz* we could use 30mm/s respectively. The only constrain was that with the (*f*) increasement we need to sustain the exact some *Ep* as we have used with *f=1kHz*. Another approach would be to increase the *δ* distance and reduce the processing time, but the significant increasement of *δ* would need to almost zero overlap between two adjacent scanning lines and eventually cause important irregularity and unaffected areas. Consequently, and interplay between the *f* and *δ* as described in the chapter 2.4 was the key for the successful reduction of the laser processing time in order to realize the desired surfaces with the specific morphological features we have presented in the previous paragraphs.

In this context, we performed a series of irradiations for the realization of large surface areas of LSFL on the 100nm-Ni films. Figure 5.8(a–d) demonstrates the top view SEM images of *1 cm² areas, fabricated at f= 60kHz with φ= 0.17 J/cm², v= 30 mm/s, δ=6μm* on fused silica and sapphire substrates with λ_{513nm}. The SEM images on Figure 5.8(a,b) correspond to 100nm Ni with a SiO_2 substrate while Figure 5.8(c,d) for Al_2O_3 substate respectively. It can be observed that the structures attained are of high order and homogeneity with high preferential shape and orientation. The LSFL formation was again perpendicular to the incident laser beam linear polarization state, and the structures showed a smooth corrugation of Ni-substrate-Ni interface. All the fabricated surfaces showed high regularity with only a few imperfections (small discontinuity points) which

can be spotted in Figure 5.8(a,c). These imperfections could be attributed to our custom made set up and which is designed for research purposes and not for the realization of large high-precision laser treated surfaces (due to vibrations). But also, it could be the result of weak local adhesion of the deposited Ni films during the e-beam evaporation due to the presence of dust of other impurities during the metal film deposition. The geometrical characteristics of these metal ripples of the produced surfaces are 432± 58nm in periodicity, in a complete agreement with the period measurements we obtained for the line scans at Figure 5.7 (namely 422±30nm), showing an average ripple width of 182± 66nm. The actual photograph of the laser structured area of the Figure 5.8(c,d) is presented at Figure 5.8(e) showing the processed area of the 100nm-Ni thin film on a round sapphire substrate of 1mm thickness and 26mm diameter on a low-illuminated background, comprising the polarizing plate.

Fig. 5.8: Top view SEM images of LIPSS on Ni films on SiO$_2$ (a),(b) and Al$_2$O$_3$ (c),(d) fabricated with at f= 60kHz with φ= 0.17 J/cm^2, v= 30 mm/s, δ=6μm at λ$_{513nm}$. Physical photograph of (a) The actual physical image of the 1 cm^2 on Al$_2$O$_3$ substrate is presented on (e) as an example. The double ended white arrow denotes the beams polarization state.

The same surfaces were realized on both sapphire and silica substrates this time with λ$_{1026nm}$ in order to prove that the control of the spatial features in large surface areas is possible with the change of the λ. In Figure 5.9(a-d) top view SEM images of *0.5 cm^2* areas, at different magnifications fabricated at *f= 60kHz* with *φ$_{peak}$= 0.25 J/cm^2, v= 30 mm/s, δ=6μm* on fused silica and sapphire substrates with *λ$_{1026nm}$*. The SEM images on Figure 5.9(a,b) correspond to 100nm Ni with a SiO$_2$ substrate while Figure 5.9(c,d) for Al$_2$O$_3$ substate respectively. It can be observed that the structures attained are of high order and homogeneity with high preferential shape and orientation. In addition, with the surfaces

produced with λ_{513nm} those created with λ_{1026nm} are not so regular with the LSFL structures to exhibit a lot of discontinuities and ununiform corrugation. All the fabricated surfaces showed a relative low regularity with many voids (presence of the substrate only) which can be spotted more clearly in Figure 5.9(a,c) which are the higher magnification SEM images.

The reduced LIPSS regularity of the surfaces in Figure 5.9 can be attributed to the fact that we used identical parameters except the laser fluence for their fabrication as we used for the those at Figure 5.8 which were fabricated with λ_{513nm}. The use of the exact same δ and v caused and increased number of pulses to the surfaces produced with the IR pulses because of the almost twice bigger spot size of the λ_{1026nm} with respect to λ_{513nm} as previously explored and presented at Figure 5.5. Nevertheless, the aim of the fabrication of this second polarizing plate was only an attempt to prove the wavelength dependence on the spatial features of the LSFL and the validity of this method for the direct realization of polarization responsive plates upon laser processing of sub-micrometer metal films on a substrate. Hence, the estimated periodicity of the Ni ripples on the surfaces of Figure 5.9 was 892±91 and in very good agreement with the line scans previously discussed at Figure 5.7 and twice higher that the polarizing plate produced with λ_{513nm} (Figure 5.8) and an average width of 221±85.

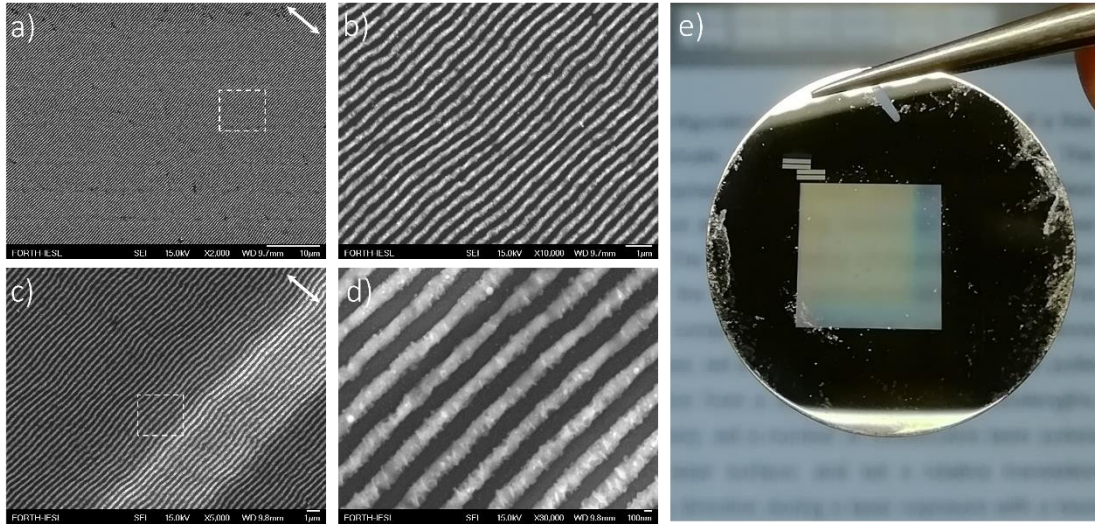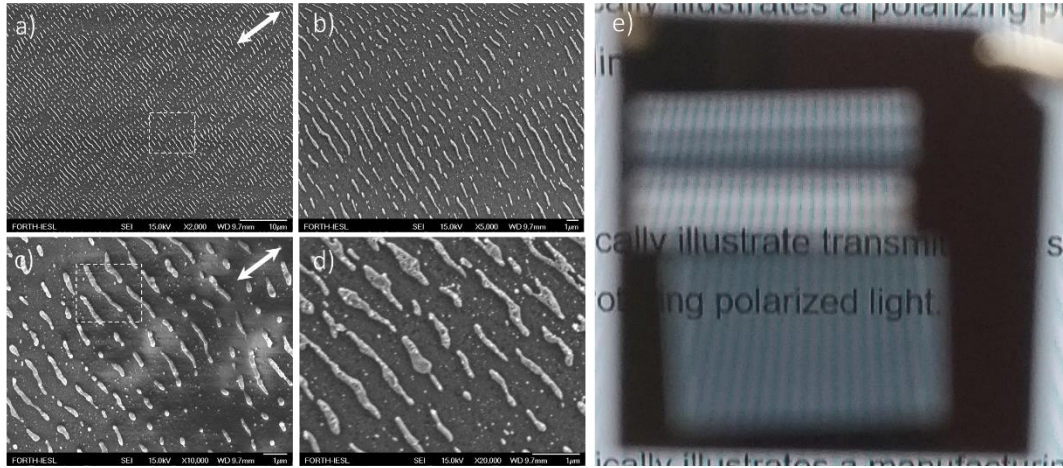*Fig. 5.9 Top view SEM images of LIPSS on Ni films on SiO$_2$ (a),(b) and Al$_2$O$_3$ (c),(d) fabricated with at f= 60kHz with φ= 0.25 J/cm^2, v= 30 mm/s, δ=6μm at λ_{1026nm}. Physical photograph of (a) The actual physical image of the 1 cm^2 on SiO$_2$ substrate is presented on (e) as an example. The double ended white arrow denotes the beams polarization state.*

Because of the low regularity obtained in the surfaces produced with the infrared fs pulses we decided to perform a complete topographical assessment on the surface only produced with λ_{513nm}. Given that the analysis on the LIPSS spatial characteristic such as period, width and height are crucial for the realization of WGP the need to evaluate the obtained structural dimensions of the LSFL are of huge importance. Therefore, all the

spatial characteristics (except the ripple depth which will be discussed in the following paragraph) of the surfaces produced with both wavelengths are summarized in the following table. The estimation of the ripples period and width was performed on SEM images for the period (p) according to chapter paragraph 2.6.1 and for the width (w) we calculated the average and the standard deviation of ten manual measurements on random areas on top view SEM images. Furthermore, the fill factor (F) =(w/p) of the surfaces is calculated for every case since it is an important parameter for the polarizing plates efficiency as we will discuss below.

Table 4: Summarized the spatial characteristics of the LSFL-ripples produced with λ_{513nm} and λ_{1026nm} of the polarizing plates

λ (nm)	p (nm)	w (nm)	F
513	432± 58	182± 66	~0.42
1026	892±91	221± 85	~0.25

5.6 Morphological and Chemical characterization of the LSFL structures

Following the estimation of the spatial characteristics (periodicity and width) of the fabricated LSFL on the Ni films it is crucial to evaluate the depth of the laser induced corrugation on the Ni film and whether it is affected from the initial thickness of the deposited metal layer (100nm). Thus, the attained structures on the line-scanned areas were characterized through EDS and AFM with aim to investigate whether the initial thin film thickness (100nm) is preserved after the laser processing procedure. The AFM analysis on the laser processed areas Figure 5.10(a,b) showed that the average ripple height was 123nm ± 21nm. These slight increase on the thin film height is due to Ni nanoparticle accumulation (observed on AFM and SEM high magnification images) on the top of the ripple structures as the surfaces didn't passed through any cleaning procedure after irradiation as a precaution due to our concern that they might not survive an ultrasonic cleaning bath. It is important to note at this point that after characterization we tested this case and Ni structured films on both substrates seemed to endure without any visible deformation (examined from the optical microscope) a 10-minute ultrasonic bath on 40^0 heated ethanol.
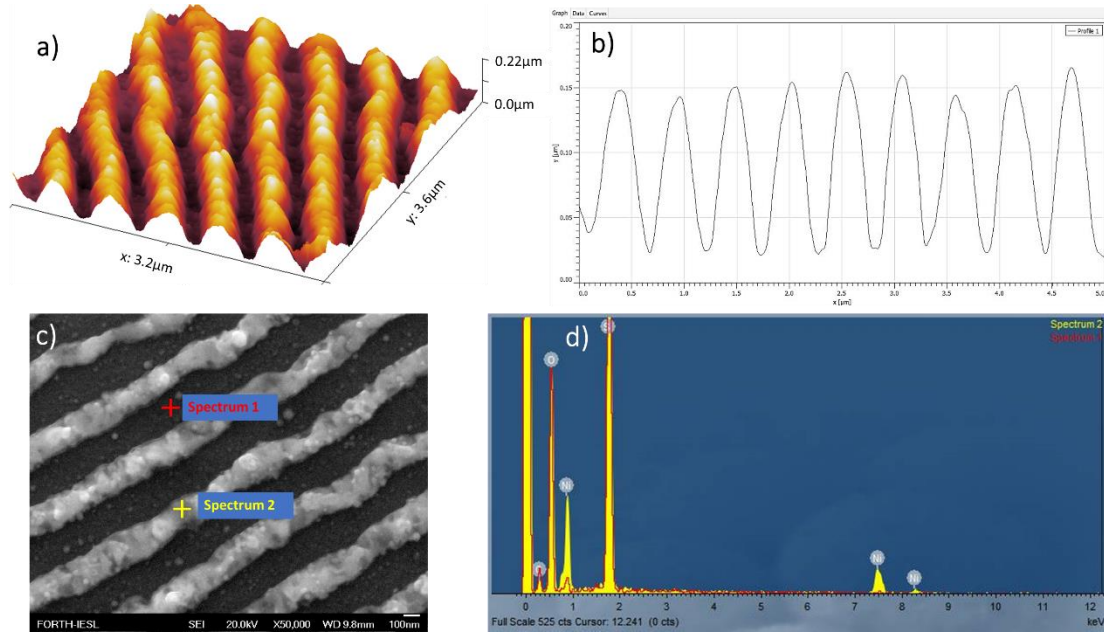
Fig. 5.10 AFM and EDS analysis for line scans produced with 513nm. Here, (a) the AFM morphological 3D image, (b) the extracted height from cross-section line acquired from (a). EDS analysis with (c) SEM image depicting the examined areas, (d) the corresponding spectrums for red and yellow marked areas of (c).

Along with the AFM Figure 5.10(c,d) depicts the EDS results for the red and yellow cross-marked areas on Figure 5.10(c). The EDS spectrum for these marked areas are presented on Figure 5.10(d) and indicate that the Ni concentration on the ripple (red spectrum) is about ≈9 times higher than the void between two ripples (yellow spectrum). This is a strong indication that the only remnants are nanoparticles which can be afterwards removed through the cleaning procedure. The complete removal of the Ni film in-between the ripple structures as well as the confirmation that the only metal remnants are some ablated nanoparticles are essential for the further developments of high-quality laser induced polarizing plates.

Conclusively, the results of the AFM as well as the EDS analysis indicate that we created well-defined corrugation of metal lines with a complete removal of the metallic layer from one line to another. While the almost ineligible Ni concentration presented in the exposed substrate segments (in-between the ripples), verifies our hypothesis that these surfaces can potentially act exactly like a WGP plate. In this framework we proceed with optical characterization of the fabricated surfaces in transmission mode.

5.7 Polarization response in the Mid-Infrared of the plate

5. Realizing polarizing plates via laser processing of sub-micron thin metal films

In order to evaluate the polarization response of the fabricated surfaces we had to measure the percentage of linearly polarized light that is passing the plate when the light polarization is parallel (TE) and vertical (TM) to the ripple orientation. Transmission measurements with linearly polarized light were performed for surfaces processed with λ_{513nm} on both silica and sapphire substrates as well as the surfaces produced with λ_{1026nm} for the same substrates. It is important to note that all the measurements of the polarizing plated were performed with the help of Dr. George Kenanakis with a Fourier-transform infrared spectroscopy (FT-IR) system, placed in the laboratory of the Photonic-, Phononic- and Meta-materials (PPM) Group at FORTH. The fused silica and the sapphire substrates were uncoated and without any anti-reflection coating treatment while all transmittance measurements were performed at normal incidence of the incident beam with respect to the sample surface ($\approx 89.9^0$). The background of all the transmittance measurements for both samples was the air.
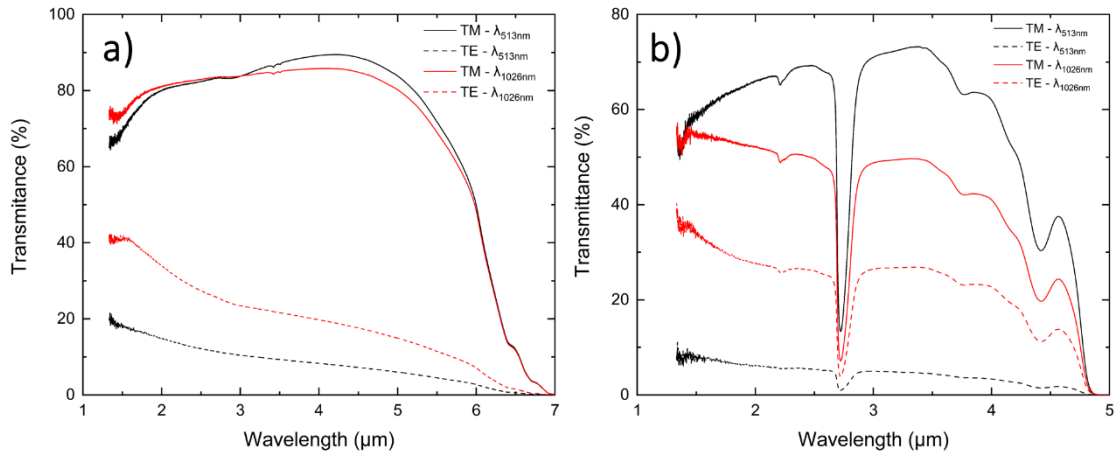
Fig. 5.11: The transmission spectrums for (a) Sapphire and (b) Fused silica substrates, the red and black lines correspond to λ_{1026nm} and λ_{513nm} respectively. The straight red and black lines are the transmittance measurements of the TM polarization (vertical to the ripples) and the dashed lines correspond to the transmittance measurements of the TE polarization (parallel to the ripples).

All the surfaces of Figure 5.8 and Figure 5.9 were characterized regarding their transmission with polarized light for TE and TM polarization modes at the IR and the Mid-IR spectrum (1-7μm). The TE polarization was parallel to the metal ripples and the TM vertical. The transmittance results for both surfaces are presented at Figure 5.11 were the straight red and black lines correspond to the fabrication wavelengths with red for λ_{1026nm} and black for λ_{513nm}, while the straight lines are always the TM and the dashed lines the TE polarization modes for both the sapphire and fused silica substrates. From the spectrum graph of Figure 5.11(a), for the TM mode the transmittance is almost as a plateau, similar for both irradiation wavelengths and showing a maximum of ~90% value for the λ_{1026nm}

at 4.5μm. Furthermore, it is observed significant and gradual decrease in transmittance when the incident light is TE-polarized for a wide range of 1.3μm-7μm, while the transmission in approximating a zero value at 7μm given that the Sapphire is non transparent for λ>7μm and most of the far-infrared. For the fused silica substrate (Figure 5.11(b)) the same trend is observed for both wavelengths while the TE transmittance is lower with respect to the sapphire (Figure 5.11(a)). The transmittance values showed a maximum value at 76% in the 3.5μm for λ_{513nm}, while the overall transmittance spectra in less broadband than the one examined with the sapphire substrate due to high absorption of the silica substrate from the 5μm and higher. Moreover, the characteristic absorption valley of the UV-graded silica substrate we used is observed at ~2.7μm, given that the measurements were performed with respect to the air background transmittance.

The overall transmittance reduction for the TE mode in both cases presented at Figure 5.11 is attributed due to the electric fields alignment parallel to the metal orientation, which prompts movement of electrons along the length of the ripples[217]. Given that the electrons are free to move in this direction, the polarizer behaves like a typical metal surface when reflecting light and most of the wave is reflected backwards (except of a small amount of energy which is lost due to Joule heating of the metal ripple)[192].
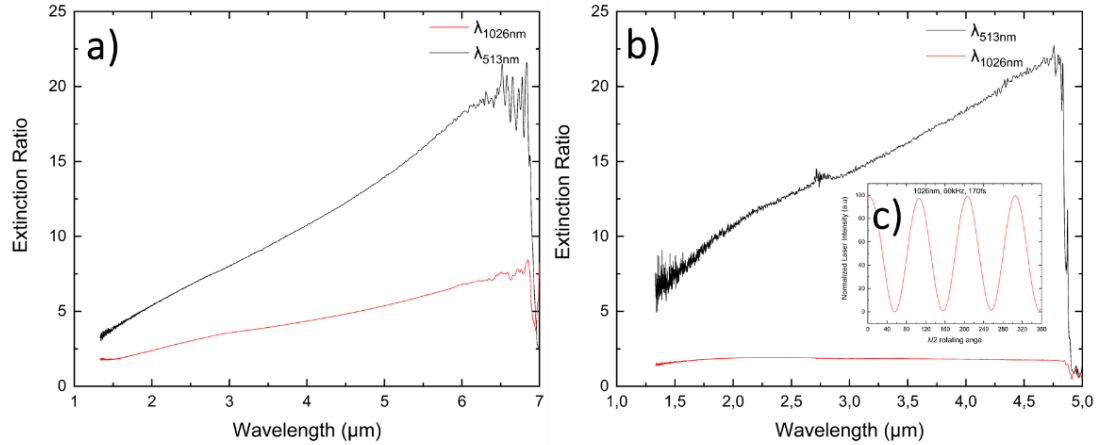
Fig. 5.12: Extinction ratio of the polarizing plates for (a) sapphire and (b) fused silica, the red and black lines correspond to λ_{1026nm} and λ_{513nm} respectively. (c) consistency of the polarizing plate, measured at 1026nm and 60kHz by rotated with a zero-order λ/2 waveplate.

The extinction ratio of the polarizer was acquired from the transmittance spectrums of Figure 5.12(a) as the ratio of the transmittance of TM/TE polarization, presented at Figure 5.12(b) with the red and black straight lines corresponding to the λ_{1026nm} and λ_{513nm} fabrication wavelengths respectively. The extinction ration measurements showed

significant differences for the polarizing plates attained with the fundamental and the second harmonic of the laser. Regardless the substrate type, the polarizing plates fabricated with λ_{513nm} was dominant and with much higher contrast with respect to those obtained with λ_{1026nm} as the LSFL structures were much more regular and with very few discontinuities and the ratio of ripple (w) and the ripples (p) is almost twice higher as we saw in the previous section.

The highest extinction ration values were 25:1 at 4.0 – 5.0µm for Fused Silica and 23:1 between 6.5 – 7.0µm for Sapphire. Furthermore, the consistency of the polarizing plate fabricated with λ_{513nm} on a fused silica substrate. The reliability of the plate was measured and depicted at Figure 5.12(c) graph were the polarization of our femtosecond laser beam (and not on the FT-IR) at 1026nm and 60kHz was rotated with a zero-order λ/2 waveplate for a full circle at 360°.

For the optimization of our method towards higher extinction ratio yields which would make even more valuable our direct realization of the polarizing plates, the effective medium theory (EMT) has often been used in order to estimate the effective permittivity of a dielectric periodic structure[218–221]. In our case and for the regular array of ripples on a dielectric substrate the refractive index is termed as n_s. The refractive index of the Ni ripple or wire and the filled material are n_{Ni} and n_f. The grating period is p and the shape of the wire can be described by a value of (w) and height (h). The filled factor (F) (defined as ratio w/p).

So, for an unpolarized wave with λ propagating upon the grating medium with refractive index n_{ni} at normal incident. The EMT can be considered[222], with the only boundary that grating period is much shorter than the incident wavelength (which is met in our case both cases). Therefore, our fabricated surfaces can be regarded as an equivalent anisotropic film, and the complex effective refractive indexes of our polarizing plates for both TE polarization and TM polarization can be estimated with the EMT[223]:

$$n_{TE} = \sqrt{[n_{Ni}^2 F + (1 - F)n_F^2]} \qquad \text{Eq. 41}$$

$$n_{TM} = n_{Ni}n_F \frac{1}{\sqrt{[n_F^2 F + (1 - F)n_{Ni}^2]}} \qquad \text{Eq. 42}$$

With equation 41 and 42 we performed theoretical calculations for the Ni polarization gratings we fabricated, assuming that the refractive index of the Ni is not changed thought the laser irradiation process (due to oxidation). The nickel's complex refractive index was taken from ref[224]. Figure 5.13 shows the effective permittivity of the Nickel wire-grid grating as a function of F ranged from 0.1 to 0.9 with $n_F=1$ and $n_{Ni}=3.47+9.09i$ which is the refractive index of Nickel at $\lambda= 1.937\mu m$. As seen, the refractive indices of effective medium for both TE polarization and TM polarization increase with the increase of filled factor. The effective refractive index for TM polarization is larger than that for TE polarization. Figure 5.13(b) shows that the extinction coefficient for TE polarization increases with the increase of fill factor.
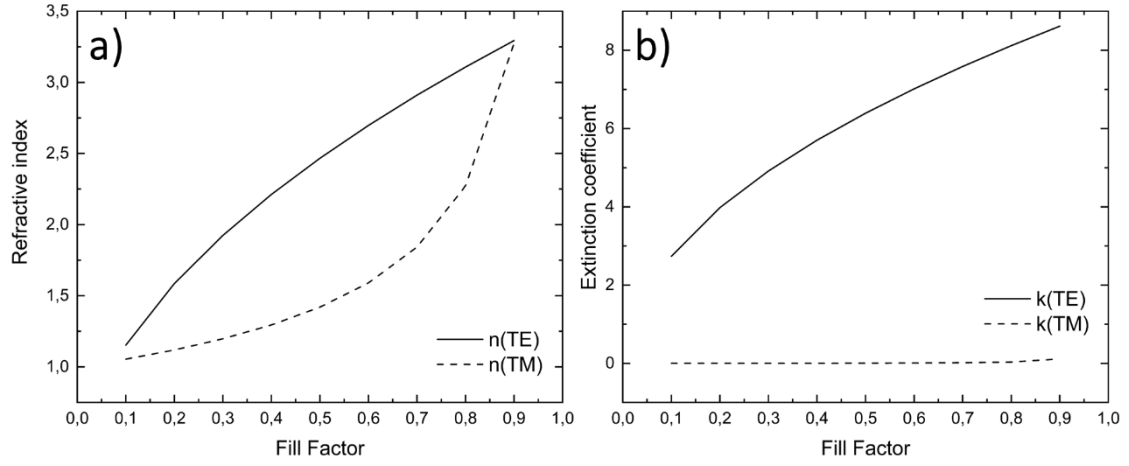
Fig. 5.13: The calculated effective refractive index (n) as a function of fill factor (a) and the effective extinction coefficient (k)as a function of fill factor (b)

From Figure 5.13(b), we can see that the extinction coefficient for TM polarization is near zero, and it is much smaller than that for TE polarization. We can also observe that the effective refractive index and extinction coefficient of the ripples with different fill factors for TE polarization show similar characteristics with the bulk Nickel material that has small refractive index and large extinction coefficient in the infrared region. In contrast, the effective refractive index and extinction coefficient of the wire-grid grating with different filled factors for TM polarization exhibit characteristics of bulk dielectric material with large refractive index and extremely small extinction coefficient.

With the use of EMT we can also demonstrate how to design our polarizing plates with higher polarization extinction ratio than those we can yield taking into account the substrate properties. We can now calculate the most effective F for a fused silica substrate as an example. Given that, the parameters are fixed and the ambient refractive index

n_{air}=1.0, the n_s=1.439 (for fused silica), p=0.5μm, λ=1.937μm, the refractive index of the gap between two successive ripples n_F=1.0, and the angle of incidence θ=0⁰, we can determine the fill factor of the wire-grid grating according to the refractive index of the substrate. And in advance, the requirements of the LSFL height (h) for TM polarization can be obtained by enhancing the TM-polarization transmission. Furthermore, the requirements of the h for TE polarization can be obtained this time by enhancing the TE-polarization reflection resulting to higher transmission and reflection for the TM and TE modes respectively. Therefore, the ideal h can be determined as the h value that the polarizing plate can presented enhanced TM-polarization transmission and the TE-polarization reflection.

Accordingly for the fused silica substrate, we can define the optimum F to make the wire-grid grating as an effective antireflective film with high transmittance according to the film theory[225]. Hence, the refractive index of the effective film that is the most efficient to act as an antireflection film is:

$$n_{eff(TM)} = \sqrt{n_{air}n_s}$$

Subsequently with the above parameters the $n_{eff(TM)}$ = ~1.2. Furthermore, the F of the for n_{TM} from Figure 5.13(a) equals to F~0.3.

This means that our polarizing plate could reach the highest extinction rates for a F~0.3. The only constriction of our method is that currently there is not a possible way to control he w of the LSFL and on the same time to obtain high regular LIPSS.

Consequently, for TM polarization, the transmittance will reach a maximum value and the reflectance for TM polarization will be nearly zero with the optimized filled factor if the height of wire-grid grating meets the condition of

$$h = m\frac{1}{4}\frac{1}{n_{eff}}\lambda$$

where m= (1,2…) It has to be mentioned that the k for TM polarization has been neglected in our design process because of its relatively small contribution from Figure 5.13(b). And the h of the ripples can be adjusted to the initial thin film deposition.

The extinction ratio results we obtained are significant but not tremendous, due to the fact that the h was not the optimum, given that we needed to prove the validity of this

method. However, for future prospects polarizing plates with variable h can be produced with both laser wavelengths (we have strong indications for this) were of high regularity and exhibiting well divined spatial characteristics with dimensions that can respond to the calculated spectral region that we need to examine.

Conclusively, we have presented a systematic method for the direct realization of a polarizing plate, based on laser induced periodic surface structures on thin metal films. The fabricated surfaces were characterized optically and morphologically and exhibited significant polarization response on the IR and The Mid-IR electromagnetic spectrum. As a future prospect, the effective spectrum of the polarizer can be controlled with the thin film ripple period which can be controlled precisely with the laser wavelength or even the angle of incidence of the laser beam[226]. Furthermore, due to the simplicity of this technique and the versatility it can potentially be applied on alternative thin film materials with different thickness for optimization. Due to the simplicity of the method we estimated that with the current laser technology we can create a 2.5cm² polarizing plate in ~3seconds. We believe that this method can be applied on almost all thin metal surfaces regardless the substrate characteristics. Eventually, this approach can with further development revolutionize the current way we produce wire grid polarizing plates without the need of chemicals and time-consuming multi-step processes.

Conclusions

This thesis reports on systematic experimental investigations regarding the direct femtosecond laser structuring of bulk and sub-micrometer layered surfaces. Within the framework of the thesis, the focus on particular surface structures have been considered along with their development from single craters covered with self-organized laser-induced periodic surface structures to large area surface patterns. The realization of these surfaces was achieved via laser scanning with spatially variant and linear polarization modes. Furthermore, the influence of the experimental parameters, like laser wavelength, laser fluence and number of pulses have been also addressed with particular emphasis on the LIPSS formation on sub-micrometer thin metal films. All the experiments were designed basically with the following aims: i) to acquire further indications on the physical processes involved in the formation of the surface structures with respect to the laser exiting polarization state; ii) Implement LIPSS formation for the possibility to realize reversable control on the morphological characteristics of the laser-generated structures; iii) Provide some preliminary results towards scientific applications or methods that could potentially have possible technological and industrial interest.

In Chapter 3 the fabrication of LIPSS using cylindrical vector beams with vectorial polarization states was addressed. The observation of the orientation of the LIPSS following the complex state of polarization states (radial and azimuthal) on Nickel surfaces was illustrated in detail as it consists a direct method to produce complex and multi-directional LIPSS patterns. Along with the surface characterization, the Nickel response was experimentally and theoretically investigated for the radial and linear polarization effect on the surface plasmon polariton properties and eventually on the ripple formation and their spatial features. Moreover, we demonstrated a new strategy to realize angle-free structural coloration (iridescence) introducing a single step approach for the fabrication of unique surface structures that act as refractive gratings in all possible observing angles with multi-ordered surface patterns.

Based on our knowledge on the mechanism for LIPSS formation, we have demonstrated the possibility of highly-regular, erasable and re-writable periodic surface patterns on silver metaphosphate glass ($AgPO_3$). The experimental investigation was performed at 1026nm laser wavelength, 170fs pulse duration and 1kHz repetition rate. We showed that laser LIPSS can be readily erased and re-written upon further exposure to femtosecond

laser irradiation under controlled conditions. This all-laser inscription and deletion protocol allows the reversible patterning of the phosphate glass surface by employing a single laser beam. While the UV-VIS spectroscopy revealed that the formation of the periodic patterns and the erasing process do not cause any phosphate network modifications or structural damage on the glass, and thus, proving that the demonstrated reversible LIPSS process in sub-ablation conditions. This could practically enable infinite cycles of the write/erase/re-write process on the same area of the glassy material, posing the LIPSS formation on $AgPO_3$ glass as an important method for laser induced waveguides and optical responsive memory components of advanced photonic applications.

Finally, the possibility of direct laser structuring of Ni thin films deposited on a dielectric substrate, to obtain wire-grid polarized elements, was demonstrated. We have particularly shown the realization of a functional WGP plate. Exploiting the generation of high order LIPSS, selectively induced on 100nm Ni thin metal films. It is also shown that the substrate material had no effect on the optimum irradiating conditions required. The deposited Ni thin films were irradiated with two laser wavelengths of 1026nm and 513nm on static irradiation conditions and line scanning mode. Detailed experimental analysis was presented regarding the fluence thresholds for LSFL and crater formation on the layer material. Moreover, rectangular areas were produced with identical conditions on both substrates, which showed polarization response for TE and TM electromagnetic modes. The polarizing plates functioned as polarizing plates for the IR and Mid-IR spectral regions. The polarizer was characterized both experimentally and theoretically from 1μm to 7μm spectral range for TE and TM polarizing modes showing extinction ratio up to of 23:1 and high consistency. Remarkably the EDS measurements showed significant decrease on Ni concentration among the metal ripples, which is a strong indication that there is complete material removal. Following the laser processing, the initial thin film thickness is preserved, as showed by the analysis of the metal wires height. As a future prospect it could be possible to control the effective polarization response of the plate with the laser wavelength or the laser fabrication angle of incidence, as this is the only way to control the spatial characteristics of the LIPSS on the metallic film. We believe that this method can potentially revolutionize the way we currently create wire grid polarizers and with further development it could consist an important method for the direct, maskless and chemical free technique that produces wire grid polarizers from the visible to the far infrared electromagnetic spectra.

Bibliography

1.   Birnbaum, M. Semiconductor Surface Damage Produced by Ruby Lasers. *J. Appl. Phys.* **36**, 3688–3689 (1965).

2.   Bonse, J., Hohm, S., Kirner, S. V., Rosenfeld, A. & Kruger, J. Laser-Induced Periodic Surface Structures— A Scientific Evergreen. *IEEE J. Sel. Top. Quantum Electron.* **23**, 9000615 (2017).

3.   Ahmmed, K., Grambow, C. & Kietzig, A.-M. Fabrication of Micro/Nano Structures on Metals by Femtosecond Laser Micromachining. *Micromachines* **5**, 1219–1253 (2014).

4.   Borowiec, A. & Haugen, H. K. Subwavelength ripple formation on the surfaces of compound semiconductors irradiated with femtosecond laser pulses. *Appl. Phys. Lett.* **82**, 4462–4464 (2003).

5.   Barberoglou, M. *et al.* Controlling ripples' periodicity using temporally delayed femtosecond laser double pulses. *Opt. Express* **21**, 18501 (2013).

6.   Gräf, S. & Müller, F. A. Polarisation-dependent generation of fs-laser induced periodic surface structures. *Appl. Surf. Sci.* **331**, 150–155 (2015).

7.   Han, Y., Zhao, X. & Qu, S. Polarization dependent ripples induced by femtosecond laser on dense flint (ZF_6) glass. *Opt. Express* **19**, 19150 (2011).

8.   Tsibidis, G. D., Skoulas, E. & Stratakis, E. Ripple formation on nickel irradiated with radially polarized femtosecond beams. *Opt. Lett.* **40**, 5172 (2015).

9.   Sipe, J. E., Young, J. F., Preston, J. S. & van Driel, H. M. Laser-induced periodic surface structure. I. Theory. *Phys. Rev. B* **27**, 1141–1154 (1983).

10.   Bonse, J., Rosenfeld, A. & Krüger, J. On the role of surface plasmon polaritons in the formation of laser-induced periodic surface structures upon irradiation of silicon by femtosecond-laser pulses. *J. Appl. Phys.* **106**, 104910 (2009).

11.   Hwang, T. Y. & Guo, C. Angular effects of nanostructure-covered femtosecond laser induced periodic surface structures on metals. *J. Appl. Phys.* **108**, 073523 (2010).

12.   Bonse, J., Munz, M. & Sturm, H. Structure formation on the surface of indium phosphide irradiated by femtosecond laser pulses. *J. Appl. Phys.* **97**, 013538 (2005).

13.   Bonse, J., Krüger, J., Höhm, S. & Rosenfeld, A. Femtosecond laser-induced periodic surface structures. *J. Laser Appl.* **24**, 042006 (2012).

14.   Fuentes-Edfuf, Y. *et al.* Surface Plasmon Polaritons on Rough Metal Surfaces: Role

in the Formation of Laser-Induced Periodic Surface Structures. *ACS Omega* **4**, 6939–6946 (2019).

15. Sedao, X. *et al.* Self-Arranged Periodic Nanovoids by Ultrafast Laser-Induced Near-Field Enhancement. *ACS Photonics* **5**, 1418–1426 (2018).

16. Fuentes-Edfuf, Y. *et al.* Tuning the period of femtosecond laser induced surface structures in steel: From angled incidence to quill writing. *Appl. Surf. Sci.* **493**, 948–955 (2019).

17. Huang, M., Zhao, F., Cheng, Y., Xu, N. & Xu, Z. Origin of Laser-Induced Near-Subwavelength Ripples: Interference between Surface Plasmons and Incident Laser. *ACS Nano* **3**, 4062–4070 (2009).

18. Puerto, D. *et al.* Femtosecond laser-controlled self-assembly of amorphous-crystalline nanogratings in silicon. *Nanotechnology* **27**, 265602 (2016).

19. Fuentes-Edfuf, Y. *et al.* Coherent scatter-controlled phase-change grating structures in silicon using femtosecond laser pulses. *Sci. Rep.* **7**, 4594 (2017).

20. Soileau, M. Ripple structures associated with ordered surface defects in dielectrics. *IEEE J. Quantum Electron.* **20**, 464–467 (1984).

21. Bonse, J. *et al.* Applications of laser-induced periodic surface structures (LIPSS). *Proc SPIE* **10092**, 100920N (2017).

22. Höhm, S., Rosenfeld, A., Krüger, J. & Bonse, J. Femtosecond laser-induced periodic surface structures on silica. *J. Appl. Phys.* **112**, 014901 (2012).

23. Rudenko, A. *et al.* Spontaneous periodic ordering on the surface and in the bulk of dielectrics irradiated by ultrafast laser: a shared electromagnetic origin. *Sci. Rep.* **7**, 12306 (2017).

24. Heitz, J., Arenholz, E., Bauerle, D., Sauerbrey, R. & Phillips, H. M. Femtosecond excimer-laser-induced structure formation on polymers. *Appl. Phys. A* **59**, 289–293 (1994).

25. Emmony, D. C., Howson, R. P. & Willis, L. J. Laser mirror damage in germanium at 10.6 μm. *Appl. Phys. Lett.* **23**, 598–600 (1973).

26. Sipe, J. E., Young, J. F., Preston, J. S. & Van Driel, H. M. Laser-induced periodic surface structure. I. Theory. *Phys. Rev. B* **27**, 1141–1154 (1983).

27. Sipe, J. E. & van Driel, H. M. Laser Induced Periodic Surface Structure: An Experimental And Theoretical Review. in (ed. Ursu, I.) 302 (1989). doi:10.1117/12.950633.

28. Stratakis, E. *et al.* Laser engineering of biomimetic surfaces. *Mater. Sci. Eng. R Reports* **141**, 100562 (2020).

29. Bonse, J., Hohm, S., Kirner, S. V., Rosenfeld, A. & Kruger, J. Laser-Induced Periodic

Surface Structures-A Scientific Evergreen. *IEEE J. Sel. Top. Quantum Electron.* **23**, 2–3 (2017).

30. Ursu, I., Mihăilescu, I. N., Prokhorov, A. M., Konov, V. I. & Tokarev, V. N. On the role of the periodical structures induced by powerful laser irradiation of metallic surfaces in the energy coupling process. *Phys. B+C* **132**, 395–402 (1985).

31. Reif, J., Costache, F., Henyk, M. & Pandelov, S. V. Ripples revisited: non-classical morphology at the bottom of femtosecond laser ablation craters in transparent dielectrics. *Appl. Surf. Sci.* **197**–**198**, 891–895 (2002).

32. Skolski, J. Z. P. *et al.* Laser-induced periodic surface structures: Fingerprints of light localization. *Phys. Rev. B* **85**, 075320 (2012).

33. Huang, M., Zhao, F., Cheng, Y., Xu, N. & Xu, Z. Origin of laser-induced near-subwavelength ripples: Interference between surface plasmons and incident laser. *ACS Nano* **3**, 4062–4070 (2009).

34. Dufft, D., Rosenfeld, A., Das, S. K., Grunwald, R. & Bonse, J. Femtosecond laser-induced periodic surface structures revisited: A comparative study on ZnO. *J. Appl. Phys.* **105**, 034908 (2009).

35. Tsibidis, G. D., Skoulas, E., Papadopoulos, A. & Stratakis, E. Convection roll-driven generation of supra-wavelength periodic surface structures on dielectrics upon irradiation with femtosecond pulsed lasers. *Phys. Rev. B* **94**, 081305 (2016).

36. Ivanov, D. S. & Zhigilei, L. V. Combined atomistic-continuum modeling of short-pulse laser melting and disintegration of metal films. *Phys. Rev. B* **68**, 064114 (2003).

37. Zhigilei, L. V., Lin, Z. & Ivanov, D. S. Atomistic Modeling of Short Pulse Laser Ablation of Metals: Connections between Melting, Spallation, and Phase Explosion. *J. Phys. Chem. C* **113**, 11892–11906 (2009).

38. Varlamova, O., Costache, F., Reif, J. & Bestehorn, M. Self-organized pattern formation upon femtosecond laser ablation by circularly polarized light. *Appl. Surf. Sci.* **252**, 4702–4706 (2006).

39. Rudenko, A., Mauclair, C., Garrelie, F., Stoian, R. & Colombier, J. P. Self-organization of surfaces on the nanoscale by topography-mediated selection of quasi-cylindrical and plasmonic waves. *Nanophotonics* **8**, 459–465 (2019).

40. Miyaji, G. & Miyazaki, K. Origin of periodicity in nanostructuring on thin film surfaces ablated with femtosecond laser pulses. *Opt. Express* **16**, 16265 (2008).

41. Tsibidis, G. D., Barberoglou, M., Loukakos, P. A., Stratakis, E. & Fotakis, C. Dynamics of ripple formation on silicon surfaces by ultrashort laser pulses in subablation conditions. *Phys. Rev. B* **86**, 115316 (2012).

42. Tsibidis, G. D. *et al.* Modelling periodic structure formation on 100Cr6 steel after irradiation with femtosecond-pulsed laser beams. *Appl. Phys. A* **124**, 27 (2018).

43. Höhm, S., Rosenfeld, A., Krüger, J. & Bonse, J. Femtosecond diffraction dynamics of laser-induced periodic surface structures on fused silica. *Appl. Phys. Lett.* **102**, 054102 (2013).

44. Tsibidis, G. D., Fotakis, C. & Stratakis, E. From ripples to spikes: A hydrodynamical mechanism to interpret femtosecond laser-induced self-assembled structures. *Phys. Rev. B* **92**, 041405 (2015).

45. Zhang, J., Zhang, L. & Xu, W. Surface plasmon polaritons: physics and applications. *J. Phys. D. Appl. Phys.* **45**, 113001 (2012).

46. Lin, Z., Zhigilei, L. V. & Celli, V. Electron-phonon coupling and electron heat capacity of metals under conditions of strong electron-phonon nonequilibrium. *Phys. Rev. B* **77**, 075133 (2008).

47. van Driel, H. M. Kinetics of high-density plasmas generated in Si by 1.06- and 0.53-μm picosecond laser pulses. *Phys. Rev. B* **35**, 8166–8176 (1987).

48. Chichkov, B. N., Momma, C., Nolte, S., Von Alvensleben, F. & Tünnermann, A. Femtosecond, picosecond and nanosecond laser ablation of solids. *Appl. Phys. A Mater. Sci. Process.* **63**, 109–115 (1996).

49. Tsibidis, G. D., Barberoglou, M., Loukakos, P. A., Stratakis, E. & Fotakis, C. Dynamics of ripple formation on silicon surfaces by ultrashort laser pulses in subablation conditions. *Phys. Rev. B - Condens. Matter Mater. Phys.* **86**, 115316 (2012).

50. Phillips, K. C., Gandhi, H. H., Mazur, E. & Sundaram, S. K. Ultrafast laser processing of materials: a review. *Adv. Opt. Photonics* **7**, 684 (2015).

51. Rudenko, A. *et al.* Spontaneous periodic ordering on the surface and in the bulk of dielectrics irradiated by ultrafast laser: A shared electromagnetic origin. *Sci. Rep.* **7**, 1–14 (2017).

52. Liang, F., Vallée, R. & Chin, S. L. Mechanism of nanograting formation on the surface of fused silica. *Opt. Express* **20**, 4389 (2012).

53. Liang, F., Bouchard, J., Leang Chin, S. & Vallée, R. Defect-assisted local field rearrangement during nanograting formation with femtosecond pulses. *Appl. Phys. Lett.* **107**, 061903 (2015).

54. Wachter, G. *et al.* Ab Initio Simulation of Electrical Currents Induced by Ultrafast Laser Excitation of Dielectric Materials. *Phys. Rev. Lett.* **113**, 087401 (2014).

55. Vorobyev, A. Y. & Guo, C. Direct femtosecond laser surface nano/microstructuring and its applications. *Laser Photon. Rev.* **7**, 385–407 (2013).

56. Guay, J.-M. *et al.* Laser-induced plasmonic colours on metals. *Nat. Commun.* **8**,

16095 (2017).

57. Siddique, R. H., Gomard, G. & Hölscher, H. The role of random nanostructures for the omnidirectional anti-reflection properties of the glasswing butterfly. *Nat. Commun.* **6**, 6909 (2015).

58. Quartau, J. A. & Simões, P. C. Cicada cretensis sp. n. (Hemiptera, Cicadidae) from southern Greece. *Biologia (Bratisl).* **605**, 489–494 (2005).

59. Papadopoulos, A. *et al.* Biomimetic Omnidirectional Antireflective Glass via Direct Ultrafast Laser Nanostructuring. *Adv. Mater.* 1901123 (2019) doi:10.1002/adma.201901123.

60. Barmina, E. V., Serkov, A. A., Shafeev, G. A., Stratakis, E. & Fotakis, C. Nanostructuring of single-crystal silicon carbide by femtosecond laser irradiation in a liquid. *Phys. Wave Phenom.* **22**, 15–18 (2014).

61. Chen, J.-T., Lai, W.-C., Kao, Y.-J., Yang, Y.-Y. & Sheu, J.-K. Laser-induced periodic structures for light extraction efficiency enhancement of GaN-based light emitting diodes. *Opt. Express* **20**, 5689 (2012).

62. Xiong, P. *et al.* Ultraviolet luminescence enhancement of ZnO two-dimensional periodic nanostructures fabricated by the interference of three femtosecond laser beams. *New J. Phys.* **13**, 023044 (2011).

63. de Prado, E. *et al.* Optical spectroscopy study of nano- and microstructures fabricated by femtosecond laser pulses on ZnO based systems. *CrystEngComm* **20**, 2952–2960 (2018).

64. Taylor, R., Hnatovsky, C. & Simova, E. Applications of femtosecond laser induced self-organized planar nanocracks inside fused silica glass. *Laser Photonics Rev.* **2**, 26–46 (2008).

65. Kazansky, P. *et al.* Eternal 5D data storage via ultrafast-laser writing in glass. *SPIE Newsroom* (2016) doi:10.1117/2.1201603.006365.

66. Drevinskas, R. & Kazansky, P. G. High-performance geometric phase elements in silica glass. *APL Photonics* **2**, 066104 (2017).

67. Liu, Y. *et al.* Micromodification of element distribution in glass using femtosecond laser irradiation. *Opt. Lett.* **34**, 136 (2009).

68. Fernandez, T. T. *et al.* Bespoke photonic devices using ultrafast laser driven ion migration in glasses. *Prog. Mater. Sci.* **94**, 68–113 (2018).

69. del Hoyo, J. *et al.* Control of waveguide properties by tuning femtosecond laser induced compositional changes. *Appl. Phys. Lett.* **105**, 131101 (2014).

70. del Hoyo, J. *et al.* High-Efficiency Waveguide Optical Amplifiers and Lasers via FS-Laser Induced Local Modification of the Glass Composition. *J. Light. Technol.* **35**,

2955–2959 (2017).

71. Dias, A. *et al.* Femtosecond laser writing of photonic devices in borate glasses compositionally designed to be laser writable. *Opt. Lett.* **43**, 2523 (2018).

72. Yu, Y., Bai, S., Wang, S. & Hu, A. Ultra-Short Pulsed Laser Manufacturing and Surface Processing of Microdevices. *Engineering* **4**, 779–786 (2018).

73. Papadopoulos, A. *et al.* Biomimetic Omnidirectional Antireflective Glass via Direct Ultrafast Laser Nanostructuring. *Adv. Mater.* **1901123**, 1901123 (2019).

74. Linklater, D. P., Juodkazis, S. & Ivanova, E. P. Nanofabrication of mechano-bactericidal surfaces. *Nanoscale* **9**, 16564–16585 (2017).

75. Ngo, C. V. & Chun, D. M. Effect of Heat Treatment Temperature on the Wettability Transition from Hydrophilic to Superhydrophobic on Laser-Ablated Metallic Surfaces. *Adv. Eng. Mater.* **20**, 1–11 (2018).

76. Yao, J. *et al.* Selective appearance of several laser-induced periodic surface structure patterns on a metal surface using structural colors produced by femtosecond laser pulses. *Appl. Surf. Sci.* **258**, 7625–7632 (2012).

77. Zhang, J., Gecevičius, M., Beresna, M. & Kazansky, P. G. Seemingly Unlimited Lifetime Data Storage in Nanostructured Glass. *Phys. Rev. Lett.* **112**, 033901 (2014).

78. Vorobyev, A. Y. & Guo, C. Multifunctional surfaces produced by femtosecond laser pulses. *J. Appl. Phys.* **117**, 033103 (2015).

79. Hermens, U. *et al.* Mimicking lizard-like surface structures upon ultrashort laser pulse irradiation of inorganic materials. *Appl. Surf. Sci.* **418**, 499–507 (2017).

80. Kirner, S. V. *et al.* Mimicking bug-like surface structures and their fluid transport produced by ultrashort laser pulse irradiation of steel. *Appl. Phys. A* **123**, 754 (2017).

81. Florian Baron, C. *et al.* Biomimetic surface structures in steel fabricated with femtosecond laser pulses: influence of laser rescanning on morphology and wettability. *Beilstein J. Nanotechnol.* **9**, 2802–2812 (2018).

82. Kietzig, A.-M., Hatzikiriakos, S. G. & Englezos, P. Patterned Superhydrophobic Metallic Surfaces. *Langmuir* **25**, 4821–4827 (2009).

83. Martínez-Calderon, M. *et al.* Femtosecond laser fabrication of highly hydrophobic stainless steel surface with hierarchical structures fabricated by combining ordered microstructures and LIPSS. *Appl. Surf. Sci.* **374**, 81–89 (2016).

84. Florian, C. *et al.* Controlling the Wettability of Steel Surfaces Processed with Femtosecond Laser Pulses. *ACS Appl. Mater. Interfaces* **10**, 36564–36571 (2018).

85. Yong, J., Chen, F., Yang, Q. & Hou, X. Femtosecond laser controlled wettability of solid surfaces. *Soft Matter* **11**, 8897–8906 (2015).

86. Vorobyev, A. Y. & Guo, C. Laser turns silicon superwicking. *Opt. Express* **18**, 6455 (2010).

87. Zorba, V. *et al.* Biomimetic Artificial Surfaces Quantitatively Reproduce the Water Repellency of a Lotus Leaf. *Adv. Mater.* **20**, 4049–4054 (2008).

88. Lin, Y. *et al.* Durable and robust transparent superhydrophobic glass surfaces fabricated by a femtosecond laser with exceptional water repellency and thermostability. *J. Mater. Chem. A* **6**, 9049–9056 (2018).

89. Stroj, S. *et al.* Transparent superhydrophobic surfaces with high adhesion generated by the combination of femtosecond laser structuring and wet oxidation. *Appl. Surf. Sci.* **420**, 550–557 (2017).

90. López, A. J., Ramil, A., Pozo-Antonio, J. S., Rivas, T. & Pereira, D. Ultrafast Laser Surface Texturing: A Sustainable Tool to Modify Wettability Properties of Marble. *Sustainability* **11**, 4079 (2019).

91. Liang, C. *et al.* Preparation of Hydrophobic and Oleophilic Surface of 316 L Stainless Steel by Femtosecond Laser Irradiation in Water. *J. Dispers. Sci. Technol.* **35**, 1345–1350 (2014).

92. Stark, T., Kiedrowski, T., Marschall, H. & Lasagni, A. F. Avoiding Starvation in Tribocontact Through Active Lubricant Transport in Laser Textured Surfaces. *Lubricants* **7**, 54 (2019).

93. Dean, B. & Bhushan, B. Shark-skin surfaces for fluid-drag reduction in turbulent flow: a review. *Philos. Trans. R. Soc. A Math. Phys. Eng. Sci.* **368**, 4775–4806 (3000).

94. Bonse, J., Kirner, S. V., Griepentrog, M., Spaltmann, D. & Krüger, J. Femtosecond Laser Texturing of Surfaces for Tribological Applications. *Materials (Basel).* **11**, 801 (2018).

95. Buchberger, G. *et al.* Bio-inspired "fluidic diode" for large-area unidirectional passive water transport even against gravity. *Sensors Actuators A Phys.* **283**, 375–385 (2018).

96. Paradisanos, I., Fotakis, C., Anastasiadis, S. H. & Stratakis, E. Gradient induced liquid motion on laser structured black Si surfaces. *Appl. Phys. Lett.* **107**, 111603 (2015).

97. Osellame, R., Hoekstra, H. J. W. M., Cerullo, G. & Pollnau, M. Femtosecond laser microstructuring: an enabling tool for optofluidic lab-on-chips. *Laser Photon. Rev.* **5**, 442–463 (2011).

98. Shinonaga, T. *et al.* Formation of periodic nanostructures using a femtosecond laser to control cell spreading on titanium. *Appl. Phys. B* **119**, 493–496 (2015).

99. Rebollar, E. *et al.* Proliferation of aligned mammalian cells on laser-nanostructured polystyrene. *Biomaterials* **29**, 1796–1806 (2008).

100. Ranella, A., Barberoglou, M., Bakogianni, S., Fotakis, C. & Stratakis, E. Tuning cell adhesion by controlling the roughness and wettability of 3D micro/nano silicon structures. *Acta Biomater.* **6**, 2711–2720 (2010).

101. Simitzi, C. *et al.* Laser fabricated discontinuous anisotropic microconical substrates as a new model scaffold to control the directionality of neuronal network outgrowth. *Biomaterials* **67**, 115–128 (2015).

102. Martínez-Calderon, M. *et al.* Surface micro- and nano-texturing of stainless steel by femtosecond laser for the control of cell migration. *Sci. Rep.* **6**, 36296 (2016).

103. Jeon, H. *et al.* Directing cell migration and organization via nanocrater-patterned cell-repellent interfaces. *Nat. Mater.* **14**, 918–923 (2015).

104. Yiannakou, C. *et al.* Cell patterning via laser micro/nano structured silicon surfaces. *Biofabrication* **9**, 025024 (2017).

105. Heitz, J. *et al.* Femtosecond laser-induced microstructures on Ti substrates for reduced cell adhesion. *Appl. Phys. A* **123**, 734 (2017).

106. Zerva, I. *et al.* Implantable vaccine development using in vitro antigen-pulsed macrophages absorbed on laser micro-structured Si scaffolds. *Vaccine* **33**, 3142–3149 (2015).

107. Cunha, A. *et al.* Femtosecond laser surface texturing of titanium as a method to reduce the adhesion of Staphylococcus aureus and biofilm formation. *Appl. Surf. Sci.* **360**, 485–493 (2016).

108. Epperlein, N. *et al.* Influence of femtosecond laser produced nanostructures on biofilm growth on steel. *Appl. Surf. Sci.* **418**, 420–424 (2017).

109. Lutey, A. H. A. *et al.* Towards Laser-Textured Antibacterial Surfaces. *Sci. Rep.* **8**, 10112 (2018).

110. Schwibbert, K., Menzel, F., Epperlein, N., Bonse, J. & Krüger, J. Bacterial Adhesion on Femtosecond Laser-Modified Polyethylene. *Materials (Basel).* **12**, 3107 (2019).

111. Zhan, Q. Cylindrical vector beams: from mathematical concepts to applications. *Adv. Opt. Photonics* **1**, 1 (2009).

112. Liu, J. M. Simple technique for measurements of pulsed Gaussian-beam spot sizes. *Opt. Lett.* **7**, 196 (1982).

113. Self, S. A. Focusing of spherical Gaussian beams. *Appl. Opt.* **22**, 658 (1983).

114. Will, M., Nolte, S., Chichkov, B. N. & Tünnermann, A. Optical properties of waveguides fabricated in fused silica by femtosecond laser pulses. *Appl. Opt.* **41**, 4360 (2002).

115. Hall, D. G. Vector-beam solutions of Maxwell's wave equation. *Opt. Lett.* **21**, 9 (1996).

116. Drevinskas, R. *et al.* Laser material processing with tightly focused cylindrical vector beams. *Appl. Phys. Lett.* **108**, 221107 (2016).

117. Porfirev, A. P., Ustinov, A. V. & Khonina, S. N. Polarization conversion when focusing cylindrically polarized vortex beams. *Sci. Rep.* **6**, 6 (2016).

118. Papadopoulos, A., Skoulas, E., Tsibidis, G. D. & Stratakis, E. Formation of periodic surface structures on dielectrics after irradiation with laser beams of spatially variant polarisation: a comparative study. *Appl. Phys. A Mater. Sci. Process.* **124**, 146 (2018).

119. JJ Nivas, J. *et al.* Surface structures with unconventional patterns and shapes generated by femtosecond structured light fields. *Sci. Rep.* **8**, 1–11 (2018).

120. Nivas, J. J. J. *et al.* Direct Femtosecond Laser Surface Structuring with Optical Vortex Beams Generated by a q-plate. *Sci. Rep.* **5**, 17929 (2015).

121. Zhan, Q. & Leger, J. Focus shaping using cylindrical vector beams. *Opt. Express* **10**, 324 (2002).

122. Pattanaporkratana, A., Park, C. S., Maclennan, J. E. & Clark, N. A. Manipulation of Disk-Shaped Islands on Freely Suspended Smectic Films and Bubbles Using Optical Tweezers. *Ferroelectrics* **310**, 131–135 (2004).

123. Feng, S. & Winful, H. G. Physical origin of the Gouy phase shift. *Opt. Lett.* **26**, 485 (2001).

124. Allen, L., Beijersbergen, M. W., Spreeuw, R. J. C. & Woerdman, J. P. Orbital angular momentum of light and the transformation of Laguerre-Gaussian laser modes. *Phys. Rev. A* **45**, 8185–8189 (1992).

125. Beresna, M., Gecevičius, M., Kazansky, P. G. & Gertus, T. Radially polarized optical vortex converter created by femtosecond laser nanostructuring of glass. *Appl. Phys. Lett.* **98**, 201101 (2011).

126. Skoulas, E., Manousaki, A., Fotakis, C. & Stratakis, E. Biomimetic surface structuring using cylindrical vector femtosecond laser beams. *Sci. Rep.* **7**, 45114 (2017).

127. Gregorčič, P., Sedlaček, M., Podgornik, B. & Reif, J. Formation of laser-induced periodic surface structures (LIPSS) on tool steel by multiple picosecond laser pulses of different polarizations. *Appl. Surf. Sci.* **387**, 698–706 (2016).

128. JJ Nivas, J. *et al.* Femtosecond laser surface structuring of silicon with Gaussian and optical vortex beams. *Appl. Surf. Sci.* **418**, 565–571 (2017).

129. Allegre, O. *et al.* Ultra-short pulse laser micro-machining of steel with radial and azimuthal polarization. 22–23 (2012).

130. Hnatovsky, C., Shvedov, V., Krolikowski, W. & Rode, A. Revealing local field structure of focused ultrashort pulses. *Phys. Rev. Lett.* **106**, 123901 (2011).

131. Dusser, B. *et al.* Controlled nanostructrures formation by ultra fast laser pulses for color marking. *Opt. Express* **18**, 2913 (2010).

132. Voisiat, B., Wang, W., Holzhey, M. & Lasagni, A. F. Improving the homogeneity of diffraction based colours by fabricating periodic patterns with gradient spatial period using Direct Laser Interference Patterning. 2–10 (2019) doi:10.1038/s41598-019-44212-4.

133. Diaci, J., Bračun, D., Gorkič, A. & Možina, J. Rapid and flexible laser marking and engraving of tilted and curved surfaces. *Opt. Lasers Eng.* **49**, 195–199 (2011).

134. Yao, A. M. & Padgett, M. J. Orbital angular momentum: origins, behavior and applications. *Adv. Opt. Photonics* **3**, 161 (2011).

135. Willis, D. A. & Xu, X. Heat transfer and phase change during picosecond laser ablation of nickel. *Int. J. Heat Mass Transf.* **45**, 3911–3918 (2002).

136. Chen, A. M. *et al.* Modeling of femtosecond laser damage threshold on the two-layer metal films. *Appl. Surf. Sci.* **257**, 1678–1683 (2010).

137. Colombier, J. P. *et al.* Effects of electron-phonon coupling and electron diffusion on ripples growth on ultrafast-laser-irradiated metals. *J. Appl. Phys.* **111**, 024902 (2012).

138. Rethfeld, B., Sokolowski-Tinten, K., von der Linde, D. & Anisimov, S. I. Timescales in the response of materials to femtosecond laser excitation. *Appl. Phys. A* **79**, 767–769 (2004).

139. Anisimov, S., Kapeliovich, B. & Perel'Man, T. Electron emission from metal surfaces exposed to ultrashort laser pulses. *Sov. J. Exp. Theor. Phys.* **39**, 776–781 (1974).

140. Garrelie, F. *et al.* Evidence of surface plasmon resonance in ultrafast laser-induced ripples. *Opt. Express* **19**, 9035 (2011).

141. Gnilitskyi, I. *et al.* High-speed manufacturing of highly regular femtosecond laser-induced periodic surface structures: Physical origin of regularity. *Sci. Rep.* **7**, 1–11 (2017).

142. Jin, Y. *et al.* Dynamic modulation of spatially structured polarization fields for real-time control of ultrafast laser-material interactions. *Opt. Express* **21**, 25333 (2013).

143. Li, G. *et al.* Realization of diverse displays for multiple color patterns on metal surfaces. *Appl. Surf. Sci.* **316**, 451–455 (2014).

144. Vorobyev, A. Y. & Guo, C. Colorizing metals with femtosecond laser pulses. **041914**, 1–4 (2015).

145. Phys, J. A. Spectral and polarization responses of femtosecond laser-induced periodic surface structures on metals. **043513**, 101–104 (2012).

146. Tamamura, Y. & Miyaji, G. Structural coloration of a stainless steel surface with

homogeneous nanograting formed by femtosecond laser ablation. *Opt. Mater. Express* **9**, 2902–2909 (2019).

147. Li, G. *et al.* Evolution of aluminum surface irradiated by femtosecond laser pulses with different pulse overlaps. *Appl. Surf. Sci.* **276**, 203–209 (2013).

148. Ionin, A. A. *et al.* Femtosecond laser color marking of metal and semiconductor surfaces. *Appl. Phys. A Mater. Sci. Process.* **107**, 301–305 (2012).

149. Ahsan, M. S., Ahmed, F., Kim, Y. G., Lee, M. S. & Jun, M. B. G. Colorizing stainless steel surface by femtosecond laser induced micro/nano-structures. *Appl. Surf. Sci.* **257**, 7771–7777 (2011).

150. Wang, L., Chen, Q., Cao, X., Wang, X. & Juodkazis, S. Plasmonic nano-printing : large-area nanoscale energy deposition for ef fi cient surface texturing. 1–7 (2017) doi:10.1038/lsa.2017.112.

151. Højlund-nielsen, E., Weirich, J. & Kristensen, A. Angle-independent structural colors of silicon. doi:10.1117/1.JNP.8.083988.

152. Yetisen, A. K. *et al.* Color-Selective 2 . 5D Holograms on Large-Area Flexible Substrates for Sensing and Multilevel Security. 1589–1600 (2016) doi:10.1002/adom.201600162.

153. Jwad, T., Penchev, P., Nasrollahi, V. & Dimov, S. Applied Surface Science Laser induced ripples ' gratings with angular periodicity for fabrication of diffraction holograms. *Appl. Surf. Sci.* **453**, 449–456 (2018).

154. Romano, J. M., Garcia-Giron, A., Penchev, P. & Dimov, S. Triangular laser-induced submicron textures for functionalising stainless steel surfaces. *Appl. Surf. Sci.* **440**, 162–169 (2018).

155. Hecht, E. *Optics. Optics 4th edition by Eugene Hecht Reading MA AddisonWesley Publishing Company 2001* (2001). doi:10.1119/1.3274347.

156. Palmer, C. Diffraction Grating Handbook. *J. Opt. Soc. Am.* **46**, 20–23 (2005).

157. Davis, K. M., Miura, K., Sugimoto, N. & Hirao, K. Writing waveguides in glass with a femtosecond laser. *Opt. Lett.* **21**, 1729 (1996).

158. Glezer, E. N. & Mazur, E. Ultrafast-laser driven micro-explosions in transparent materials. *Appl. Phys. Lett.* **71**, 882–884 (1997).

159. Sugioka, K. & Cheng, Y. Ultrafast lasers-reliable tools for advanced materials processing. *Light Sci. Appl.* **3**, e149 (2014).

160. Kazansky, P. *et al.* Eternal 5D data storage via ultrafast-laser writing in glass. *SPIE Newsroom* **9736**, 1–16 (2016).

161. Patel, A., Svirko, Y., Durfee, C. & Kazansky, P. G. Direct Writing with Tilted-Front Femtosecond Pulses. *Sci. Rep.* **7**, 12928 (2017).

162. Stratakis, E. I. & Zorba, V. *Biomimetic Artificial Nanostructured Surfaces*. *Nanotechnologies for the Life Sciences* vol. 7 (2012).

163. Fraggelakis, F., Mincuzzi, G., Lopez, J., Manek-Hönninger, I. & Kling, R. Texturing metal surface with MHz ultra-short laser pulses. *Opt. Express* **25**, 18131 (2017).

164. Ta, V. D. *et al.* Laser textured superhydrophobic surfaces and their applications for homogeneous spot deposition. *Appl. Surf. Sci.* **365**, 153–159 (2016).

165. Gnilitskyi, I., Rota, A., Gualtieri, E., Valeri, S. & Orazi, L. Tribological Properties of High-Speed Uniform Femtosecond Laser Patterning on Stainless Steel. *Lubricants* **7**, 83 (2019).

166. Simitzi, C. *et al.* Laser fabricated discontinuous anisotropic microconical substrates as a new model scaffold to control the directionality of neuronal network outgrowth. *Biomaterials* **67**, 115–128 (2015).

167. Zhang, J. *et al.* Eternal 5D data storage by ultrafast laser writing in glass. in (eds. Klotzbach, U., Washio, K. & Arnold, C. B.) 97360U (2016). doi:10.1117/12.2220600.

168. Beresna, M., Gecevičius, M. & Kazansky, P. G. Polarization sensitive elements fabricated by femtosecond laser nanostructuring of glass [Invited]. *Opt. Mater. Express* **1**, 783 (2011).

169. Poumellec, B., Lancry, M., Chahid-Erraji, A. & Kazansky, P. G. Modification thresholds in femtosecond laser processing of pure silica: review of dependencies on laser parameters [Invited]. *Opt. Mater. Express* **1**, 766 (2011).

170. Sakka, S. & Mackenzie, J. D. Relation between apparent glass transition temperature and liquids temperature for inorganic glasses. *J. Non. Cryst. Solids* **6**, 145–162 (1971).

171. Lei, Y., Zhang, N., Yang, J. & Guo, C. Femtosecond laser eraser for controllable removing periodic microstructures on Fe-based metallic glass surfaces. *Opt. Express* **26**, 5102 (2018).

172. Konidakis, I., Varsamis, C. P. E. & Kamitsos, E. I. Effect of synthesis method on the structure and properties of AgPO3-based glasses. *J. Non. Cryst. Solids* **357**, 2684–2689 (2011).

173. Palles, D., Konidakis, I., Varsamis, C. P. E. & Kamitsos, E. I. Vibrational spectroscopic and bond valence study of structure and bonding in Al 2 O 3 -containing AgI–AgPO 3 glasses. *RSC Adv.* **6**, 16697–16710 (2016).

174. Eichstädt, J., Römer, G. R. B. E. & Huis in 't Veld, A. J. Determination of irradiation parameters for laser-induced periodic surface structures. *Appl. Surf. Sci.* **264**, 79–87 (2013).

175. Chimier, B. *et al.* Damage and ablation thresholds of fused-silica in femtosecond

regime. *Phys. Rev. B* **84**, 094104 (2011).

176. Di Niso, F. *et al.* Role of heat accumulation on the incubation effect in multi-shot laser ablation of stainless steel at high repetition rates. *Opt. Express* **22**, 12200 (2014).

177. Sakurai, H. *et al.* Effect of damage incubation in the laser grooving of sapphire. *J. Appl. Phys.* **125**, 173109 (2019).

178. Ruiz de la Cruz, A., Lahoz, R., Siegel, J., de la Fuente, G. F. & Solis, J. High speed inscription of uniform, large-area laser-induced periodic surface structures in Cr films using a high repetition rate fs laser. *Opt. Lett.* **39**, 2491 (2014).

179. Tsibidis, G. D. Ultrafast dynamics of non-equilibrium electrons and strain generation under femtosecond laser irradiation of Nickel. *Appl. Phys. A Mater. Sci. Process.* **124**, 1–14 (2018).

180. Gnilitskyi, I., Gruzdev, V., Bulgakova, N. M., Mocek, T. & Orazi, L. Mechanisms of high-regularity periodic structuring of silicon surface by sub-MHz repetition rate ultrashort laser pulses. *Appl. Phys. Lett.* **109**, 107–112 (2016).

181. Taravati, S. & Eleftheriades, G. V. Generalized Space-Time-Periodic Diffraction Gratings: Theory and Applications. *Phys. Rev. Appl.* **12**, 024026 (2019).

182. Delestre, A. *et al.* Towards second-harmonic generation micropatterning of glass surface. *Appl. Phys. Lett.* **96**, 091908 (2010).

183. Konidakis, I., Psilodimitrakopoulos, S., Kosma, K., Lemonis, A. & Stratakis, E. Effect of composition and temperature on the second harmonic generation in silver phosphate glasses. *Opt. Mater. (Amst).* **75**, 796–801 (2018).

184. Vangheluwe, M. *et al.* Enhancement of nanograting formation assisted by silver ions in a sodium gallophosphate glass. *Opt. Lett.* **39**, 5491 (2014).

185. Marquestaut, N. *et al.* Three-Dimensional Silver Nanoparticle Formation Using Femtosecond Laser Irradiation in Phosphate Glasses: Analogy with Photography. *Adv. Funct. Mater.* **24**, 5824–5832 (2014).

186. Jain, C. *et al.* Silver metaphosphate glass wires inside silica fibers—a new approach for hybrid optical fibers. *Opt. Express* **24**, 3258 (2016).

187. Konidakis, I., Zito, G. & Pissadakis, S. Silver plasmon resonance effects in AgPO_3/silica photonic bandgap fiber. *Opt. Lett.* **39**, 3374 (2014).

188. Ahmmed, K. M. T., Ling, E. J. Y., Servio, P. & Kietzig, A.-M. Introducing a new optimization tool for femtosecond laser-induced surface texturing on titanium, stainless steel, aluminum and copper. *Opt. Lasers Eng.* **66**, 258–268 (2015).

189. Kreibig, U. Small silver particles in photosensitive glass: Their nucleation and growth. *Appl. Phys.* **10**, 255–264 (1976).

190. Shestakov, M. V. *et al.* The size and structure of Ag particles responsible for surface plasmon effects and luminescence in Ag homogeneously doped bulk glass. *J. Appl. Phys.* **114**, 073102 (2013).

191. Kersey, A. D. *et al.* Fiber grating sensors. *J. Light. Technol.* **15**, 1442–1463 (1997).

192. Hertz, H. *Electric Waves*. *Electric Waves* (Macmillan & Co, 1893).

193. Bird, G. R. & Parrish, M. The Wire Grid as a Near-Infrared Polarizer. *J. Opt. Soc. Am.* **50**, 886 (1960).

194. Chou, S. Y. & Krauss, P. R. Imprint lithography with sub-10 nm feature size and high throughput. *Microelectron. Eng.* **35**, 237–240 (1997).

195. Wang, X. *et al.* Free-standing SU-8 subwavelength gratings fabricated by UV curing imprint. *Microelectron. Eng.* **85**, 910–913 (2008).

196. Kim, W. *et al.* Nanogap Engineering for Enhanced Transmission of Wire Grid Polarizers in Mid-Wavelength Infrared Region. *Sci. Rep.* **9**, 1–10 (2019).

197. Cho, Y. T. Fabrication of wire grid polarizer for spectroscopy application: From ultraviolet to terahertz. *Appl. Spectrosc. Rev.* **53**, 224–245 (2018).

198. Liao, Y. L. & Zhao, Y. Design of wire-grid polarizer with effective medium theory. *Opt. Quantum Electron.* **46**, 641–647 (2014).

199. Şengül, H., Theis, T. L. & Ghosh, S. Toward Sustainable Nanoproducts. *J. Ind. Ecol.* **12**, 329–359 (2008).

200. Fast, D. B. *et al.* Wire-grid THz polarizers manufactured by laser micromachining of metal films on a polymer membrane. in *2011 International Conference on Infrared, Millimeter, and Terahertz Waves* 1–2 (IEEE, 2011). doi:10.1109/irmmw-THz.2011.6104851.

201. Domke, M. *et al.* Understanding thin film laser ablation: The role of the effective penetration depth and the film thickness. *Phys. Procedia* **56**, 1007–1014 (2014).

202. Gaković, B. *et al.* Partial ablation of Ti/Al nano-layer thin film by single femtosecond laser pulse. *J. Appl. Phys.* **122**, 223106 (2017).

203. Gray, J., Thomas, P. & Zhu, X. D. Laser pointing stability measured by an oblique-incidence optical transmittance difference technique. *Rev. Sci. Instrum.* **72**, 3714–3717 (2001).

204. Huynh, T. T. D., Petit, A. & Semmar, N. Picosecond laser induced periodic surface structure on copper thin films. *Appl. Surf. Sci.* **302**, 109–113 (2014).

205. Dostovalov, A. V. *et al.* LIPSS on thin metallic films: New insights from multiplicity of laser-excited electromagnetic modes and efficiency of metal oxidation. *Appl. Surf. Sci.* **491**, 650–658 (2019).

206. Reyes-Contreras, A. *et al.* Laser-induced periodic surface structures on bismuth

thin films with ns laser pulses below ablation threshold. *Opt. Mater. Express* **7**, 1777 (2017).

207. Rodríguez, A. *et al.* Femtosecond laser-induced periodic surface nanostructuring of sputtered platinum thin films. *Appl. Surf. Sci.* **351**, 135–139 (2015).

208. Bonse, J., Baudach, S., Krüger, J., Kautek, W. & Lenzner, M. Femtosecond laser ablation of silicon-modification thresholds and morphology. *Appl. Phys. A Mater. Sci. Process.* **74**, 19–25 (2002).

209. He, S., Nivas, J. J., Vecchione, A., Hu, M. & Amoruso, S. On the generation of grooves on crystalline silicon irradiated by femtosecond laser pulses. *Opt. Express* **24**, 3238 (2016).

210. Jee, Y., Becker, M. F. & Walser, R. M. Laser-induced damage on single-crystal metal surfaces. *J. Opt. Soc. Am. B* **5**, 648 (1988).

211. Nivas, J. J., Anoop, K. K., Bruzzese, R., Philip, R. & Amoruso, S. Direct femtosecond laser surface structuring of crystalline silicon at 400 nm. *Appl. Phys. Lett.* **112**, 121601 (2018).

212. Zhang, L., Cao, X. W., Li, S. G., Xiang, R. Y. & Sun, H. C. Investigation of Femtosecond Laser Ablation Threshold for Nickel Template. *Appl. Mech. Mater.* **633–634**, 665–670 (2014).

213. Hashida, M. *et al.* Threshold Fluence for Femtosecond Laser Nanoablation for Metals. *Electron. Commun. Japan* **99**, 88–95 (2016).

214. Qi, L., Nishii, K. & Namba, Y. Regular subwavelength surface structures induced by femtosecond laser pulses on stainless steel. *Opt. Lett.* **34**, 1846 (2009).

215. Qi, L., Li, F., Lin, H. & Hu, J. On the formation of regular sub-wavelength ripples by femtosecond laser pulses on silicon. *Optik (Stuttg).* **126**, 4905–4909 (2015).

216. Kim, K. H., Akase, Z., Suzuki, T. & Shindo, D. Charging Effects on SEM/SIM Contrast of Metal/Insulator System in Various Metallic Coating Conditions. *Mater. Trans.* **51**, 1080–1083 (2010).

217. Yeh, P. A new optical model for wire grid polarizers. *Opt. Commun.* **26**, 289–292 (1978).

218. Tyan, R.-C. *et al.* Design, fabrication, and characterization of form-birefringent multilayer polarizing beam splitter. *J. Opt. Soc. Am. A* **14**, 1627 (1997).

219. Raguin, D. H. & Morris, G. M. Antireflection structured surfaces for the infrared spectral region. *Appl. Opt.* **32**, 1154 (1993).

220. Tyan, R.-C., Sun, P.-C., Scherer, A. & Fainman, Y. Polarizing beam splitter based on the anisotropic spectral reflectivity characteristic of form-birefringent multilayer gratings. *Opt. Lett.* **21**, 761 (1996).

221. Liao, Y.-L. & Zhao, Y. Design of wire-grid polarizer with effective medium theory. *Opt. Quantum Electron.* **46**, 641–647 (2014).

222. Kameda, S., Mizutani, A. & Kikuta, H. Effective Medium Theory for Calculating Reflectance from Metal–Dielectric Multilayered Structure. *Jpn. J. Appl. Phys.* **51**, 042202 (2012).

223. Moon, S. & Kim, D. Fitting-based determination of an effective medium of a metallic periodic structure and application to photonic crystals. *J. Opt. Soc. Am. A* **23**, 199 (2006).

224. Johnson, P. B. & Christy, R. W. Optical Constants of the Noble Metals. *Phys. Rev. B* **6**, 4370–4379 (1972).

225. Born, M. *et al. Principles of Optics. Principles of Optics* (Cambridge University Press, 1999). doi:10.1017/cbo9781139644181.

226. Hwang, T. Y. & Guo, C. Angular effects of nanostructure-covered femtosecond laser induced periodic surface structures on metals. *J. Appl. Phys.* **108**, 073523 (2010).

Acknowledgments

I would like to express my deepest gratitude to my supervisor Dr. Emmanuel Stratakis for the unlimited support and excellent collaboration all this time during my thesis. I think that there are no words to describe my appreciation for him since I have considered him to be not only a scientific supervisor but also a great friend. I would also like to thank from the bottom of my heart my other supervisor Prof. Dimitris Papazoglou for his support and belief in me and whose office door was always open for any of my minor or major concerns. Also Prof. George Kioseoglou for gladly being in the 3-member committee of this thesis and was always pleasant and helpful.

I can't continue this acknowledgment if I'm not to include here Dr. George Tsibidis the "Saint of LIPSS" a truly amazing scientist and person, one of the most important collaborators I have worked with all these years. From the moment I meet him, we were a (theoretical-experimental) match and I own him more than a lot, not only for his unconditional support but also for his great sense of humour, friendship and the numerous unexplained "bugs" he can mysteriously induce in a simple word document.

It is also important to thank Dr. Maria Farsari, Prof. Maria Kafesaki, Prof Ioannis Remediakis and Prof. George Kopidakis for agreeing to evaluate this work without a second thought and for the fact that to most of them I own my scientific background from early years of my postgraduate studies in the Department of Materials Science and Technology.
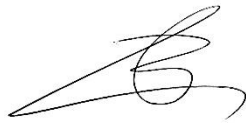
Furthermore, I would like to thank all the members of the Ulmnp lab which were like a huge family will excellently working conditions. Special thanks to the 3A's which are namely Andreas Lemonis, Antonis Papadopoulos and Alexandros Mimidis, i consider them to be my scientific alter egos and the best guys someone can work with. I also owe much to Aleka Manousaki for all the countless hours we spent in the FE-SEM clean room as well as my office mates Dr. Sotiris Psilodimitrakopoulos and Mr. Giannis Lamprakis who could both put up with my noisy character in the office. Moreover, I would like to thank Dr. Ioannis Konidakis, Dr. Anna Tasolamprou and Dr. George Kenanakis for the amazing collaboration we had in parts of this thesis.

Finally, I would like to thank my family, my wife and friends for all the support during these years. As well as the financial support from the European Horizon 2020 - FET OPEN

Σας ευχαριστώ όλους που κάνετε αυτό το ταξίδι αξέχαστο και γεμάτο ευτυχισμένες στιγμές.

Βαγγέλης Σκουλάς

Vitae

The author was born and raised in Heraklion of Crete. He received his postgraduate diploma from the Department of Optics and Vision and his Bachelor degree in Materials Science and Technology Department from the University of Crete. Greece. He started his PhD "Surface structuring of bulk and thin film materials with ultrashort laser pulses" at the Department of Materials Science and Technology of the University of Crete in November of 2017 under the guidance of Dr. Emmanuel Stratakis and Prof. Dimitris Papazoglou. He is a member of the ultrafast laser micro- and nano- processing group at the Institute of electronic structure and laser (IESL) of the Foundation for research and technology – Hellas (FORTH). He specializes in the surface functionalization with ultrashort pulsed laser pulses, light-matter interactions and beam shaping.

Publications related to my thesis

1) C.-Y. Shih, I. Gnilitskyi, M. V. Shugaev, E. Skoulas, E. Stratakis, L. V. Zhigilei, Nanoscale 12 (2020) 7674–7687.

2) Papadopoulos, A., Skoulas E., Mimidis A., Perrakis G., Kenanakis G., Tsibidis G. D., Stratakis E., "Biomimetic Omnidirectional Antireflective Glass via Direct Ultrafast Laser Nanostructuring". Advanced Materials. **1901123**, 1–8 (2019).

3) Petrović S., Peruško D., Skoulas E., Kovač J., Mitrić M., Potočnik J., Rakočević Z.,Stratakis E., "Laser-Assisted Surface Texturing of Ti/Zr Multilayers for Mesenchymal Stem Cell Response". Coatings **9**, 854 (2019).

4) Konidakis, I., Skoulas E., Papadopoulos A., Serpetzoglou E., Margariti E., Stratakis E., "Erasable and rewritable laser-induced gratings on silver phosphate glass". *Applied Physics A* **124**, 839 (2018).

5) Florian C., Skoulas E., Puerto D., Mimidis A., Stratakis E., Solis J., Siegel *J.,* "Controlling the wettability of steel surfaces processed with femtosecond laser pulses". *ACS Applied Materials Interfaces* **10**, 36564–36571 (2018).

6) Tsibidis, G. D., Mimidis A., Skoulas E., Kirner S. V., Krüger j., Bonse J., Stratakis E., "Modelling periodic structure formation on 100Cr6 steel after irradiation with femtosecond-pulsed laser beams". *Applied Physics A* **124**, 27 (2018).

7) Barmina, E. V., Skoulas, E., Stratakis, E. & Shafeev, G. A. "Laser Nano-Structuring of Pre-Structured Substrates". *J. Laser Micro Nanoengineering.* **13**, 6–9 (2018).

8) Papadopoulos, A., Skoulas, E., Tsibidis, G. D. & Stratakis, E. "Formation of periodic surface structures on dielectrics after irradiation with laser beams of spatially variant polarisation: a comparative study". *Applied Physics A Mater. Sci. Process.* **124**, 146 (2018).

9) Baron, C. F. *et al.* "Biomimetic surface structures in steel fabricated with femtosecond laser pulses: Influence of laser rescanning on morphology and wettability". *Beilstein J. Nanotechnology.* **9**, 2802–2812 (2018).

10) Gaković, B., Tsibidis GD., Skoulas E, Petrović S., Vasić B., Stratakis E., "Partial ablation of Ti/Al nano-layer thin film by single femtosecond laser pulse". *Journal of Applied Physics.* **122**, 223106 (2017).

11) Kirner, S. V. *et al.* "Mimicking bug-like surface structures and their fluid transport produced by ultrashort laser pulse irradiation of steel". *Applied Physics A Mater. Sci. Process.* **123**, 0 (2017).

12) Hermens, U. *et al.* "Mimicking lizard-like surface structures upon ultrashort laser pulse irradiation of inorganic materials". *Applied Surface Science* **418**, 499–507 (2017).

13) Skoulas, E., Manousaki, A., Fotakis, C. & Stratakis, E. "Biomimetic surface structuring using cylindrical vector femtosecond laser beams". *Scientific Reports* **7**, 45114 (2017).

14) Tsibidis, G. D., Skoulas, E., Papadopoulos, A. & Stratakis, E. "Convection roll-driven generation of supra-wavelength periodic surface structures on dielectrics upon irradiation with femtosecond pulsed lasers". *Physical Review B* **94**, 81305 (2016).

15) Tsibidis, G. D., Skoulas, E. & Stratakis, E. "Ripple formation on nickel irradiated with radially polarized femtosecond beams". *Optics Letters.* **40**, 5172 (2015).

16) Allahyari, E. *et al.* On the formation and features of the supra-wavelength grooves generated during femtosecond laser surface structuring of silicon. *Appl. Surf. Sci.* **528**, 146607 (2020).

17) Livakas, N., Skoulas, E. & Stratakis, E. Omnidirectional iridescence via cylindrically- polarized femtosecond laser processing. *Opto-Electronic Adv.* **3**, 190035–190035 (2020).

18) Skoulas, E., Mimidis, A., Demeridou, I., Tsibidis, G. D. & Stratakis, E. " Polarization dependent spike formation on silicon via ultrafast laser structuring ". *"submitted"*

19) Skoulas, E., Tasolabrou, A., Kenanakis, G. & Stratakis, E. "Laser induced wire grid polarizing plates". *"Manuscript ready for submission"*

20) Stratakis, E. *et al.* Laser engineering of biomimetic surfaces. *Mater. Sci. Eng. R Reports* **141**, 100562 (2020).

Conference Presentations

1. V. Skoulas, A. Papadopoulos, G. D. Tsibidis, E. Stratakis. Ultrafast laser processing of transparent materials for the fabrication of biomimetic surfaces. **Oral Presentation** on 6th International Symposium on Transparent Conductive Materials Chania 2016.

2. E. Skoulas, E. Stratakis. Ultrafast laser fabrication of biomimetic micro and nano structured surfaces. **Oral Presentation** at DPG spring meeting 2017, Mainz, Germany

3. E. Skoulas, E. Stratakis. Biomimetic surface structuring using cylindrical vector femtosecond laser beams. **Oral & Poster presentation**, EMRS Spring meeting 2017 symposium K. Strasbourg, France.

4. E. Skoulas, A. Mimidis, A. Papadopoulos, C. Lanara, N. Livakas , G.D Tsibidis, and E. Stratakis, Laser-induced multi-functional biomimetic surfaces. **Oral presentation**, CLEO®/Europe – EQEC, 2019, Munich, Germany.

5. E. Skoulas, Tsibidis G.D., E. Stratakis. Versatile surface processing using CV femtosecond laser pulses. **Oral presentation** ,ICPEPA conference, September, 2018, Vilnius, Lithuenia.

6. E. Skoulas, E. Stratakis, Ultrafast laser surface structuring using cylindrical vector polarization states, **Oral presentation**, EUROMAT 2017, Thessaloniki, Greece.

Patents related to my thesis

1. "USING LASERS TO REDUCE REFLECTION OF TRANSPARENT SOLIDS, COATINGS AND DEVICES EMPLOYING TRANSPARENT SOLIDS" E. Stratakis, E. Skoulas, A Papadopoulos. PCT Publication number: PCT/GR2018/000014
2. "LASER FABRICATED SUPEROLEOPHILIC METALLIC COMPONENT WITH OIL RETENTION PROPERTIES FOR FRICTION REDUCTION" E. Stratakis, E. Skoulas, A. Mimidis, J. Siegel, C. F. Barron. PCT/GR2019/000056
3. "ULTRAFAST LASER FABRICATION OF A THIN FILM ON A SUBSTRATE POLARIZING PLATE" E. Stratakis, E. Skoulas. Filled to OBI.